INFLUENCE OF COMPOSITION ON THE STRUCTURE, ELECTRIC AND MAGNETIC PROPERTIES OF Pd-Mn-P AND Pd-Co-P AMORPHOUS ALLOYS

Thesis by

Neville Ingersoll Marzwell

In Partial Fulfillment of the Requirements

for the Degree of

Doctor of Philosophy

California Institute of Technology

Pasadena, California

1973

(Submitted May 7, 1973)

To all those who by thoughts, words, and actions made the present stage in the life of the author possible.

ACKNOWLEDGMENTS

The work described in this thesis is part of a continuing program directed by Professor Pol E. Duwez concerning the properties of amorphous alloys. This work was supported in part by the United States Atomic Energy Commission, the Ford Foundation and the Josephine de Karman fellowship. Acknowledgment is also made to the California Institute of Technology for a Graduate Research Assistantship.

The author would like to express his deepest gratitude to Professor P. Duwez for the help, encouragement and guidance given during his graduate career. He wishes to express his appreciation for the counsel of Dr. J. Dixmier, Dr. A. S. Gargill III, Dr. M. Cyrot and Dr. W. Goddard. It is a pleasure to acknowledge the help of my co-workers for stimulating scientific viewpoints and F. Koenig, P. Schluter, S. Kotake, H. Arnal, J. Wysocki for assisting in the experiments. The care of Miss Loraine Broderick in proofreading and the diligence of Mrs. Ruth Stratton in typing the manuscript is greatly appreciated.

ABSTRACT

The influence of composition on the structure and on the electric and magnetic properties of amorphous Pd-Mn-P and Pd-Co-P prepared by rapid quenching techniques were investigated in terms of (1) the 3d band filling of the first transition metal group, (2) the phosphorus concentration effect which acts as an electron donor and (3) the transition metal concentration.

The structure is essentially characterized by a set of polyhedra subunits essentially inverse to the packing of hard spheres in real space. Examination of computer generated distribution functions using Monte Carlo random statistical distribution of these polyhedra entities demonstrated the reproducibility of the experimentally calculated atomic distribution function. As a result, several possible "structural parameters" are proposed such as: the number of nearest neighbors, the metal-to-metal distance, the degree of short-range order and the affinity between metal-metal and metal-metalloid. It is shown that the degree of disorder increases from Ni to Mn. Similar behavior is observed with increase in the phosphorus concentration.

The magnetic properties of Pd-Co-P alloys show that they are ferromagnetic with a Curie temperature between 272 and 399^{o}K as the cobalt concentration increases from 15 to 50 at.%. Below 20 at.% Co the short-range exchange interactions which produce the ferromagnetism are unable to establish a long-range magnetic order and a peak in the magnetization shows up at the lowest temperature range. The electric resistivity measurements were performed from liquid helium temperatures

up to the vicinity of the melting point ($900^{o}K$). The thermomagnetic analysis was carried out under an applied field of 6.0 kOe. The electrical resistivity of Pd-Co-P shows the coexistence of a Kondo-like minimum with ferromagnetism. The minimum becomes less important as the transition metal concentration increases and the coefficients of $\ell n\ T$ and T^2 become smaller and strongly temperature dependent. The negative magnetoresistivity is a strong indication of the existence of localized moment.

The temperature coefficient of resistivity which is positive for Pd-Fe-P, Pd-Ni-P, and Pd-Co-P becomes negative for Pd-Mn-P. It is possible to account for the negative temperature dependence by the localized spin fluctuation model and the high density of states at the Fermi energy which becomes maximum between Mn and Cr. The magnetization curves for Pd-Mn-P are typical of those resulting from the interplay of different exchange forces. The established relationship between susceptibility and resistivity confirms the localized spin fluctuation model. The magnetoresistivity of Pd-Mn-P could be interpreted in terms of a short-range magnetic ordering that could arise from the Ruderman-Kittel type interactions.

TABLE OF CONTENTS

I. INTRODUCTION

The technique for quenching liquid alloys at very high rates of cooling in the range of 10^3 to 10^8 ^oC/sec has led to the synthesis of three types of new alloys, namely supersaturated solid solution, crystalline phases, which do not exist under equilibrium conditions, and amorphous alloys. The latter type of alloy phases which is studied in this essay, represents the ultimate in quenching rate since the atomic arrangement present in the liquid state is retained after solidification.

Although the number of amorphous alloys obtained so far by liquid quenching is not large enough to formulate definite rules governing the occurrence of an amorphous phase, four observations were formulated by Professor Pol Duwez[1] as follows: 1) Alloys with composition around the eutectic point were found to have a greater chance to solidify to an amorphous state provided the eutectic is steep, meaning that the eutectic temperature is low with respect to the melting point of the predominant metallic constituent. 2) The "confusion principle" which states that an alloy containing a large number of different atoms has a greater capacity to prevent the normal process of crystallization. 3) The "covalent bonding condition" which suggests that as a condition for glass formation from the liquid state a certain amount of covalent bonding is required. 4) A rather high viscosity in the liquid state. These observations lead to the support of the theory of Cohen and Turnbull[2] on glass formation. According to Cohen et al, impurity addition seems to raise the free energy of the

crystalline states in a system more than the energy of the amorphous state and thus increases the tendency for glass formation.

Many attempts were made to describe the short-range order[3-5] existing in amorphous materials. A crystalline fcc and hcp[6] were first proposed as a possible description. Then a quasi-crystalline model[7] based on the intermetallic compound Pd_4P gave a better agreement for Pd-Ni-P and Pd-Fe-P. The weakness of this approach is that it does not take into consideration the fact that atoms have been moved independently from each other and that a main criterion for the structure is to account not only for the size and concentration of the constituents but also for the affinity between metal and metalloids. We are then left with the hard sphere model[8] which favors the attractive potential between the spheres as a guiding criterion, while the repulsive potential is favored by the Bernal[9] model packing structure.

The anomalous electrical properties of amorphous alloys containing a transition metal were qualitatively explained by Friedel[10] and Anderson[11] in terms of localized virtual bound state model (v.b.s.). In this concept, conduction electrons are polarized through s-d exchange interaction[12]. Gerritsen[13] explained the resistivity minimum by postulating that the transition metal introduces spatially localized states with energies near the Fermi energy. Kasuya[14], Schmitt[15] and Yosida[16] developed various theories based on a perturbing potential consisting of spin-dependent and spin-independent interactions between the 4s conduction electrons and the 3d electrons localized on the transition metal atom. Kondo[17] explains the resistivity minimum observed in these alloys from a simplified s-d exchange model

consisting of localized spins and conduction electrons. He obtained the spin contribution to the resistivity term ($\propto$ ℓn T) by calculating the transition probability to the second Born approximation. The resistivity minimum is therefore the combined effect of this logarithmic term with the electron-phonon contribution to the resistivity. Some revised theories along this line of thought have been proposed by Nagaoka[18], Suhl and Wong[19] and by Hamann[20]. Recently Rivier, Zuckermann and Šunjić[21] overcame the sharp and unphysical boundary between magnetic and nonmagnetic impurities in the Friedel-Anderson theory by replacing it with a smooth transition between slow and fast localized spin fluctuation regimes (LSF). In this model the time scale of the LSF is clearly important, as it is implied that the resistivity is determined by only the time-average cross section and the magnetic susceptibility by the time-average polarization. This is valid only if the LSF are fast compared with other relevant times. On the other hand, if the LSF are slow enough, the conditions become very close to the Friedel-Anderson condition where the magnetic moments have sufficient time to equilibrate or to flip the spin of a conduction electron. The magnetoresistivity in the amorphous alloys is generally negative and follows similar lines to Yosida[16] theory. The magnetic properties are quite complicated and can be described best by the Blandin[22] regime involving collective and random distribution of magnetic spins.

The specific objectives of this thesis are: 1) To prepare amorphous alloys of composition Pd-Mn-P and Pd-Co-P, and study the structure, electric and magnetic properties in terms of a varied concentration of transition metal as well as a varied concentration of

glass former. 2) To study the mechanism of electrical conduction in terms of "d band" filling by going across the first d transition metals and by electron transfer from the phosphorus. 3) To study the magnetoresistivity as well as the magnetic behavior of amorphous alloys and thus shed some light on the behavior of a metallic transition atom carrying moment, on short range magnetic orders, on the magnitude of exchange interactions and superexchange forces. 4) To build a structural model for the amorphous metallic alloys and attempt to study the effect of exchange anisotropy and local atomic environment on the atomic moment of Co and Mn. 5) To establish the mechanism and temperature of ordering.

An added interest is in terms of the future practical applications of these materials. Some amorphous alloys have proved to have very unusual electrical and magnetic properties and the size limitation has not any serious consequences, as they could be used as components of integrated miniature circuits, magnetic films, magnetic memories, as well as a choice material for high resistance with low coefficient of expansion. The amorphous alloys should be considered as a choice material for thermometers, magnetic switches, and gages in high radiation regions. Also the already observed high strength of supersaturated solid solutions opens new fields for engineering applications.

II. ALLOY AND SPECIMEN PREPARATION

The amorphous Pd-Mn-P and Pd-Co-P alloys were obtained by rapid quenching from the liquid state using the "piston and anvil" method[23]. The alloys were prepared by "reactive sintering" techniques based on powder metallurgy as these alloys contain large amounts of phosphorus and could not be obtained by direct melting of the constituents. The Mn was electrolitically pure, the Pd was 99.99% pure, lot R-728 No. 162. Englehard, contained a maximum of 26 p.p.m. Fe, and the cobalt was spectrographically standardized to 99.99% pure, laboratory No. W.899 Johnson, Matthey and Co., London. The phosphorus was reagent grade red amorphous powder, lot No. 35, 427 Baker Chemical Co., Phillipsburg, New Jersey. The elements were carefully weighed and mixed. A total of 2 grams of mixed powder was consolidated into a briquet in a 1/4 inch diameter steel die under a pressure of 50.000 psi. The sintering was carried out in an evacuated pyrex capsule at a slowly increasing temperature up to 500°C at an average rate of heating of 20°C/hour, so that the reaction between phosphorus and the metal could proceed in the solid state until all the phosphorus was combined into a stable phosphide. The pyrex tubes were then opened to release whatever gas pressure might be present. The sample was then placed in evacuated quartz tubes and heated to a temperature near the melting point about 560°C to 600°C where it was kept for about 3 days and then taken out of the furnace.

The sintered briqueted alloy was then melted in quartz crucibles in an induction furnace under an argon atmosphere and the melt was cast

into several 2 mm diameter rods by sucking the liquid alloy into a quartz tube. No noticeable reaction occurred between the melt and the quartz crucible which indicated that the phosphorus was entirely combined into stable phosphide before melting occurred. The rods were then broken into pieces of appropriate size for use in the quenching process. Full details may be found elsewhere.

The amorphous state of the alloys was obtained by quenching from the liquid state. The "piston and anvil" technique was used where a small globule of liquid alloy was contained in a fused silica tube for about 30 seconds before quenching. This time is short enough to prevent reaction between the liquid alloys and the fused silica tube. Every foil used in the present study was carefully checked by x-ray monochromatized molybdenum radiation, and microcrystals, if any, could be detected by weak Bragg reflections superimposed to the broad maximum.

The amorphous foil quenched from the liquid state for Pd-Mn-P and Pd-Co-P were about 2.5 cm in diameter and 40 to 60μ thick. From these foils a rectangular specimen of about 40×4 mm was cut for resistivity measurements. Current potential leads, made of 0.005" Pt wires were spot welded to the specimen. For the magnetic susceptibility measurements, few 3 mm diameter wafers were obtained by a punch of the amorphous foil and a total amount of about 2 to 10 mg in weight was used.

III. STRUCTURE INVESTIGATION BY X-RAY DIFFRACTION OF LOCAL ORDER IN AMORPHOUS METALLIC ALLOYS

Since the theoretical foundation of radial distribution analysis of liquid diffraction patterns were laid in 1927 by Zernicke and Prins[24], progress in apparatus, experimental techniques and computerized methods of calculation have ensured a greater reliability and hence greater confidence in the method as a means of evaluating a structure of amorphous alloys.

A brief discussion of the theory and a detailed analysis of the procedure to identify, isolate and correct for the errors that lead to parasitic undulations in the probability distribution functions is described.

A. Notion of Amorphous Structure

The word "amorphous" means "no form" or lacking structure. Therefore all solids composed of crystals of size lower than the diffraction power or separation of the optical instrument have to be assumed amorphous. Bernal defines the liquid state as "an assembly of atoms irregular, coherent and homogeneous".

So if we imagine a model made of spheres, we will view the first nearest neighbor of an atom taken as origin to be slightly displaced with respect to its ideal position in a crystalline phase, and the disorder grows increasingly as we go further and further away from the atom taken as origin. We can solve this vocabulary problem if we adopt a molecular model with an identity unit practically unchanged and undeformed. This solid is called amorphous if these molecular

units are not periodically placed in space.

The degree of structure in solids as well as in liquids can be deduced from an analysis of their diffraction patterns.

In general, one distinguishes between the small-angle scattering (the scattering close to the primary beam), and the large angle scattering which includes all angles of scattering other than the small angle. The large angle scattering is governed by the atomic distribution function $W(r)$ which represents the number of j-type atoms per unit volume at the distance r from an i-type atom averaged over all i-atoms in the sample, and the size of the diffracting domains; whereas the small-angle scattering is a consequence of the size of the heterogeneities in the atomic densities in the sample--that is, by the size of the diffracting domains if they are sufficiently separated by regions of low or zero atomic densities.

If now we try to distinguish between liquids, microcrystalline and amorphous structure, Figs. 1 and 2, we find that there are four features to look for: (a) At very low angles, the small size of the crystals makes a high intensity peak appear, which is not found in the liquid state. This part of the curve has no relation with the internal structure of the grain, but with its size and its exterior shape. (b) The first peak height is weaker for the scattering of the powder than it is for the liquid. (c) The width of the first peak measured at half height is greater for the powder sample. (d) The intensity of the different peaks is damped much more rapidly in the liquid curve.

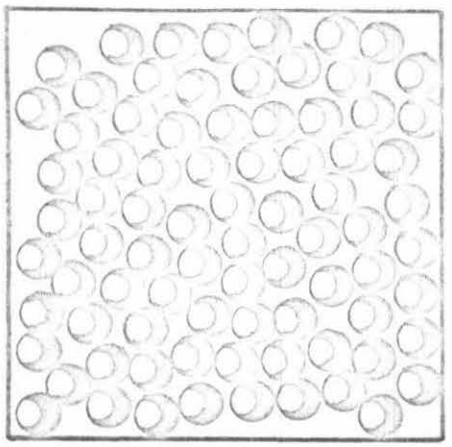

1.A - Liquid

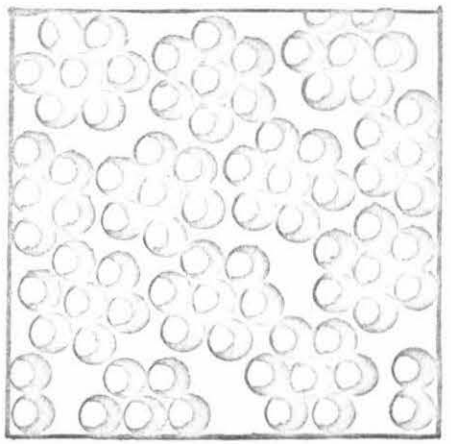

1.B - Microcrystaline powder

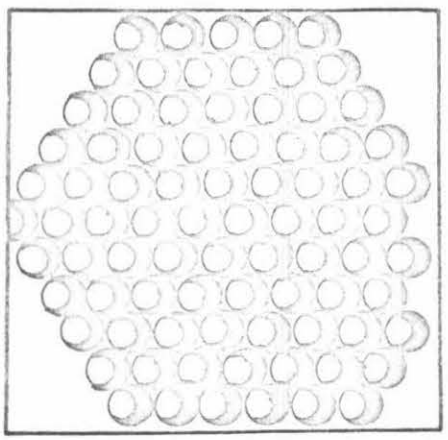

1.C - Single crystal

Fig. 1. Two-dimensional representation of an assembly of atoms grouped into 3 types of structure (Ref. 25).

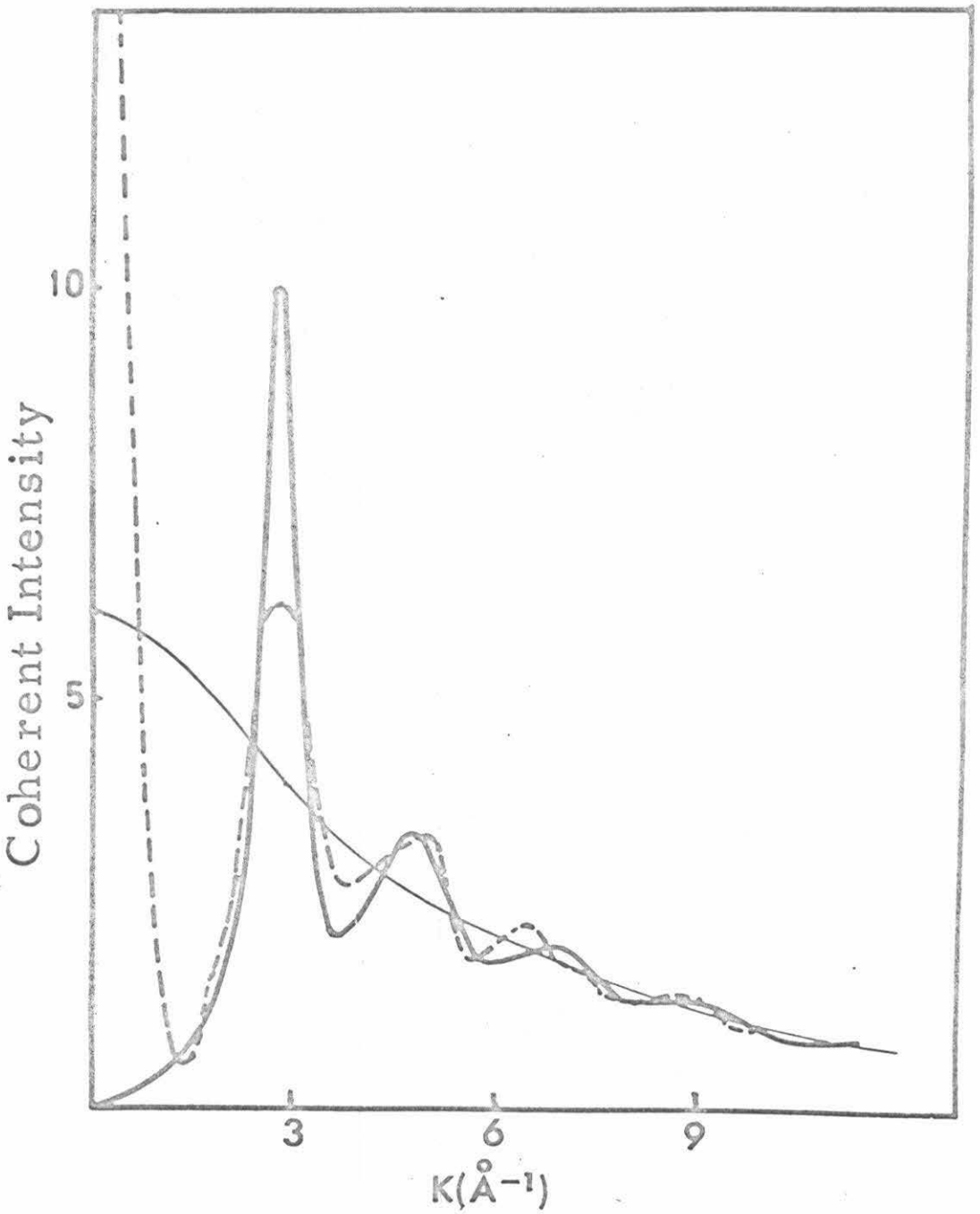

Fig. 2. Coherent intensity of a liquid metal (solid line) and a system of microcrystals (dashed line) (Ref. 25).

The techniques that are used have been used by Debye and then by Zernicke and Prins[24] and many others[26]. The mathematical background is therefore well known and accepted by now. The diffraction spectrum of amorphous alloys leads, after appropriate corrections, to an interference function. This function, through a Fourier transformation, yields an atomic or electronic radial distribution function. This process is rather straightforward in a monoatomic system, but requires some approximations in multicomponent alloy systems.

B. Theoretical Review

1. Theoretical Aspect of the Structure Determination of an Amorphous Alloy

The total scattered intensity $I_{scattered}$ (in arbitrary units) at a given angle, consists of the coherent scattered intensity $I_{coherent}$ plus the incoherent intensity $I_{incoherent}$ due to Compton scattering and a background intensity $I_{background}$. All of these are also affected by a polarization factor $P(2\theta)$ and an absorption factor $A(2\theta)$. The total scattering intensity is given by the following equation:

$$I_{scattered}(2\theta) = [I_c(2\theta) + I_{inc}(2\theta) + I_b(2\theta)]\ P(2\theta)\ A(2\theta) \qquad (1)$$

The most important term is the coherent scattered intensity I_c which leads to the atomic distribution function.

By definition, the diffracting power $I_t(K)$ of a diffracting object is the ratio of the measured diffracted rays of the object to the isolated electron[5]. The diffraction power is reported to unitary

atom, by taking the diffracted power of the object and dividing it by the number of atoms. Now if a sample is made of very many grains placed in an x-ray beam, how can we calculate its scattering power? Debye suggested that the total diffracted power of an amalgamation of identical objects each containing N atoms, distributed at random, is equivalent to the mean value with respect to time of the scattering factor of a simple object if we take, with respect to the beam, all the possible different orientations with an equal probability in each orientation. The scattered intensity in electron units is therefore:

$$I_{\text{scattered}}(K) = \sum_i \sum_j f_i f_j \frac{(\sin Kr_{ij})}{Kr_{ij}} \qquad (2)$$

where $K = \frac{4 \sin \theta}{\lambda}$ and r_{ij} is the interatomic distance between atom i and atom j, the summation being extended to the entire solid. Equation (2) can be rewritten as

$$I_{\text{scattered}}(K) = N[\sum_i x_i f_i^2 + \sum_i x_i \sum_{J \neq 1} f_i f_j (\frac{\sin Kr_{ij}}{Kr_{ij}})] \qquad (3)$$

where N is the total number of atoms in the sample and x_i is the atomic concentration of element i. In the present case i goes from 1 to 3 (Pd, Mn, P) and j means all the atoms in the system except the chosen atom i. The diffracted intensity, when corrected for polarization and absorption, becomes the sum of only the coherent scattered intensity I_c, the Compton modified scattering I_{inc} and the background I_b :

$$\frac{I_{total}}{(P \times A)} = I_c + I_{inc} + I_b \qquad (4)$$

As far as absorption is concerned, the thickness of the specimen is calculated for both CuKα radiation (Table 1, 2 and 3) and chosen experimentally to be considered as infinitely thick so that the absorption factor A is independent of angle. Also the use of a diffracted beam monochromator removes most of the fluorescent radiation as well as Compton modified scattering at high angles[27], leaving only a small part of the incoherent and background intensities which act together and will be called from now on "effective background I_B".

For the polarization factor P for LiF monochromator at a Bragg angle θ corresponding to a 200 reflection

$$P = \frac{(1 + \cos^2\beta \cos^2 2\theta)}{(1 + \cos^2 2\beta)} \qquad (5)$$

Equation (1) could be written

$$(I_{scattered}/P - I_B)\alpha = I_c \text{ (electron unit)} \qquad (6)$$

where all quantities are functions of 2θ or K, which is the modulus of the scattering vector, except α .

The normalization constant α converts the coherent intensity from arbitrary units into that of electron units per atom of the alloy, and is determined by the high angle method[26] assuming the following "atomic gas" relation to be valid

$$I_c \simeq \sum_m x_m f_m \qquad \text{for } K > 17.1 \text{Å}^{-1}$$

For the amorphous alloy (3) can be written as follows[28,29]:

$$I_{coh}(e.u.) = \sum_m x_m f_m^2 + f_e^2 \int_0^\infty 4\pi r^2 (\sum_m x_m N_m)[g(r) - g_o] \frac{\sin Kr}{Kr} dr \quad (7)$$

The coefficient N_m is a constant coefficient assumed to be equal to the effective number of electrons for atoms of type m and can be approximated to:

$$N_m = \frac{f_m(K)}{f_e(K)}$$

where

$$f_e = \frac{\sum_m \frac{x_m}{f_m}}{(\sum_m x_m z_m)} \quad (8)$$

$f_e(K)$ is the effective scattering factor per electron, z_m is the atomic number, f_m the atomic scattering factor corrected for anomalous dispersion[30,31] and $f_e(K)$ is the effective scattering factor per electron.

If we denote a_m, a_n and a_p to be the number of atoms of Pd, Mn and P in an interval dr at a radial distance r from the center of any atom m, and define

$$g(r)\, dr = \frac{1}{4\pi r^2} \sum_m a_m N_m \quad (9)$$

and

$$\rho(r)\, dr = \frac{1}{4\pi r^2} \sum_m a_m \quad (10)$$

it can be seen by comparison of (9) and (10) that the ratio of $g(r)$ to $\rho(r)$ may be equated to the total number of effective electrons per atom

$$\frac{g(r)}{\rho(r)} = \sum_m x_m N_m \tag{11}$$

We may as well define $g_o(r)$ to be the average electronic density and $\rho_o(r)$ to be average atomic density in the alloy and obey a similar relation to that of (14).

Using relations (7) and (11), we may write (8) as

$$K[a(K) - 1] = \int_0^\infty 4\pi r[\rho(r) - \rho_o] \sin Kr \, dr \tag{12}$$

where

$$a(K) = 1 + \frac{(I_c - \sum_m x_m f_m^2)}{\sum_m (x_m f_m)^2} \tag{13}$$

Equation (13) is called by some the interference function, but in this study the interference function $I(K)$ is defined as

$$I(K) = a(K) - 1 \tag{14}$$

2. The Correspondence by the Fourier Transformation between the Interference Function and the Atomic Distribution Function

The number of atoms included in a shell of thickness dr is $4\pi r^2 \rho(r)\, d(r)$. The interference function $I(K)$ using relations (12), (13) and (14) and performing the Fourier inversion becomes

$$W(r) = \frac{2}{\pi} \int_0^\infty K[I(K)] \sin Kr \, dK \tag{15}$$

where $W(r)$ is the atomic distribution function with

$$W(r) = 4\pi r[\rho(r) - \rho_o] \tag{16}$$

Going from equation (12) to (15) would have been impossible by direct Fourier inversion as our system is not a monatomic alloy, so a solution suggested by Warren[28], and since then commonly used[32,33], was assumed. It consists of using a reduced scattered factor as shown in equations (10) and (11). So $\rho(r)$ as used is really a weighted average atomic density function and it could be written explicitly in terms of a pair distribution function $\rho_{mn}(r)$ [34]

$$\rho(r) = \sum_m \sum_n W_{mn}\, \rho_{mn}(r) \tag{17}$$

where the weighting factor W_{mn} is

$$W_{mn} = \frac{x_m N_m N_n}{(x_m N_m)^2} \tag{18}$$

To be able to perform the Fourier transform of (14) we had to assume W_{mn} independent of K. This is true only in a "perfect powder" containing a great number of grains distributed randomly. This is how an amorphous alloy is visualized, and the error introduced into the atomic distribution function $W(r)$ due to the assumption of a constant W_{mn} becomes vanishingly small as complete randomness is approached.

With the above assumptions in mind, the atomic distribution function $W(r)$ is a convolution-broadened weighted average sum of six pair of atomic distribution functions[35] corresponding to the combinations Pd-Pd, Mn-Mn, P-P, Pd-Mn, Pd-P, and Mn-P.

C. Experimental Procedure

The Pd-Mn-P alloys were prepared by the piston and anvil quenching method and varied in thickness between 40 and 55μ. To avoid the correction for any angular dependence on the absorption, the mass absorption coefficients for the compositions investigated by CuK_α and MoK_α radiation were calculated and tabulated in Table 1. From the values of μ/ρ and the density of the alloys ($10 g/cm^2$) only three to four foils were judged necessary for MoK_α radiation and one foil was judged more than necessary for CuK_α radiation to eliminate the necessity of including an absorption factor in the present analysis.

The specimen, consisting of four foils glued together with thinned Duco cement on a bakelite substrate, was mounted on the sample holder of a G.E. diffractometer with vertical axis after a series of steps to insure against the presence of any possible microcrystalline peaks. First each foil was carefully checked by taking its x-ray diffraction pattern in the region of the first broad band with MoK_α, then carefully checked by scanning the first diffraction maximum with CuK_α radiation between 30^o and 50^o in 2θ angle value. The diffractometer moved at the rate of 0.04^o/min and an intensity reading was automatically plotted on an H-P chart recorder every 100 seconds, which corresponds to a 2θ interval of 0.066^o. Any crystalline phase could be detected by the presence of a few weak but relatively sharp peaks superimposed upon the smooth broad band characteristic of the amorphous phase. The x-ray diffraction patterns used in this study were recorded using a G.E. diffractometer fitted with a double curvature LiF crystal monochromator located on the diffracted beam to

Table I. Mass absorption coefficients of $Pd_{100-x}Mn_x)P_{23}$ for CuK_α and MoK_α radiation

	Comp. (at %)			Comp. Wgt. %			MoK_α	CuK_α	$\mu(MoK_\alpha)$	$\mu(CuK_\alpha)$
	Pd	Mn	P	Pd	Mn	P	$\mu/\rho(cm^2/g)$	$\mu/\rho(cm^2/g)$	microns	microns
$Pd_{85}Mn_{15})_{77}P_{23}$	65.45	11.55	23	83.79	7.64	8.57	25.61	201.40	36.22	4.60
$Pd_{83}Mn_{17})_{77}P_{23}$	63.91	13.09	23	82.61	8.74	8.65	25.67	202.14	36.34	4.61
$Pd_{80}Mn_{20})_{77}P_{23}$	61.60	15.40	23	80.79	10.43	8.78	25.76	203.26	36.52	4.62
$Pd_{75}Mn_{25})_{77}P_{23}$	57.75	19.25	23	77.64	13.37	9.00	25.92	205.25	36.83	4.65
$Pd_{70}Mn_{30})_{77}P_{23}$	53.90	23.10	23	74.33	16.45	9.23	26.09	207.32	37.18	4.67
$Pd_{65}Mn_{35})_{77}P_{23}$	50.05	26.95	23	70.83	19.70	9.47	26.27	209.48	37.55	4.70
$Pd_{63}Mn_{37})_{77}P_{23}$	48.51	28.49	23	69.39	21.04	9.57	26.33	210.37	37.74	4.72
$Pd_{62}Mn_{38})_{77}P_{23}$	47.74	29.26	23	68.66	21.72	9.62	26.38	210.83	37.80	4.73

Table II. Mass absorption coefficients of $(Pd_{70}Mn_{30})_{100-y}P_y$ for CuK_α and MoK_α radiation

	Comp.(at %)			Comp. Wgt. %			MoK_α	CuK_α	$\mu(MoK_\alpha)$	$\mu(CuK_\alpha)$
	Pd	Mn	P	Pd	Mn	P	$\mu/\rho(cm^2/g)$	$\mu/\rho(cm^2/g)$	microns	microns
$(Pd_{70}Mn_{30})_{83}P_{17}$	58.1	24.9	17	76.54	16.93	6.51	26.63	211.27	35.55	4.48
$(Pd_{70}Mn_{30})_{82}P_{18}$	57.4	24.6	18	76.19	16.86	6.95	26.54	210.67	35.81	4.51
$(Pd_{70}Mn_{30})_{81}P_{19}$	56.7	24.3	19	75.82	16.78	7.40	26.45	210.00	36.07	4.54
$(Pd_{70}Mn_{30})_{80}P_{20}$	56.0	24.0	20	75.46	16.70	7.84	26.37	209.35	36.32	4.57
$(Pd_{70}Mn_{30})_{79}P_{21}$	55.3	23.7	21	75.09	16.62	8.30	26.28	208.70	36.60	4.61
$(Pd_{70}Mn_{30})_{78}P_{22}$	54.6	23.4	22	74.71	16.53	8.76	26.18	207.99	36.89	4.64
$(Pd_{70}Mn_{30})_{77}P_{23}$	53.9	23.1	23	74.33	16.45	9.23	26.09	207.32	37.18	4.68
$(Pd_{70}Mn_{30})_{76}P_{24}$	53.2	22.8	24	73.93	16.37	9.70	26.00	206.61	37.47	4.71
$(Pd_{70}Mn_{30})_{75}P_{25}$	52.5	22.5	25	73.53	16.27	10.19	25.90	205.85	37.79	4.75
$(Pd_{70}Mn_{30})_{74}P_{26}$	51.8	22.2	26	73.13	16.18	10.68	25.80	205.13	38.10	4.79
$(Pd_{62}Mn_{38})_{75}P_{25}$	49.5	28.5	25	67.88	21.48	10.62	26.17	209.07	38.46	4.81

Table III. Mass absorption coefficients of $(Pd_{100-x}Co_x)P_{20}$ for CuK_α and MoK_α radiation

	Comp.(at %)			Comp. Wgt. %			MoK_α	CuK_α	$\mu(MoK_\alpha)$	$\mu(CuK_\alpha)$
	Pd	Co	P	Pd	Co	P	$\mu/\rho(cm^2/g)$	$\mu/\rho(cm^2/g)$	microns	microns
$(Pd_{85}Co_{15})_{80}P_{20}$	68.0	12.0	20	84.50	8.25	7.24	26.57	209.40	34.20	4.34
$(Pd_{80}Co_{20})_{80}P_{20}$	64.0	16.0	20	81.34	11.26	7.40	26.99	213.63	34.00	4.29
$(Pd_{75}Co_{25})_{80}P_{20}$	60.0	20.0	20	78.02	14.41	7.57	27.43	218.04	33.81	4.25
$(Pd_{70}Co_{30})_{80}P_{20}$	56.0	24.0	20	74.56	17.69	7.75	27.88	222.61	33.64	4.21
$(Pd_{65}Co_{35})_{80}P_{20}$	52.0	28.0	20	70.92	21.15	7.93	28.37	227.46	33.45	4.17
$(Pd_{60}Co_{40})_{80}P_{20}$	48.0	32.0	20	67.09	24.78	8.13	28.87	232.53	33.29	4.13
$(Pd_{55}Co_{45})_{80}P_{20}$	44.0	36.0	20	63.07	28.59	8.34	29.42	237.85	33.11	4.09
$(Pd_{50}Co_{50})_{80}P_{20}$	40.0	40.0	20	58.85	32.59	8.56	29.95	243.44	33.00	4.06

eliminate K_β, the white spectrum, the fluorescent scattering[34], and most of the incoherent scattering, although not all[36,37]. The units were run under 45 KV and 38 mA, to provide a sufficient intensity. The incident beam was collimated by a system of slits which allowed different beam divergences. As it takes ten days to record the entire diffraction pattern of each alloy, the unit was made to run until satisfactory reproduction confirmed the stability of the x-ray tubes, the scintillation counter which was checked using a radioactive source, the associated electrical circuitry, and the pulse height analyzer which acted as detector. The pulse height analyzer was adjusted to eliminate $\lambda/2$ which is let through the monochromator. The contribution of intensity due to $\lambda/2$ was checked to be of the order of 15 counts/sec to 10,000 counts/sec for $K\alpha$ which is indeed negligible; in the absence of pulse height analyzer the $\lambda/2$ contribution was still small, although 10 times the above value. The stability of the equipment was within 1% for periods of time up to 120 hours.

The diffraction pattern was recorded in the range $12^o \leq 2\theta \leq 68^o$ with a scanning rate of 0.02^o per 100 sec and then $63^o < 2\theta < 163^o$ at the rate of 0.04^o per 100 seconds. The beam divergence employed was 1^o. The number of counts was printed every 1000 sec with a Beckman printer. The total time for a complete scan was 139 hours. Before the data were fed to the computer, the intensity vs. 2θ curves were plotted on a large scale graph paper to make sure that the curves were smooth and no failure occurred in the electric recording equipment. The stability of the system was better than 1.2% per

period of 96 hours.

D. Treatment of Data

1. Interference Function

From experimental measurements we obtain the scattered diffraction intensity $I_{scattered}$ which when properly corrected as mentioned previously gives the $I_{coherent}$:

a) The conversion of measured intensity to unitary scattering power, in electron units per atom is called normalization of the intensity. b) The integration from zero to infinity of the function $I(K)$ is limited experimentally to K_{max}. This leads on the Fourier transformed function $W(r)$ to the appearance of a phenomenon known as termination effect. c) The change of the integral to a sum gives the difficult choice of imposing the range of values of the variables. d) The atomic distribution function obtained by this method does not allow reconstitution of the image of the structure in real space, because the instrument of measurement used registers variation of intensity only; that is, the square of the amplitude of the diffracted waves. Also the phase of those waves which are necessary to calculate the interference function in real space is not known. So the atomic distribution function (equation (18)) is zero for all distances smaller than the distance between first nearest neighbors and shows some characteristic oscillations representing the degree of short range order which vanish as the distance of separation increases.

2. Normalization Errors

The scattering power reported to unity is obtained generally by identifying the magnitude of the measured intensity at high angles to the sum of the coherent Compton scattering of the elements. In fact, the interference is negligible at these high angles, due to the disordered structure at high distances. This method of normalization has the inaccuracy that at high angles the scattered intensity becomes weak; the error committed in evaluating the diffracted intensity with respect to background increases with the angle.

The conversion of experimental values to absolute intensity values in electron units introduces errors which could not be eliminated.

a. Methods used to reduce the errors in normalization.

Averbach, Strong and Kaplow[38] suggested a method based on the fact that the atomic distribution function $W(r)$ should not oscillate for values of r smaller than the first nearest neighbors and should be a straight line of slope -1 before the bottom of the first peak. Any deviation from a straight line in this region results from parasitic effects. This is why published distribution functions have an obliterated beginning. Some obliterate the beginning under the pretext or assumption that the beginning is without use or physical significance. Here it will be shown quite the opposite, that by the analysis of those oscillations it will be possible to learn how to correct the normalization.

Assume that after a long and tedious process of correction of $I(K)$ an atomic distribution function $W(r)$ was reached which does not have any oscillation at the straight line of slope -1 of the curve. To this atomic distribution function $W(r)$ corresponds an interference function $I(K)$, and consequently a coefficient α of normalization.

Averback and Kaplow varied k by a few percent around the correct value, and using this modified value of k, calculated the interference function. The result of this effort was to show the addition of a rapidly damping oscillatory wave, which imposes itself on $W(r)$. By subtraction of the mutual function from the modified k function we isolate the phenomenon due to the deviation with normalization which is shown in Fig. 3 by varying 1% on the normalization factor of $(Pd_{75}Mn_{25})_{77}P_{23}$. By varying k by a few percent around the real value of α, we can study the different atomic distribution functions obtained relative to each value of k. Using this approach we noticed the following:

1. Beyond the first maximum, the effect is very weakly sensitive, the amplitude of the first peak varies slightly but the amplitudes of the other peaks are affected unnoticeably. Also parasitic undulations add themselves to the whole curve and are especially noticeable in the first few peaks.
2. Before the first nearest neighbor, the first oscillation is very sensitive to k and disappears for $k = 1.042$. The normalization should therefore be considered as acceptable when the parasitic oscillations disappear close to $r = 0$.

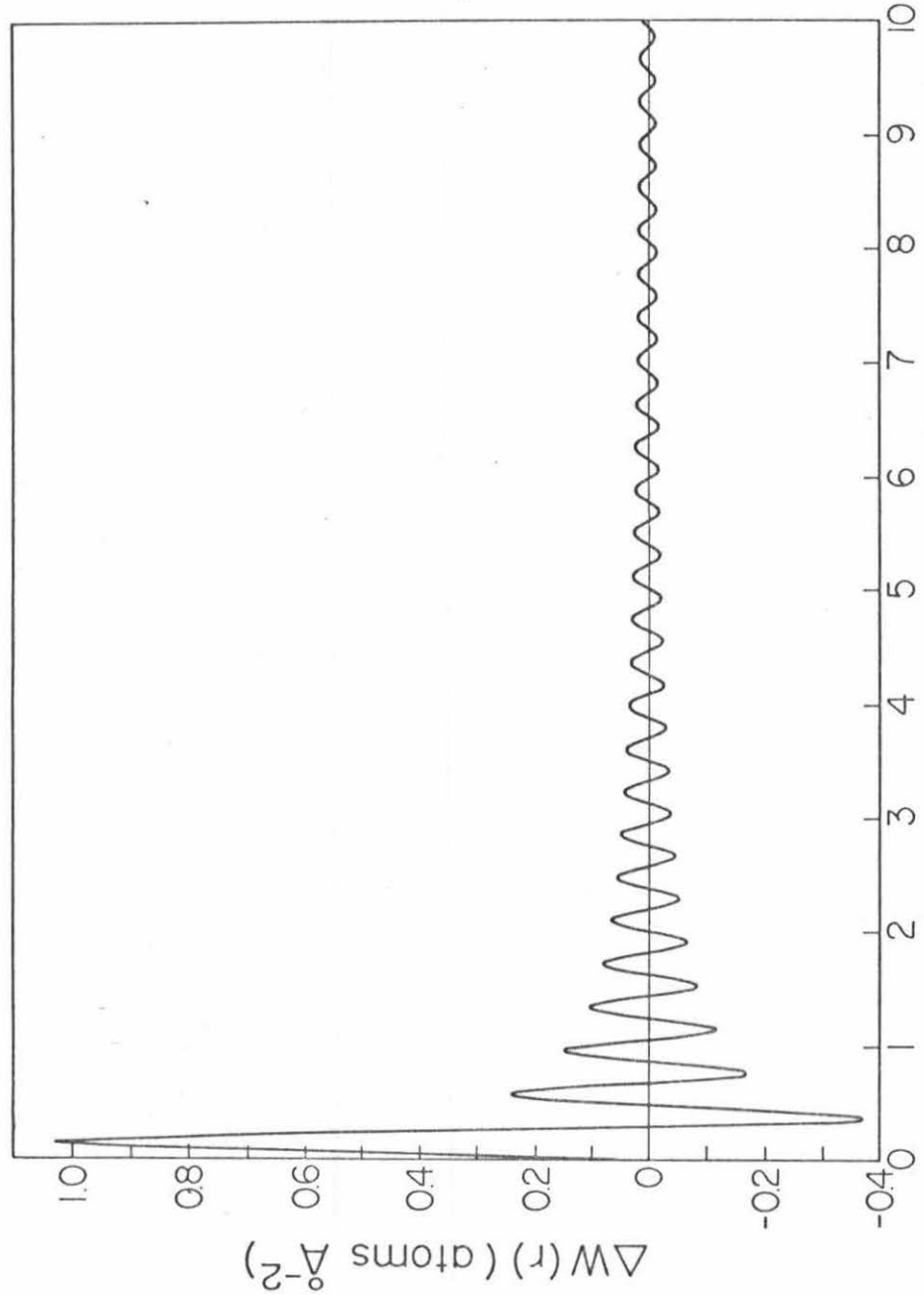

Fig. 3. Effect of 1% deviation in normalization factor of $(Pd_{75}Mn_{25})_{77}P_{23}$ on the atomic distribution function

3. It will be seen that the termination errors add to the normalization error at high values of r only.

As far as normalization is concerned, a remark found in $(Pd_{83}Mn_{17})P_{23}$ (Fig. 15) should be noted. In this case a peak noticeable at $r = 3.70\text{Å}$ remains and is not due to an erroneous normalization, as it is not located at the beginning of the decreasing slope and, as will be seen later, is not due to the cut-off of the interference function as the effects of this phenomenon are satellites of decreasing amplitude as we move further off the first peak in both directions, so this can be attributed only to a new parasitic phenomenon which is a defective experimental intensity datum.

3. Influence of the Termination Errors on I(K) and W(r)

The Fourier integration of the interference function $I(K)$ ends for $K =$ experimental K_{max}. Mathematically, the integration from zero to infinity is acting on the product of the interference function $I(K)$ multiplied by a function $M(K)$ such as $M(K) = 1$ for $K \geq K_{max}$ and $M(K) = 0$ for $K > K_{max}$. Or a characteristic of the Fourier transform is that the transform of the product of two functions is equal to the product of convolution of the transform of the two functions.

$$\text{Transf } I(K) \cdot M(K) = \text{Transf } I(K) \otimes \text{Transf } M(K)$$

The transform of $M(K)$ is of the form

$$T(r) = \frac{\sin(2\pi Kr)}{2\pi Kr} \times \text{constant} \qquad (19)$$

Therefore the consequence of the termination phenomenon is to make appear on each side of every maximum in $W(r)$, a series of secondary maxima of periodicity $1/K_{max}$.

a. Method used to reduce the termination errors

Until recently[7,39] the method was to multiply $I(K)$ by a function e^{-A^2} before doing the Fourier transform. This had the effect of damping $W(r)$ more or less rapidly depending on the chosen value of A . The thermal vibration of the sample obeys a similar function. For this reason this factor is called the artificial coefficient of temperature. The effect of such a manipulation is shown in Fig. 4(D) and it is noticed that although the satellites have completely disappeared on $W(r)$ the stripes have been enlarged drastically with loss of intensity. It is conceived, therefore, that with this technique meaningful details have been eliminated which could be extremely useful if the atomic function was cleared from normalization and termination errors; otherwise the information becomes extremely elusive.

To this unsatisfactory method, two methods are preferred. The first one is very tedious as its basic concept is the following:

Let $I_1(K)$ be a known experimental interference function, known until K_{max} ; its Fourier transform is $W_1(r)$. Suppose that the normalization correction has been done and that in the interval between $0 < r < r_1$ first nearest neighbors, some parasitic oscillations persist, coming from the termination effect. Let us replace the beginning by a straight line that joins the bottom of the first maximum peak and goes through the middle of most of the oscillations. Let $I_2(K)$ be

Figure 4

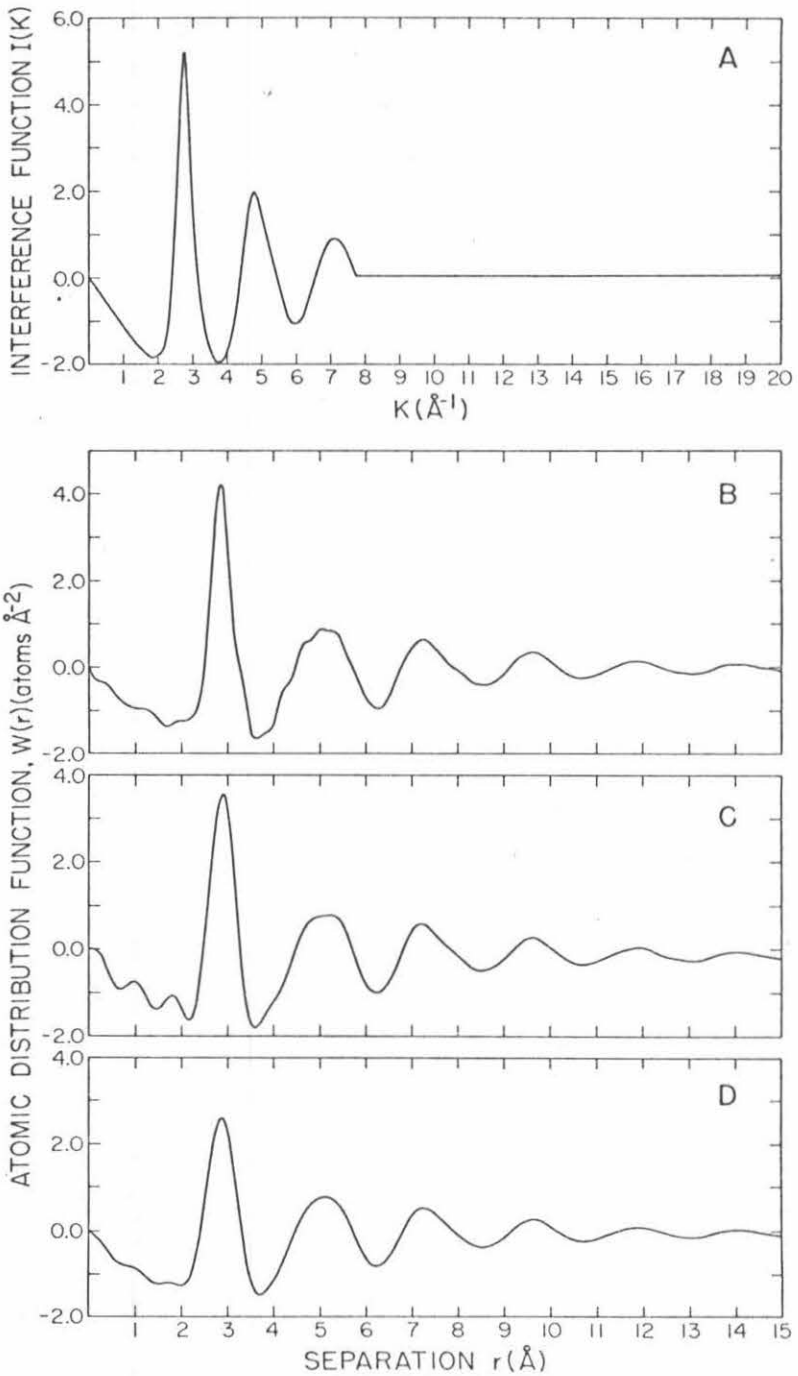

A - Interference function of $(Pd_{75}Mn_{25})_{77}P_{23}$ cut at k=7.8 to show the effect of termination error.

B - Atomic distribution function of $(Pd_{75}Mn_{25})_{77}P_{23}$ from interference function with k=20 .

C - The effect of termination on the atomic distribution function when k=2 .

D - Same curve as "C" after multiplying its interference function by $e^{-(0.02K^2)^{max}}$

this modified function. The inverse transform of $W_2(r)$ is done to obtain $I_2(K)$. It is noticed consequently that $I_2(K)$ is different from $I_1(K)$ in two ways:

1) for $K < K_{max}$: $I_2(K)$ is not superimposable to $I_1(K)$ as the suppression of the parasites on $W_1(r)$ contains an indetermination as to the point where the ideal slope meets the bottom of the first peak.

2) for $K > K_{max}$: $I_2(K)$ contains an extension made of oscillations slowly decreasing in intensity and could be considered a make up for the cut-off error.

This method is extremely useful to extract information that gets mixed up with the parasitic effect beyond the first peak.

The parasitic undulations are then eliminated from $W_1(r)$ by varying the amplitude of the calculated satellites.

The second method is to give $I(K)$ above $K = 17.2$ more and more close values to zero as the K limit boundary is approached.

4. Choice of the Interval ΔK in the Numerical Integration

It has been proved[40] that the substitution of the integral by a summation leads to a periodic Fourier transform function of period $1/\Delta K$ that goes to zero at $r = m \frac{1}{2\Delta K}$. Outside the interval $(-\frac{1}{2\Delta K}, \frac{1}{2\Delta K})$ the function repeats itself identically to what it is inside the interval. It therefore becomes convenient to choose the distance r until which the information is desirable, and ΔK can be deduced easily. For this work, the study is carried up to $r = 20\text{Å}$

$$r_{min} = \frac{1}{2\Delta K_{max}}$$

$$K_{max} = \frac{1}{2 \times 20\text{Å}} = 0.025\text{Å}^{-1}$$

but ΔK was chosen as 0.01Å^{-1} so as to insure that the information is as precise and as original as possible until 20Å.

5. Remarks on Compton Scattering Effect

The incoherent scattering of Pd, Mn, and P in amounts proportional to their respective percentages had to be subtracted. The gaseous scattering factors were used, in spite of our awareness of the fact that they differ experimentally from their sum effect in the solid. Three models are possible to take account of the Compton scattering:

(1) The Mn, Pd and P are totally segregated

(2) The P, Mn, Pd form an ideal disordered solution. In this case the phosphorus is randomly distributed and it is proved[41] that the scattering power is made of two terms

$$\overline{I(\vec{K})} = N\{\overline{f_n^2} - (\overline{f_n})^2\} + (\overline{f_n})^2 \{N + \sum \sum \overline{\cos(\vec{K}_{nn'})}\}$$

$\overline{f_n}$ being the scattering factor of a fictitious atom whose scattering factor is equal to the average of the scattering factors of Pd, Mn, P, taken into account percentage-wise. $N\{\overline{f_n^2} - (f_n)^2\}$ is the additional Compton scattering due to the difference in scattering factors between scattering

centers.

(3) Mn, Pd and P form a solid solution but the atoms of phosphorus are not randomly distributed. In this approach the diffracted intensity varies according to the arrangement of the three types of atoms, one with respect to the others. If N_{Mn}, N_{Pd} and N_P are the number of atoms of manganese, palladium and phosphorous, respectively, and f_{Mn}, f_{Pd} and f_P are their scattering factors, it could be assumed that $[N_{Mn}(N_{Mn}-1)]/2]$ couples of Mn-Mn are affected by the $(f_{Mn})^2$ factors, $N_{Mn} \times N_P$ couples of Mn-P with the coefficient $f_{Mn} \times f_P$, and $[N_P(N_P - 1)]/2$ couples P-P with the coefficient $(f_P)^2$, etc. But as it is not possible to identify which of the nine pairs mentioned above contributes most, and if the diffracted intensity is taken into consideration, the interference function could be written as

$$I(K) = \frac{I(K)_{scatt}}{N_{Mn}f_{Mn}^2 + N_{Pd}f_{Pd}^2 + N_P f_P^2} \qquad (20)$$

6. Magnitude of Thermal Vibration Effect

As seen, the thermal vibration modifies the interference function by a factor e^{-AK^2}. To have an idea of the orders of magnitude involved let us calculate the value of the constant "A" for palladium at 20^oC (293^oK).

The scattering factor for an element at the temperature T is modified with respect to its value f_R calculated at an angle θ by

the following relation

$$f_T = f_R \exp\left\{-\frac{B \sin^2\theta}{\lambda^2}\right\} \tag{21}$$

B is the Debye factor for this element. It is constituted of two terms

$$B = B_o + B_T \tag{22}$$

B_o corresponds to the thermal agitation, not zero, at zero degrees absolute, and B_T is the temperature factor. The International Tables give for palladium at 20^oC: $B = 0.105 + 0.365 = 0.470$; and as

$$f_T = f_R \exp - \frac{B}{4} K^2 \tag{23}$$

the obtained damping factor is

$$f_T = f_R \exp^{-0.235\ K^2}$$

This has enlarged all the peaks of $W(r)$ while their amplitudes were diminished.

7. Method Used for Density Determination of Amorphous Thin Foils (Experiments done by P. S. Schluter)

This method requires the knowledge of three weights: the weight of the specimen in air, W_A ; the weight of the specimen and its support wire while suspended in a liquid of known density (toluene), W_T ; the weight of the support wire while suspended in the toluene W_S , as well as the density of toluene (0.96694 gm/cc at 20^oC). The weight of the specimen alone in the toluene can be obtained by subtracting $(W_S - W_T)$. This difference is subtracted from the weight of the

specimen in air (W_A), yielding an equivalent weight of the toluene displaced by the volume of the specimen. As the density of the toluene is known, one can calculate the volume of the specimen and thus obtain the density:

$$\text{Experimental Density} = W_A / \{[W_A - (W_T - W_S)] / D\}$$

a. Procedure

The maximum size of the sample was limited by the size of the glass vial that contains the toluene, which was 1.4 cm diameter and 2.2 cm cylindrical height. Its weight was about 100 mg for optimum accuracy on the Cahn electrobalance. A small hole of the order of 1 mm diameter or smaller was drilled in the specimen to accommodate the supporting wire. All thin flaky sections of the specimen were removed so that no break-off during the weighting and immersion of the sample in the toluene occur. The specimen and suspension wire were thoroughly cleaned with proper solvents to remove any glue or cement residues and rinsed with suitable reagent grade solvent. Finally the specimen was dried in vacuum for a few hours to evaporate the last trace of the solvents.

During all phases of weighing and immersion the specimen and suspension wire were handled with a pair of forceps. After the free air weight of the specimen was determined, the specimen was suspended from its support hook. This wire was not over 2 mil in diameter and was absolutely free of any kinks and as straight as possible. The handling of the wire was made at either end and never in the middle section which interacts with the surface of the toluene. About 20 ml

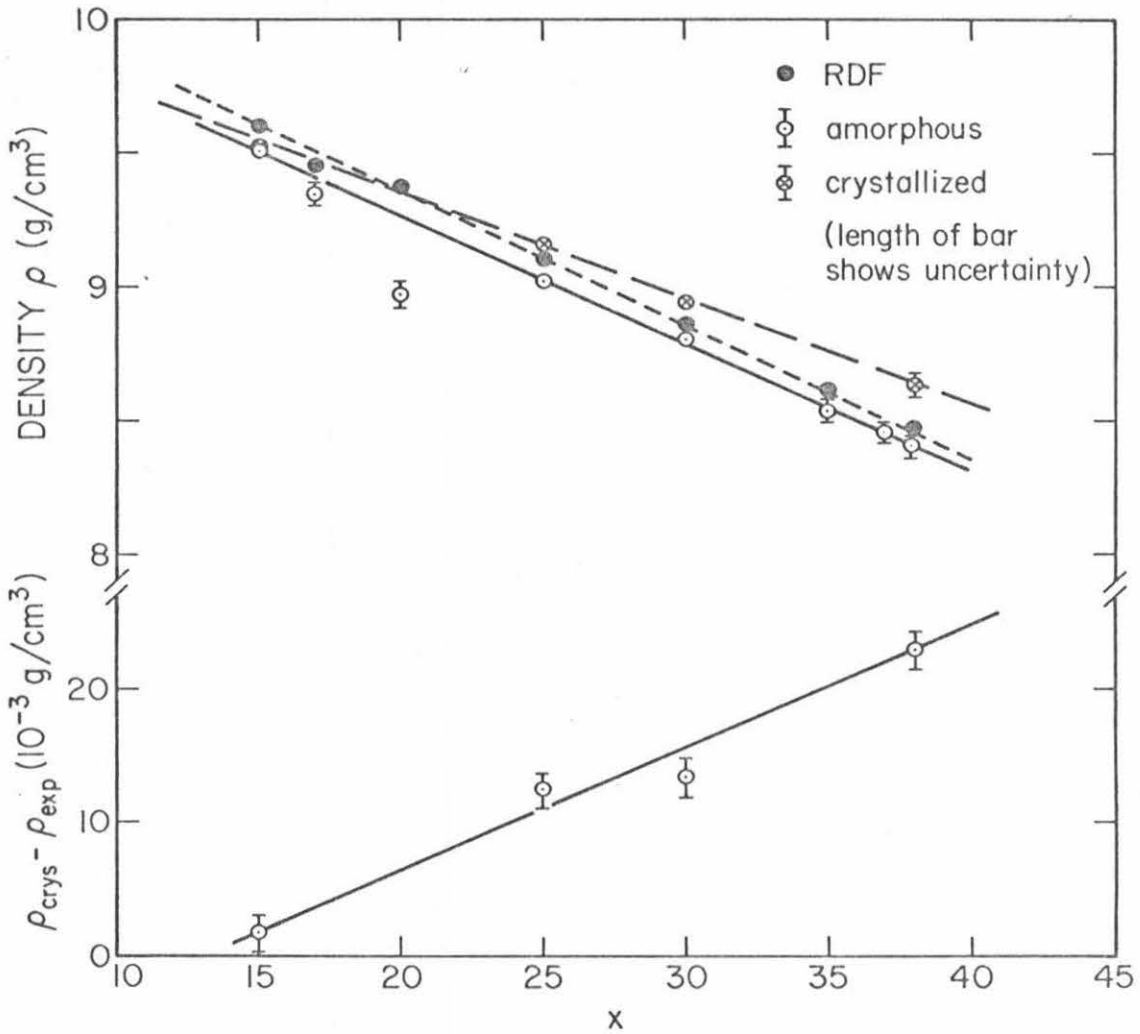

Fig. 5. Manganese concentration x (at.%) in $(Pd_{100-x}Mn_x)_{77}P_{23}$

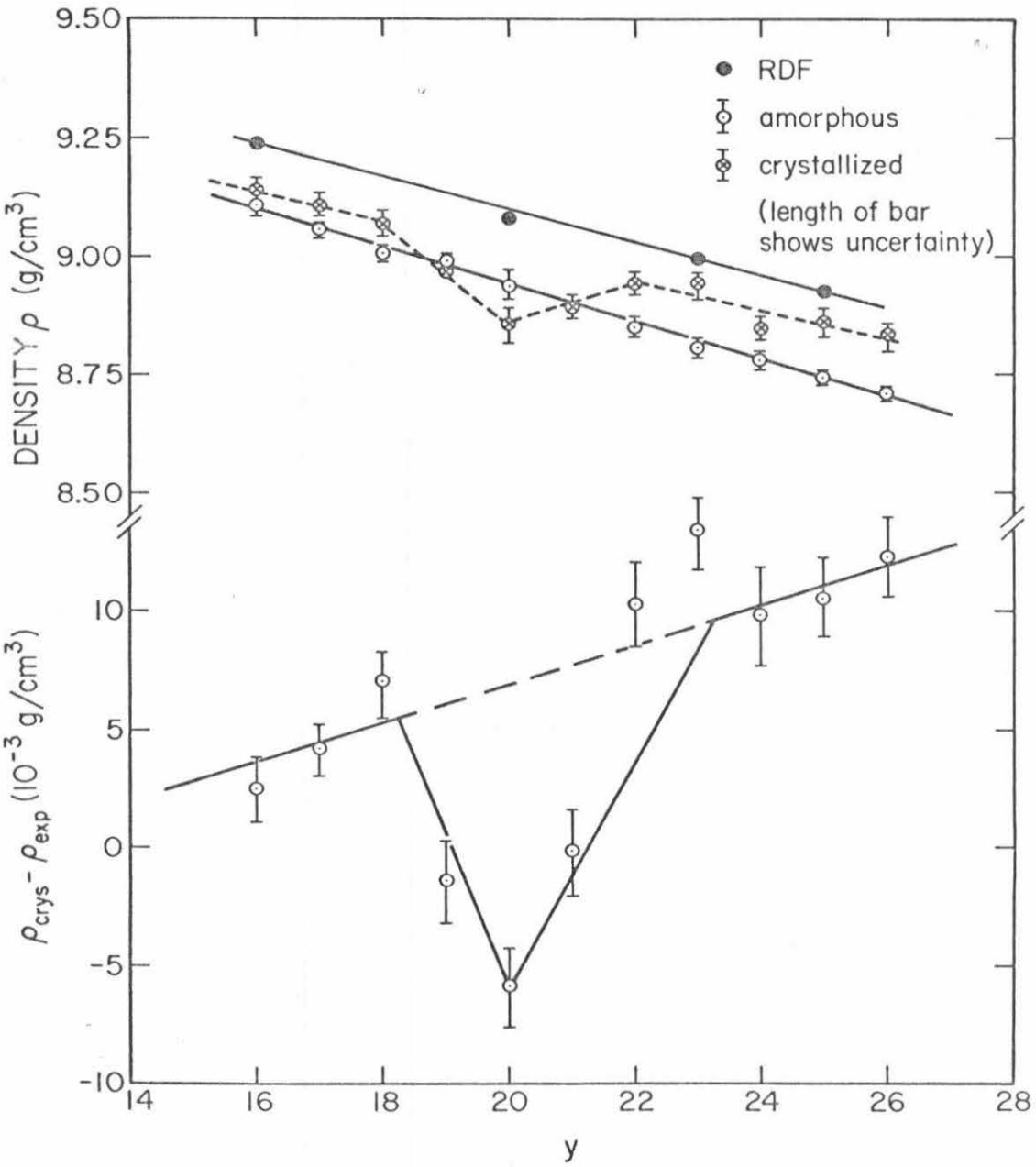

Fig. 6. Phosphorus concentration "y" at.%P in $(Pd_{70}Mn_{30})_{100-y}P_y$

of degassed reagent grade toluene was poured into the dispenser flask before applying a vacuum to the system, so as to prevent any air from entering the vacuum system. The purpose of this is to insure that only toluene molecules are present in the vacuum system and that toluene will fill every tiny crack and pore of the specimen, enhancing the accuracy of the determination. The results are listed in Tables IV and V, and a graphical representation is shown in Figs.5 and 6.

b. Estimate of errors

The greatest contribution of error arises from the surface tension on the support wire. This adds almost 200 μg to the measured mass of a wire 1 mil in diameter, an effect that represents a 10% error in the density determination. Hopefully some of this surface tension effect was cancelled when the wire in toluene measurement was subtracted from the wire plus specimen in toluene measurement. So this error might not be that large. Much care was devoted to this phase of the experiment, and due to the nonquantitative nature of this possible error source it was not included in the conventional error analysis, hoping that this neglect would be balanced by the care exercised during the experiment. The four sources of uncorrelated uncertainties in the measurements were 1) each balancing was executed to an accuracy of ±3 μg in terms of the null dial reading; 2) the linearity of the nulling system was taken to be within ±0.025% full scale (5 mg); 3) class M weights were used for "taring weights"; each might include an error of ±5.4 μg; 4) the density of degassed toluene at 25°C was within ±0.1% of the published value of 0.86694 at 70°C. The error due to the tolerance on class M weights

Table IV. Density Measurements for $(Pd_{100-x}Mn_x)_{77}P_{23}$

ALLOY COMPOSITION	RDF	EXPERIMENTAL		CRYSTALLIZED		$\rho_{crys} - \rho_{exp}$
	$\rho(g/cm^3)$	$\rho(g/cm^3)$	uncertainty	$\rho(g/cm^3)$	uncertainty	$(10^{-3} g/cm^3)$
$(Pd_{85}Mn_{15})_{77}P_{23}$	9.601	9.512	0.0253	9.528	0.0254	0.016
$(Pd_{83}Mn_{17})_{77}P_{23}$	9.462	9.357	0.0369			
$(Pd_{80}Mn_{20})_{77}P_{23}$	9.374	8.988	0.0306			
$(Pd_{75}Mn_{25})_{77}P_{23}$	9.116	9.031	0.0213	9.147	0.0243	0.116
$(Pd_{70}Mn_{30})_{77}P_{23}$	8.861	8.800	0.0379	8.937	0.0312	0.137
$(Pd_{65}Mn_{35})_{77})_{23}$	8.639	8.549	0.0223			
$(Pd_{63}Mn_{37})_{77}P_{23}$	-	8.460	0.0201			
$(Pd_{62}Mn_{38})_{77}P_{23}$	8.483	8.413	0.0230	8.643	0.0261	0.230

Table V. Density Measurements for $(Pd_{70}Mn_{30})_{100-y}P_y$

ALLOY COMPOSITION	RDF	EXPERIMENTAL		CRYSTALLIZED		$P_{crys} - P_{exp}$
	$\rho(g/cm^3)$	$\rho(g/cm^3)$	uncertainty	$\rho(g/cm^3$	uncertainty	$(10^{-3}g/cm^3)$
$(Pd_{70}Mn_{30})_{84}P_{16}$	-	9.106	0.0191	9.131	0.0280	+0.025
$(Pd_{70}Mn_{30})_{83}P_{17}$	-	9.066	0.0311	9.108	0.0319	+0.042
$(Pd_{70}Mn_{30})_{82}P_{18}$	9.236	9.0022	0.0188	9.072	0.0134	+0.070
$(Pd_{70}Mn_{30})_{81}P_{19}$	-	8.991	0.0497	8.977	0.0495	-0.014
$(Pd_{70}Mn_{30})_{80}P_{20}$	9.073	8.915	0.0308	8.856	0.0243	-0.059
$(Pd_{70}Mn_{30})_{79}P_{21}$	-	8.894	0.0299	8.892	0.0275	-0.002
$(Pd_{70}Mn_{30})_{78}P_{22}$	-	8.844	0.0201	8.946	0.0158	+0.102
$(Pd_{70}Mn_{30})_{77}P_{23}$	8.992	8.800	0.0379	8.937	0.0312	+0.137
$(Pd_{70}Mn_{30})_{76}P_{24}$	-	8.778	0.0473	8.875	0.0334	+0.097
$(Pd_{70}Mn_{30})_{75}P_{25}$	8.921	8.748	0.0307	8.853	0.0488	+0.105
$(Pd_{70}Mn_{30})_{74}P_{26}$	-	8.715	0.0322	8.837	0.0279	+0.122

Table VI. Crystallite Size of Pd-Mn-P

Alloy	(Å) MoK_α	(Å) CuK_α
$(Pd_{85}Mn_{15})_{77}P_{23}$	-	14.344
$(Pd_{83}Mn_{17})_{77}P_{23}$	11.739	16.234
$(Pd_{80}Mn_{20})_{77}P_{23}$	11.592	14.329
$(Pd_{75}Mn_{25})_{77}P_{23}$	10.082	13.569
$(Pd_{70}Mn_{30})_{77}P_{23}$	10.192	13.051
$(Pd_{65}Mn_{35})_{77}P_{23}$	11.278	12.819
$(Pd_{63}Mn_{37})_{77}P_{23}$	11.142	12.550
$(Pd_{62}Mn_{38})_{77}P_{23}$	-	12.126
$(Pd_{70}Mn_{30})_{83}P_{17}$	-	15.629
$(Pd_{70}Mn_{30})_{82}P_{18}$	11.213	14.858
$(Pd_{70}Mn_{30})_{81}P_{19}$	-	14.536
$(Pd_{70}Mn_{30})_{80}P_{20}$	10.920	13.910
$(Pd_{70}Mn_{30})_{79}P_{21}$	-	13.728
$(Pd_{70}Mn_{30})_{78}P_{22}$	-	13.337
$(Pd_{70}Mn_{30})_{77}P_{23}$	10.192	13.051
$(Pd_{70}Mn_{30})_{76}P_{24}$	-	13.258
$(Pd_{70}Mn_{30})_{75}P_{25}$	9.914	13.375
$(Pd_{70}Mn_{30})_{74}P_{26}$	-	13.220
$(Pd_{62}Mn_{38})_{75}P_{25}$	-	12.937

Table VII. Crystallite Size of Pd-Co-P

Alloy	(Å) CuK_α
$(Pd_{85}Co_{15})_{80}P_{20}$	14.896
$(Pd_{80}Co_{20})_{80}P_{20}$	14.402
$(Pd_{75}Co_{25})_{80}P_{20}$	12.758
$(Pd_{70}Co_{30})_{80}P_{20}$	12.613
$(Pd_{65}Co_{35})_{80}P_{20}$	12.332
$(Pd_{60}Co_{40})_{80}P_{20}$	12.297
$(Pd_{55}Co_{45})_{80}P_{20}$	12.078
$(Pd_{50}Co_{50})_{80}P_{20}$	11.640

were correlated to the non-common tare weights for both W_A and W_T measurements which were taken to be the multiplying factor for the class M tolerance. Every other error was considered uncorrelated and the total uncertainty was calculated to be in the form,

$$\sigma_x^2 \simeq \sigma_u^2\left(\frac{\sigma x}{\sigma u}\right)^2 + \sigma_v^2 + \sigma_v^2\left(\frac{x}{v}\right)^2 + \sigma_w^2\left(\frac{\sigma x}{\sigma w}\right)^2 + \cdots$$

8. Attempt to Estimate the Crystallite Size of Pd-Mn-P and Pd-Co-P Amorphous Systems

From the width of the first diffraction peak, which is related to the crystallite size assuming a microcrystalline model by a relation known as Scherrer formula

$$t = \frac{0.9\lambda}{B \cos \theta_B}$$

where B is the broadening of diffraction line (radians) and t is the diameter of the crystallites. The results are shown in Tables VI and VII.

9. Coordination Number

Using the radial distribution data g(r) it is possible to compute the coordination number CN for the amorphous metallic alloys Pd-Mn-P. Four methods are available in the literature and are used by different workers in the field:

a. symmetrizing the first peak in rg(r)

b. symmetrizing the first peak in $r^2g(r)$

c. decomposition of $r^2g(r)$ into shells

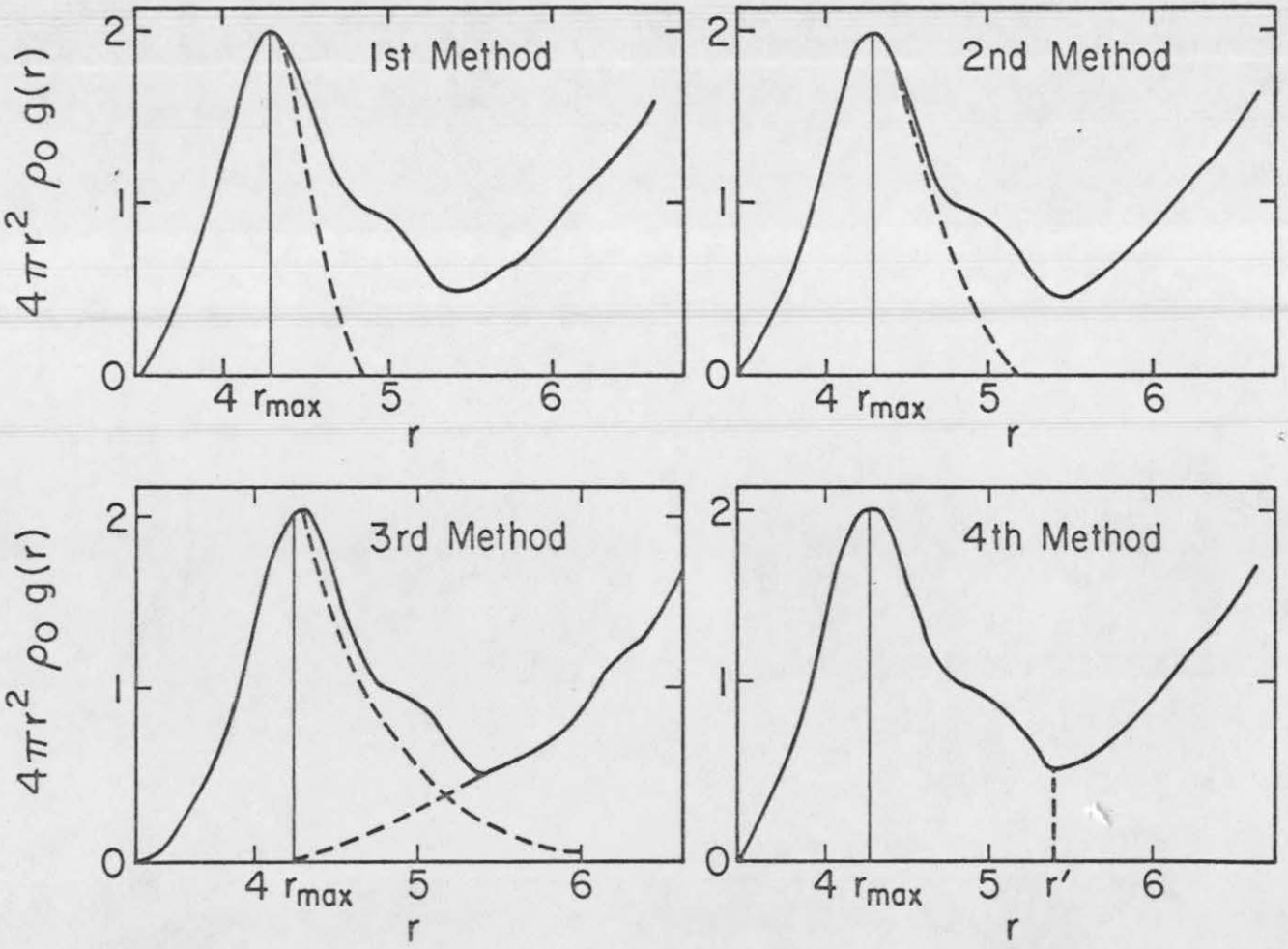

Fig. 7. Plots of $4\pi r^2 \rho_o$ g(r) vs. r showing the four methods for computing the coordination number.

d. computation of the area to the first minimum in $r^2g(r)$

In the hope of clarifying some of the confusion about this quantity, the following remarks will be made for consideration as an incentive to standardize the CN computations in future investigations of amorphous alloys.

Method (a) is based on the fact that $rg(r)$ is a symmetric function which has been disproved for many cases[42]. Method (b) is based on the assumption that the coordination shells are symmetric about a radius, which is called r_{max} in $r^2g(r)$. To resolve the asymmetry it is suggested[43] to fit the $r^2g(r)$ to a Gaussian which is not without errors, as the trailing edge of the first peak in $r^2g(r)$ extends beyond the symmetrical value of $r_B + \Delta r$ and any reasonable extrapolation gives a value of CN which is significantly larger than the symmetric $r^2g(r)$ value. Method (c) although the most objective in concept, as it attempts to decompose the total distribution function into its constituent shells, is the least objective in arriving at a precise value of CN. The reason for this is that the individual shells overlap to such an extent that there is no unique way to resolve them. Thus, the CN may easily vary by 20% depending upon how the separate coordination shells are constructed. For liquids near their melting point, the extrapolation of the first peak trailing edge presents no serious problems, but for dense liquids or amorphous alloys the decomposition of the total distribution function into its component shells is far from obvious. Thus the evaluation of CN by this method is stronger in favor of a philosophical approach than a practical one.

Method (d) offers a compromise between a more realistic definition and a more objective means of computation. It explains and justifies the definition of CN to be the average number of atomic centers to be found at some distance $\pm\delta r$ from a central point taken at random in the media: solid, liquid, or gas. The CN is determined by evaluating the integral $4\pi r^2\rho_o\, g(r)$ out to a distance r' corresponding to the first minimum on the high r side of the first peak. By so defining CN, the fact that the nearest neighbor particles are more likely to stray outward from their equilibrium position than inward toward the central or reference particle is recognized. The advantage of this method is that the characteristic distance r' may be precisely determined, thereby giving an unambiguous value of CN. Therefore, other than for comparative studies the value associated with the area under the first peak of the function $4\pi r^2\rho_o g(r)(\sum x_i K_i)^2$ is used, where ρ_o is the average number density. A graphical comparison between the four methods is shown in Fig. 7 and the results are listed in Tables VIII and IX. Figure 8 represents a sample of $g(r)$ showing the limits of integration of the calculation for the coordination number.

10. Direct Correlation Function

Goldstein[44] established that $C(r)$ could be rigorously computed from the Fourier transform of a function experimentally obtained from x-ray diffraction data by the following relation

$$C(r_{12}) = h(r_{12}) - \rho \int c(r_{13})\, h(r_{23}) dr_3 \qquad (24)$$

where $C(r)$ is the direct correlation function (DCF), $h(r) = g(r) - 1$ also called the net radial distribution function (NRDF) and ρ is the

Table VIII. Results and Comparative Features of the Coordination Number Calculations

$(Pd_{75}Mn_{25})P_{23}$	CN(atoms)
1st Method	11.54 ± 0.1
2nd Method	12.03 ± 0.4
3rd Method	12.37 ± 0.4
4th Method	12.46 ± 0.3

Table IX. Coordination Number for Pd-Mn-P Amorphous Alloys

Composition	4th Method ρ_o(atoms/Å^3)	CN CN(first)
$(Pd_{85}Mn_{15})_{77}P_{23}$	0.06759	12.53
$(Pd_{83}Mn_{17})_{77}P_{23}$	0.06765	12.32
$(Pd_{80}Mn_{20})_{77}P_{23}$	0.06778	12.36
$(Pd_{75}Mn_{25})_{77})_{23}$	0.06799	12.46
$(Pd_{70}Mn_{30})_{77}P_{23}$	0.06822	12.64
$(Pd_{65}Mn_{35})_{77}P_{23}$	0.06847	12.68
$(Pd_{63}Mn_{37})_{77}P_{23}$	0.06857	12.70
$(Pd_{70}Mn_{30})_{82}P_{18}$	0.06849	12.69
$(Pd_{70}Mn_{30})_{80}P_{20}$	0.06839	12.67
$(Pd_{70}Mn_{30})_{77}P_{23}$	0.06822	12.64
$(Pd_{70}Mn_{30})_{75}P_{25}$	0.06810	12.62

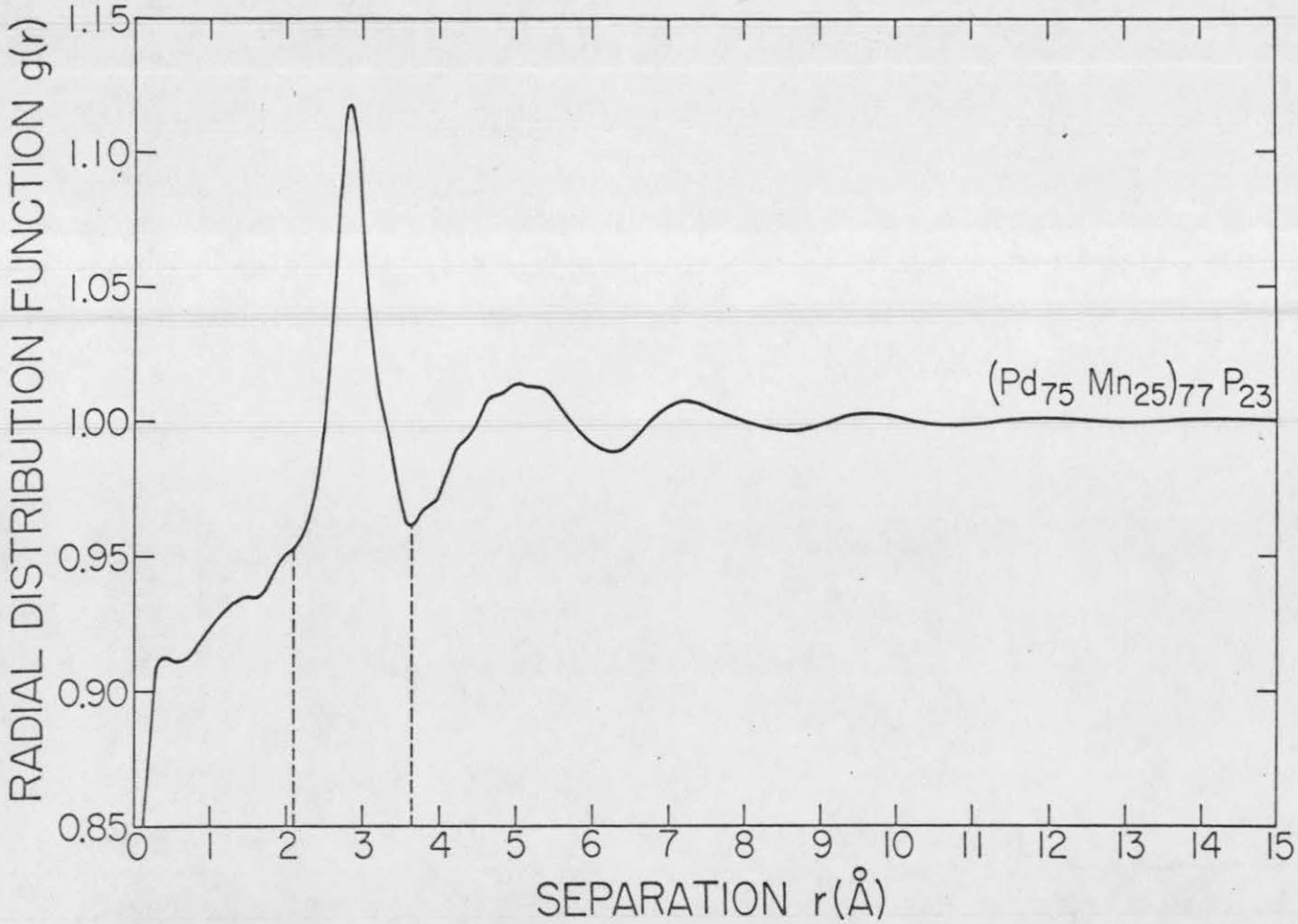

Fig. 8. Radial distribution function of $(Pd_{75}Mn_{25})_{77}P_{23}$ showing the limits of integration for the calculation of the coordination number using method "4".

density. Fisher[45] provided an interpretation that the correlation $C(r_{12})$ between particle 1 and 2 can be regarded as caused by (a) a direct influence of 1 and 2, described by the so-called DCF, $C(r_{12})$, which should be short range and having the range in the pair potential $U(r)$; and (b) an indirect influence propagated directly from 1 to a third particle[46] at r_3 which in turn exerts its total influence on particle 2. The NRDF and DCF are directly related to the observed intensity of scattered radiation as shown by Goldstein[46] and Fisher[45]:

$$h(r) = (2\pi^2 r\rho)^{-1} \int_0^\infty KI(K) \sin(Kr)\, dK \qquad (25)$$

$$C(r) = (2\pi^2 r\rho)^{-1} \int_0^\infty \frac{KI(K)}{[1+I(K)]} \sin(Kr)\, dK \qquad (26)$$

$I(K)$ is the experimentally measured intensity properly normalized and corrected. As shown in equation (26), even small errors in the determination of $I(K)$ for $K \to 0$ leads to substantial errors in the kernel of the Fourier integral. Here as a trial, the net radial correlation function for $(Pd_{75}Mn_{25})_{77}P_{23}$ was derived, Fig. 9, but some uncertainty was encountered as to the real behavior of the experimental data below $2\theta = 12^o$. This uncertainty may have been the contributing factor in the seemingly anomalous behavior observed in the present investigation for $(Pd_{75}Mn_{25})_{77}P_{23}$. It is interesting to notice that similar behavior was observed by Johnson and coworkers[47] in pure metals including Hg, Al and Pb.

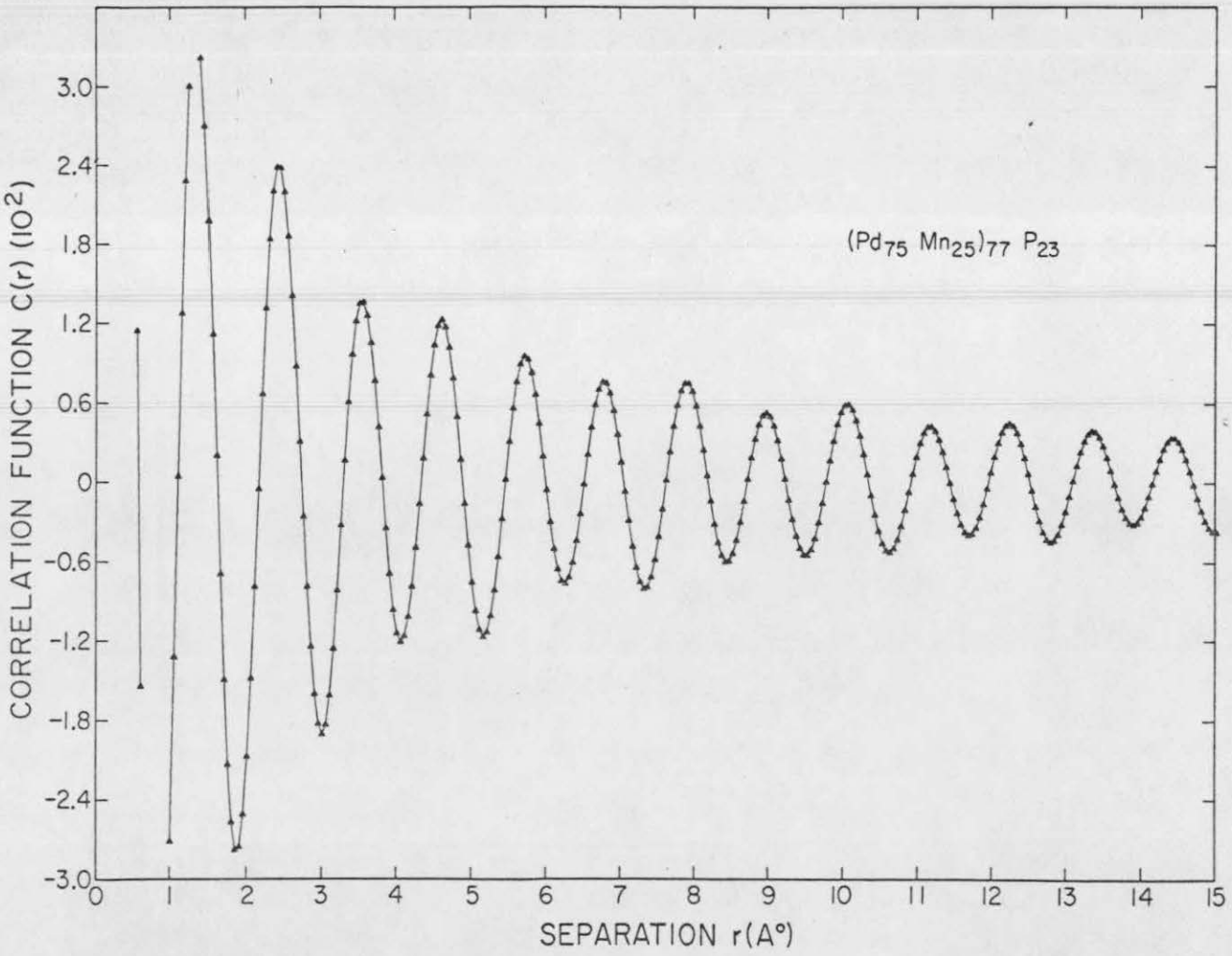

Fig. 9. Net radial correlation function $h(r) = g(r) - 1$ for amorphous $(Pd_{75}Mn_{25})_{77}P_{23}$.

11. Electron Microscopy Analysis

High resolution bright field and electron diffraction microscopy was carried out with a Siemens Elmiscop II. The rapid quenching technique has the advantage of providing foils of uneven thickness (Fig. 10) in which there are regions thin enough for direct observation by transmission electron microscopy without mechanical or chemical thinning. The desired 2000 to 4000Å thin part was cut and put between two copper grids. The instrument was operated under 100 KV and 10 microamp beam current. The effective source diameter was around 5×10^{-5}cm, the illumination angle at the specimen was 5×10^{-6} rad. The method used is based on a suggestion by Kitamura[48] which allows for improvement in angular resolution. For a sample taken at random, in this case $(Pd_{75}Mn_{25})_{77}P_{23}$, the electron diffraction pattern, Fig. 11 reveals a diffused scattered ring perfectly symmetrical, which suggests that for those compounds the structure is clearly disordered and typical of an amorphous structure.

E. Results of the Structure Analysis

1. Palladium-Manganese-Phosphorus Alloys

a. Manganese concentration effect

Seven different compositions of $(Pd_{100-x}Mn_x)_{77}P_{23}$ where $15 \leq x \leq 38$ were investigated by MoK_α x-ray radiation to yield electronic radial distribution function. Several amorphous bands are easily recognizable in the uncorrected diffraction patterns. The coherent intensity curves for the smallest and largest concentrations of manganese are shown in Fig. 12. The maxima following the fourth

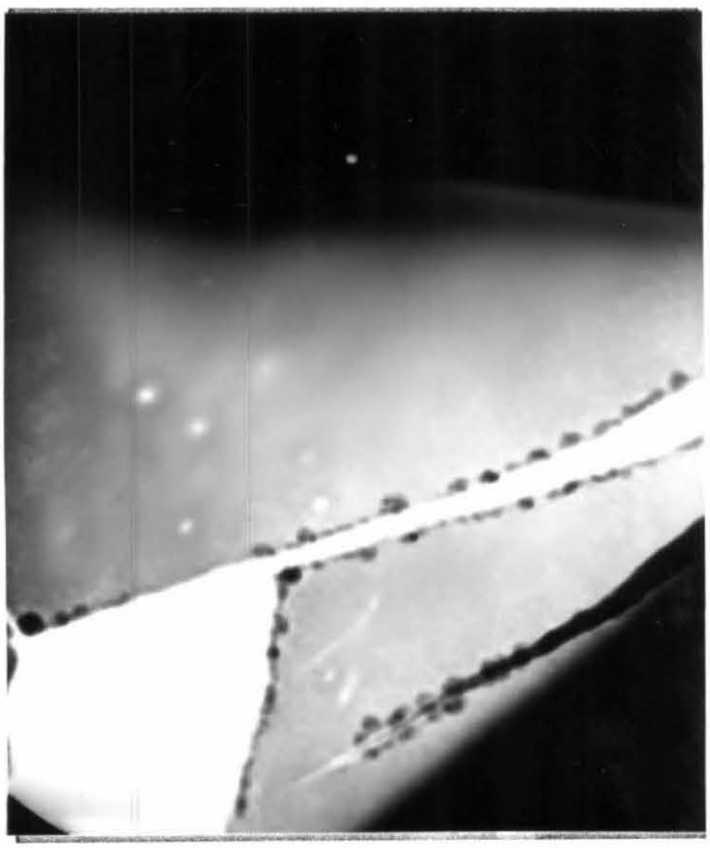

Fig. 10. Transmission electron micrograph of amorphous $(Pd_{75}Mn_{25})_{77}P_{23}$ at the same area of Fig. 11.

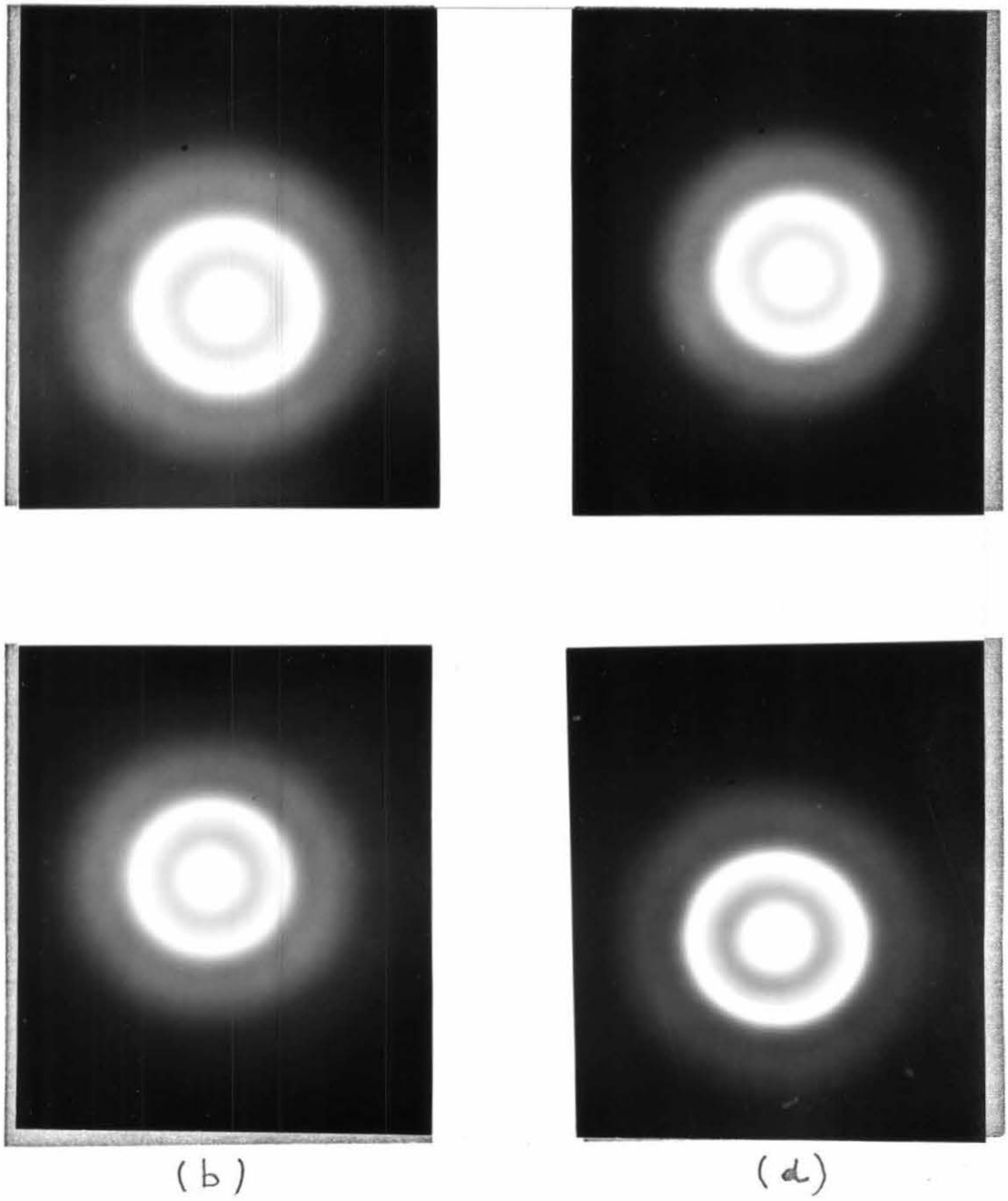

Fig. 11. Transmission electron diffraction pattern of amorphous $(Pd_{75}Mn_{25})_{77}P_{23}$ showing diffused rings characteristic of amorphous alloys. a-b (top area), c-d (specimen tilted).

peak are not visible because of the peak of the figure. On the same figure the average scattering power $\sum_i n_i f_i^2$, corresponding to independent scattering by the atoms of the alloy is shown by the smoothly varying curve, and the resulting interference function I(K) is plotted in Fig. 13. All the numerical results are gathered in Table X. The effect of increasing the manganese concentration results in a decrease in the intensity of the first peak, a broadening of the first and second peaks and a smearing in the high value amorphous bands. It is significant to note that there is no shoulder on the high angle side of the second peak of I(K) . The Fourier inversion was performed according to the method given in III-B.2, after proper correction for the Compton scattering III-C. Special care was taken to reduce the errors due to normalization III-D.2 and termination effect III-D.3. The resulting functions W(r) are shown in Fig. 14, in which we could retain the information contained in the maxima at high angles of the atomic distribution function by using a very small damping factor thus showing interesting details of the short range order. The horizontal line in I(K) and W(r) represent completely uncorrelated structures. Errors in the determination of the normalization constant k show up as spurious ripples in the W(r) plot, especially in the region of low values of r . Judging from the small amplitude of these ripples it may be concluded that this error was not large, thus enabling us to draw a theoretical straight line whose slope is $-4\pi r \rho_o$ to obtain the density of the alloy. A comparison of the atomic distribution function density with the experimental density III-D.7 is shown in Tables IV and V. The atomic radial distribution

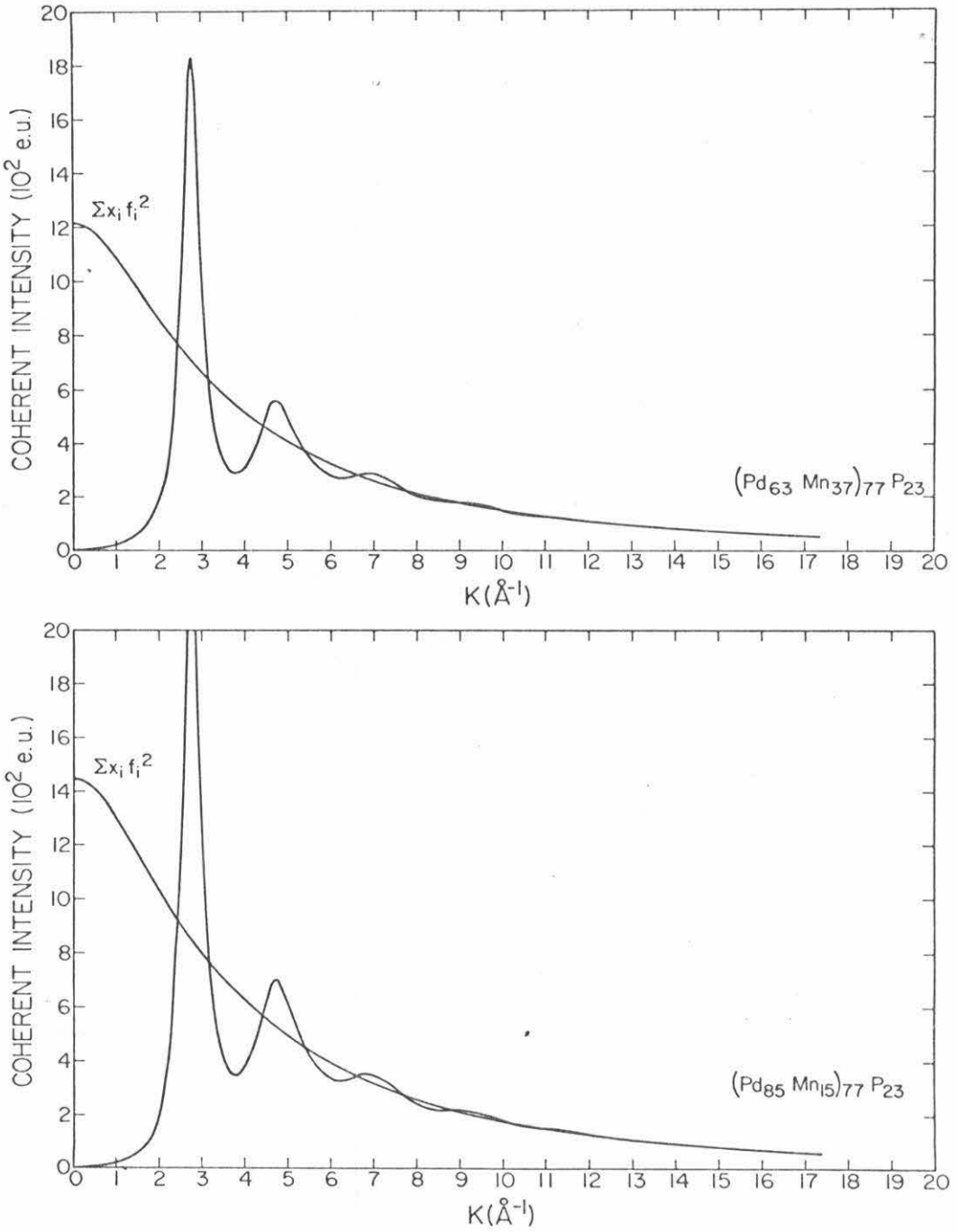

Fig. 12. Coherent scattered intensity from an amorphous $(Pd_{63}Mn_{37})_{77}P_{23}$ and $(Pd_{85}Mn_{15})_{77}P_{23}$ (MoK_α radiation). The smoothly varying curve represents the average scattering power, $\Sigma\ x_m\ f_m^2$, corresponding to independent scattering by the atoms of the alloy.

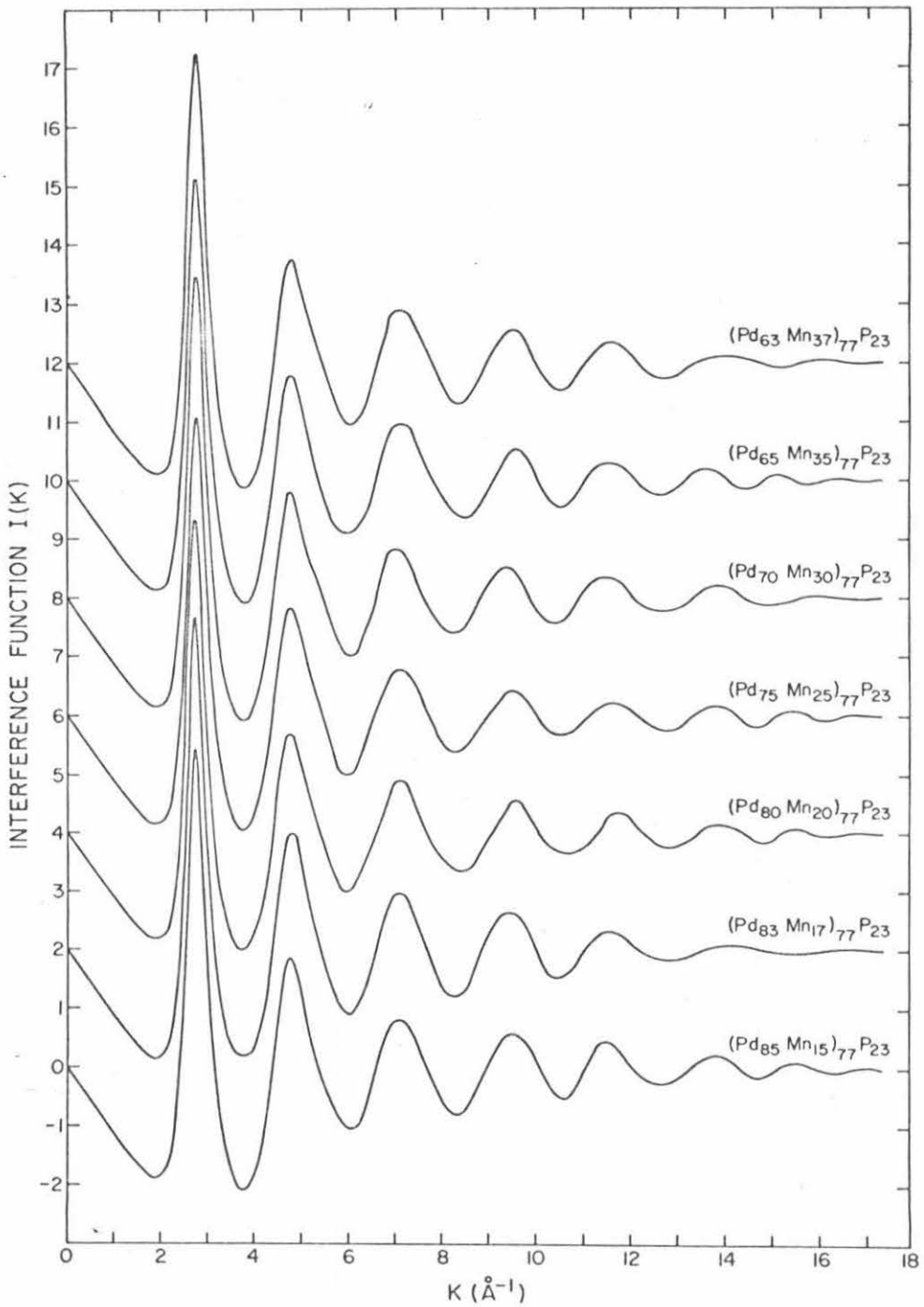

Fig. 13. Interference function I(K) for the amorphous $(Pd_{100-x}Mn_x)_{77}P_{23}$ (with shifted zeros) vs. K ($K=4\pi \sin\theta\lambda^{-1}$). Horizontal line at I(K) = 0 would represent a completely uncorrelated structure.

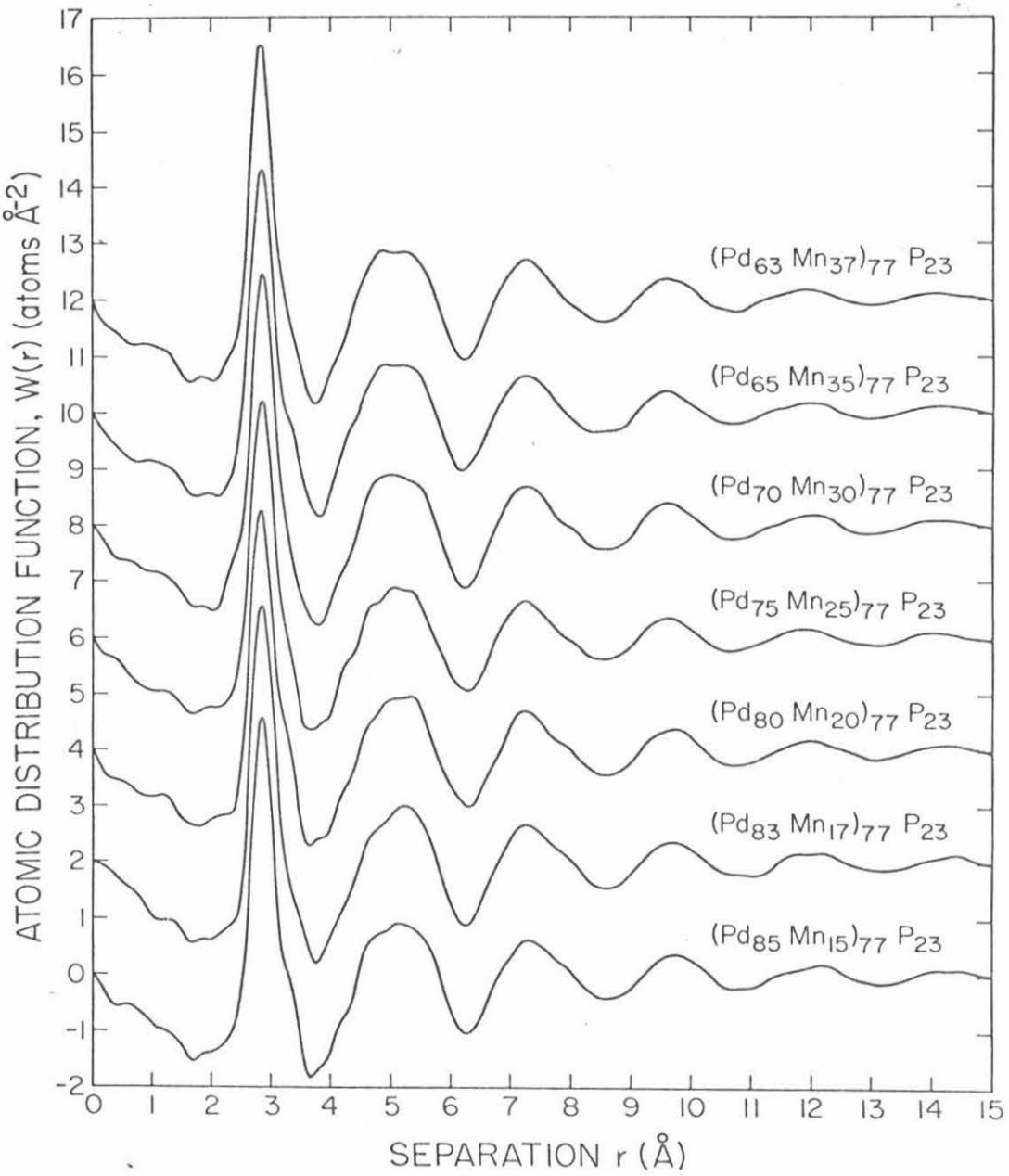

Fig. 14. Atomic distribution function W(r) for amorphous $(Pd_{100-x}Mn_x)_{77}P_{23}$ with shifted zeros.

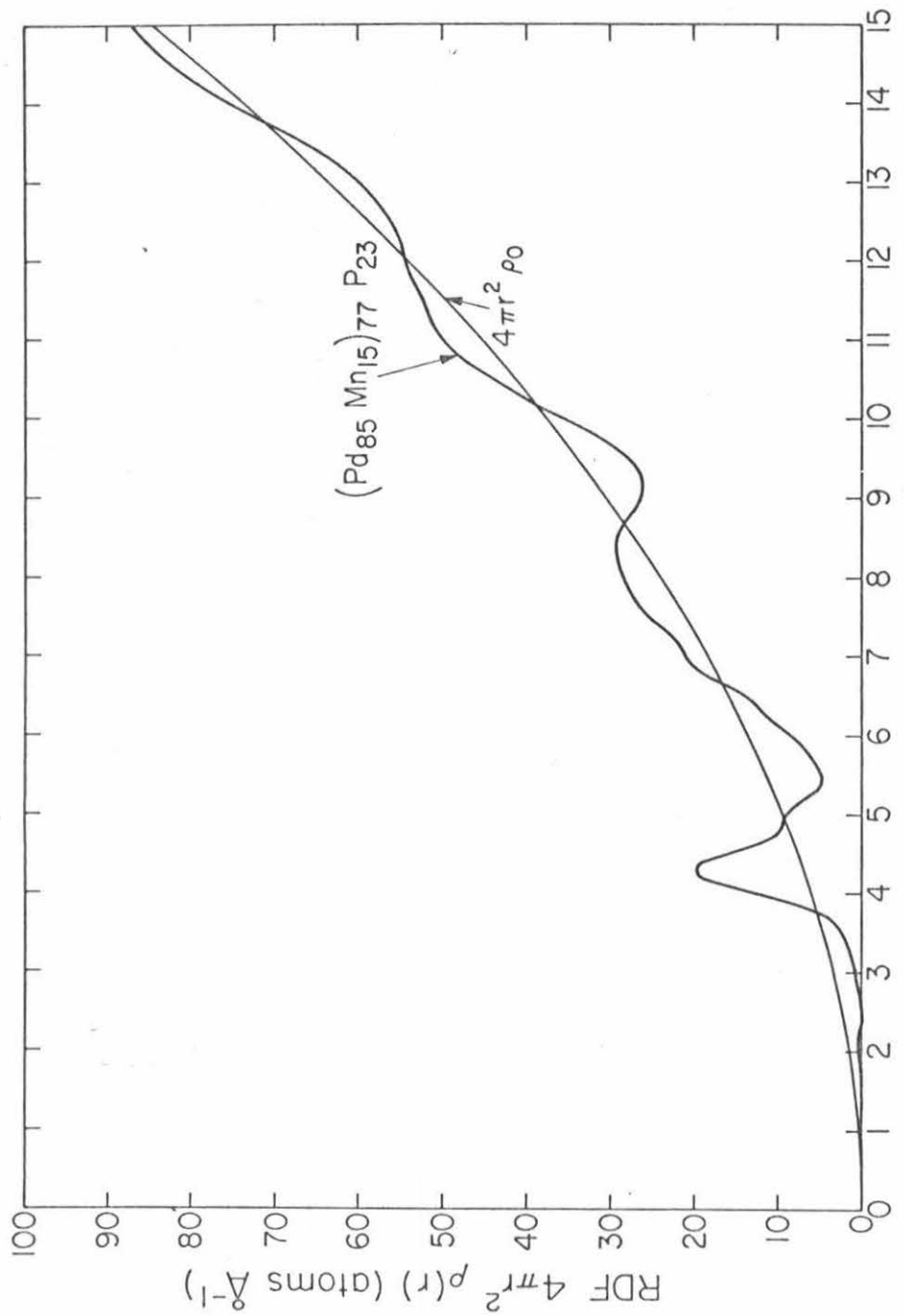

Fig. 15. Radial distribution function (RDF) for a random sample of the $(Pd_{100-x}Mn_x)_{77}P_{23}$ series, namely $(Pd_{85}Mn_{15})_{77}P_{23}$ (oscillating curve). The smoothly rising curve represents the average atomic density $4\pi r^2\rho_o$.

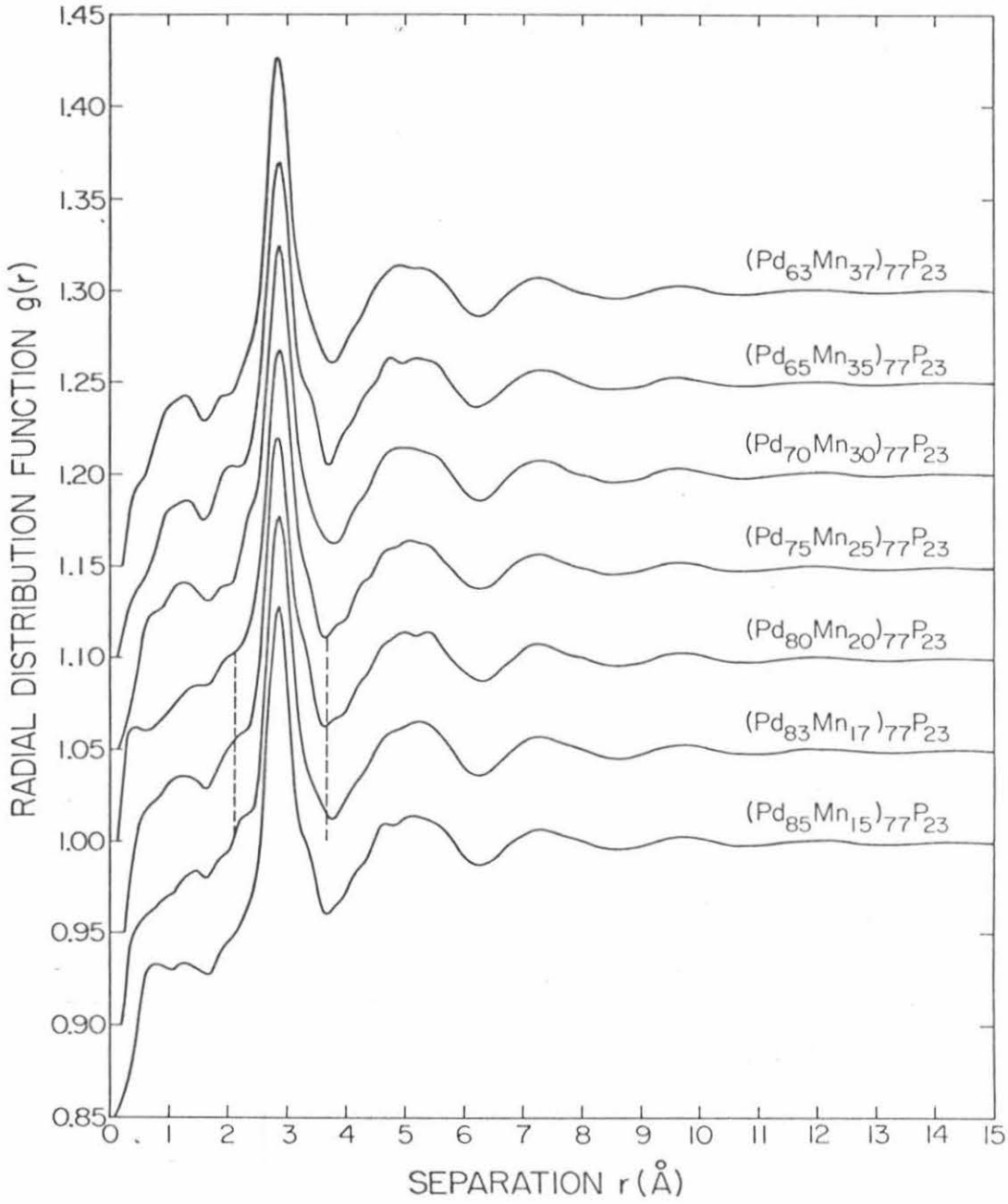

Fig. 16. Radial distribution function g(r) for the amorphous alloy system $(Pd_{100-x}Mn_x)_{77}P_{23}$.

Table X. Structural Results for Amorphous $(Pd\text{-}Mn)_{77}P_{23}$

	Maximum positions in I(K)				Maximum positions in W(r)				
	K_1	K_2	K_3	K_4	r_1	r_2	r_3	r_4	r_2/r_1
$(Pd_{85}Mn_{15})_{77}P_{23}$	2.74	4.75	7.05	9.53	2.84	5.10	7.25	9.70	1.789
$(Pd_{83}Mn_{17})_{77}P_{23}$	2.75	4.78	7.08	9.26	2.84	5.25	7.25	9.70	1.842
$(Pd_{80}Mn_{20})_{77}P_{23}$	2.75	4.78	7.16	9.68	2.85	5.35	7.25	9.75	1.877
$(Pd_{75}Mn_{25})_{77}P_{23}$	2.76	4.78	7.11	9.32	2.85	5.05	7.25	9.65	1.772
$(Pd_{70}Mn_{30})_{77}P_{23}$	2.76	4.78	7.02	9.42	2.85	5.05	7.25	9.65	1.772
$(Pd_{65}Mn_{35})_{77}P_{23}$	2.77	4.75	7.14	9.58	2.86	5.15	7.25	9.60	1.807
$(Pd_{63}Mn_{37})_{77}P_{23}$	2.77	4.81	7.08	9.53	2.86	5.25	7.25	9.60	1.842

Table XI. Relative Positions of Maxima in I(K) and W(r)

	K_i/K_1			r_i/r_1			
Alloy composition	i=1	i=2	i=3	i=1	i=2	i=3	$K_1 \cdot r_1$
$(Pd_{85}Mn_{15})_{77}P_{23}$	1.00	1.73	2.57	1.00	1.79	2.55	7.78
$(Pd_{83}Mn_{17})_{77}P_{23}$	1.00	1.74	2.57	1.00	1.85	2.55	7.82
$(Pd_{80}Mn_{20})_{77}P_{23}$	1.00	1.74	2.60	1.00	1.88	2.54	7.84
$(Pd_{75}Mn_{25})_{77}P_{23}$	1.00	1.73	2.58	1.00	1.77	2.54	7.87
$(Pd_{70}Mn_{30})_{77}P_{23}$	1.00	1.73	2.54	1.00	1.77	2.54	7.87
$(Pd_{65}Mn_{35})_{77}P_{23}$	1.00	1.72	2.58	1.00	1.80	2.53	7.93
$(Pd_{63}Mn_{37})_{77}P_{23}$	1.00	1.74	2.56	1.00	1.83	2.53	7.93

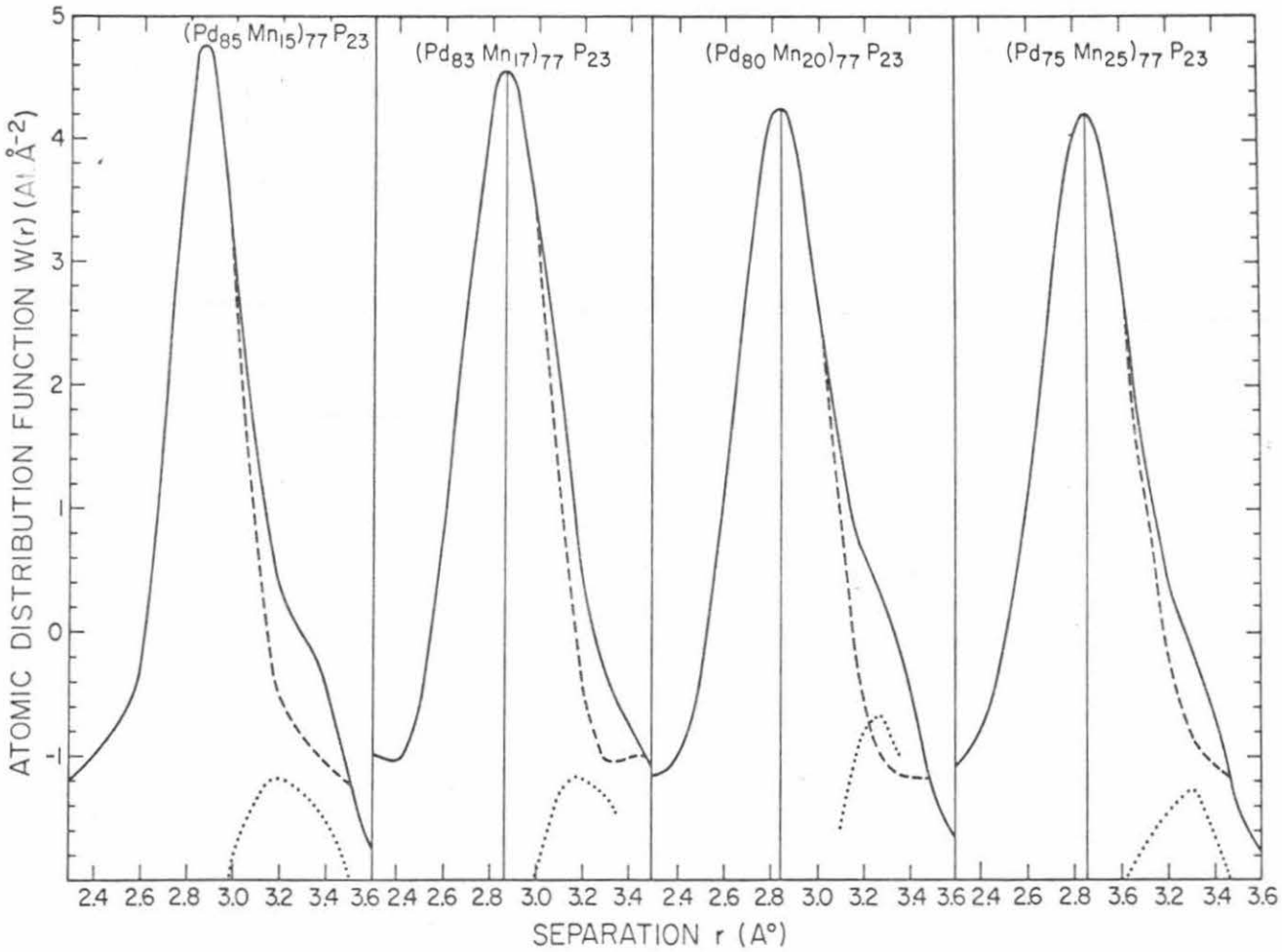

Fig. 17. First peak of the atomic distribution function (solid line), symmetrical left side (dashed line), subtraction of the two curves (dotted line)

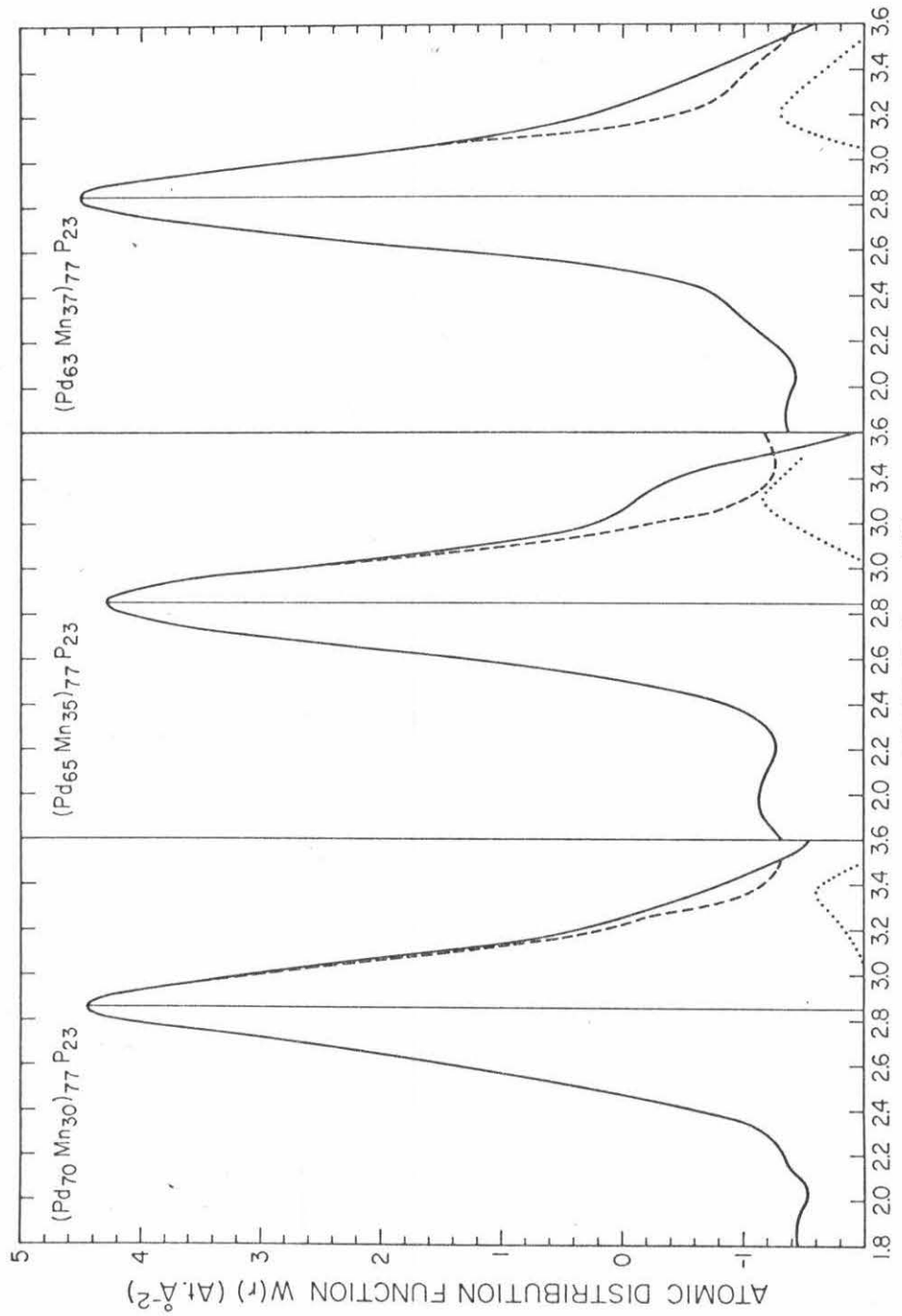

Fig. 18. Same as Fig. 11

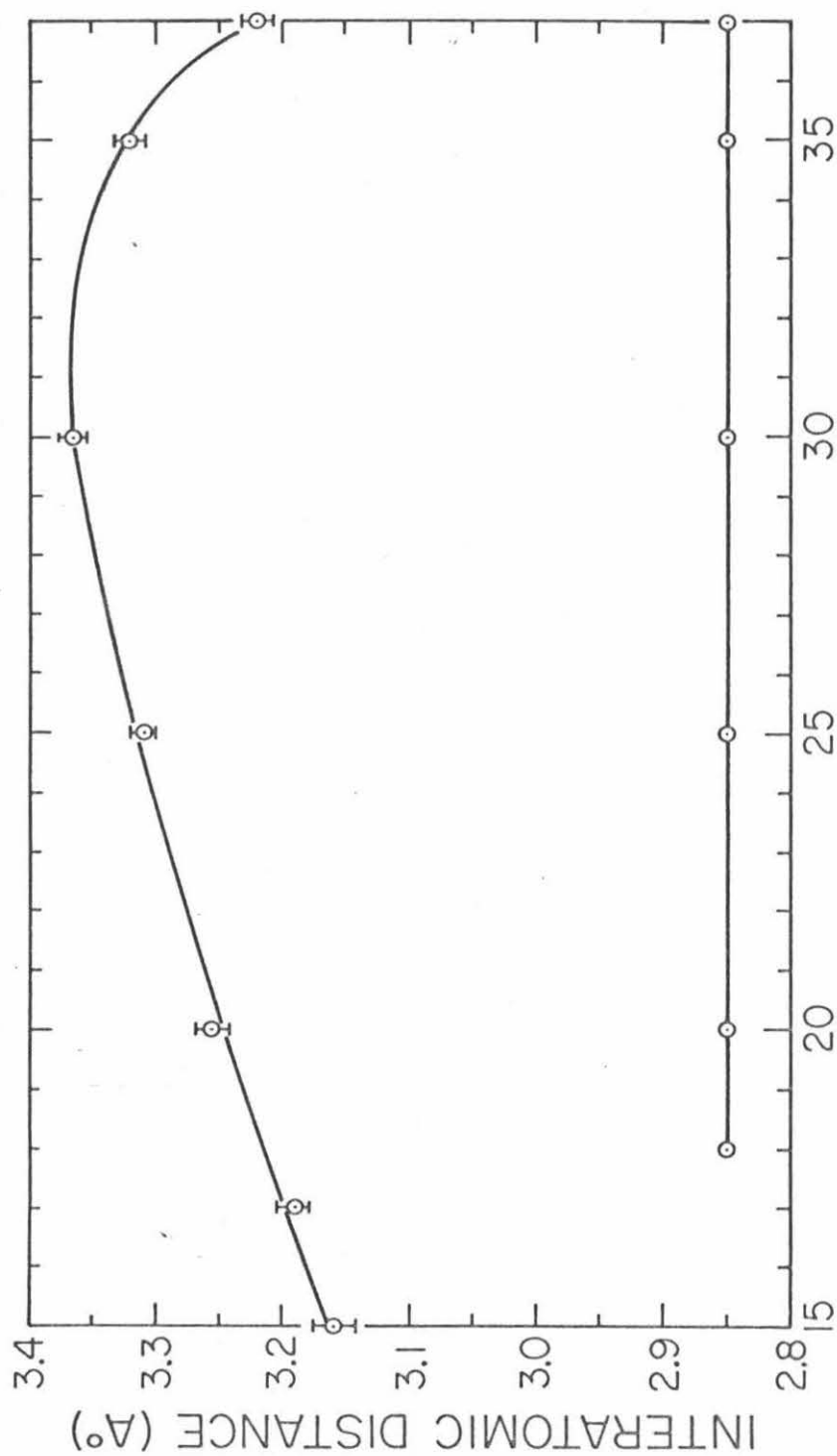

Fig. 19. Metal-to-metal (⊖) and maximum position of the shoulder of the right hand side of the first peak (⊖) versus manganese concentration.

function (RDF) for $(Pd_{85}Mn_{15})_{77}P_{23}$ is shown as an example in Fig. 15 by the oscillating curve. The smoothly rising curve represents the average atomic density $4\pi r^2\rho_o$. The area under the first peak Fig. 16 of the reduced radial distribution function $g(r) = \rho(r)/\rho_o(r)$ gives the coordination number and the results are shown in Tables VIII and IX. The results of the structure investigation with MoK_α radiation are summarized in Table XI and show rather constant ratios of r_i/r_1 and K_i/K_1 implying a continuity in structural order. The product $K_1 \cdot r_1$ varies slowly between 7.78 and 7.93 as we increase the manganese content and appears to fulfill the relationship $K_1 \cdot r_1 \simeq 8.0$ found in most other amorphous alloys. As shown in Figs. 13 and 14, the first peaks I(K) and W(r) are not symmetrical. To analyze this asymmetry, a symmetrical curve was traced taking the mirror image of the left side with respect to the location of the maximum, dashed line Figs. 17 and 18, and the difference between this curve and the experimental one is represented by the dotted lines. The metal-to-metal nearest neighbor distances and the maximum in the shoulder on the right hand side of the first peak is shown in Fig. 19 as a function of manganese concentration. Finally the correlation function C(r) was shown in Fig. 9.

b. Phosphorus concentration effect

Four different alloys varying in composition between $18 \leq y \leq 25$ in $(Pd_{70}Mn_{30})_{100-y}P_y$ were investigated with MoK_α and CuK_α radiations. The diffraction pattern showed several amorphous bands and the position of these peaks was also displaced toward larger values of 2θ or K with increasing percentage of phosphorous.

Table XII gathers the numerical results with respect to the diffraction patterns and to the maxima of the interference function $I(K)$. The ratio of r_2/r_1 is 1.77 and close to 1.8 found for liquids. The interference function is shown in Fig. 20. The Fourier transforms leading to the atomic distribution functions were performed in the same way as in the manganese concentration effect. The resultant atomic distribution function $W(r)$ is represented by Fig. 21 while the radial distribution function $r\,W(r)$ is shown in Fig. 22. In both cases a temperature factor equal to $\exp(-0.002\,k^2)$ was used in an effort to reduce the oversharpening effect of $1/f_e^2$ and at the same time take into consideration the thermal vibration. Similarly the crystallite size is listed in Table VI and the density obtained $W(r)$ is compared with the experimental density, Table V. By integrating under the curve of the reduced radial distribution function, the first coordination number is obtained, while the second and third coordination numbers are computed for $(Pd_{70}Mn_{30})_{75}P_{25}$ just for the valuation of an approximate order of magnitude. From the asymmetry of the first peak in $W(r)$ the metal-to-metal and the maximum position of the shoulder on the right hand side of the first peak is shown in Fig. 24 using the same technique mentioned for the increase in manganese effect. The results of the interatomic distance versus the phosphorous concentration is shown in Fig. 26. As in $(Pd_{100-x}Mn_x)_{77}P_{23}$ the relevant structure parameters are shown in Table XIII; the product $K_1 \cdot r_1$ increases from 7.88 for 18 At.% P to 7.93 for 25 At.% P and is close to the expected value of 8.0.

Table XII. Structural Results for Amorphous $(Pd_{70}Mn_{30})_{100-y}P_y$

		Max. position in I(K)				Max. position in W(r)				
		K_1	K_2	K_3	K_4	r_1	r_2	r_3	r_4	r_2/r_1
$(Pd_{70}Mn_{30})_{82}P_{18}$	Position	2.76	4.78	7.11	9.63	2.84	5.00	7.20	9.60	1.754
	Intensity	5.83	1.85	1.00	0.55	4.64	1.04	0.78	0.42	
$(Pd_{70}Mn_{30})_{80}P_{20}$	Position	2.77	4.75	7.11	9.58	2.85	5.05	7.20	9.6	1.772
	Intensity	5.70	2.01	0.98	0.62	4.82	1.00	0.75	0.41	
$(Pd_{70}Mn_{30})_{77}P_{23}$	Position	2.77	4.78	7.02	9.42	2.85	5.05	7.25	9.65	1.772
	Intensity	5.62	1.93	0.97	0.69	4.47	0.89	0.68	0.40	
$(Pd_{70}Mn_{30})_{75}P_{25}$	Position	2.78	4.75	7.05	9.38	2.85	5.05	7.25	9.65	1.772
	Intensity	5.11	8.89	1.42	0.83	4.96	0.87	0.64	0.32	

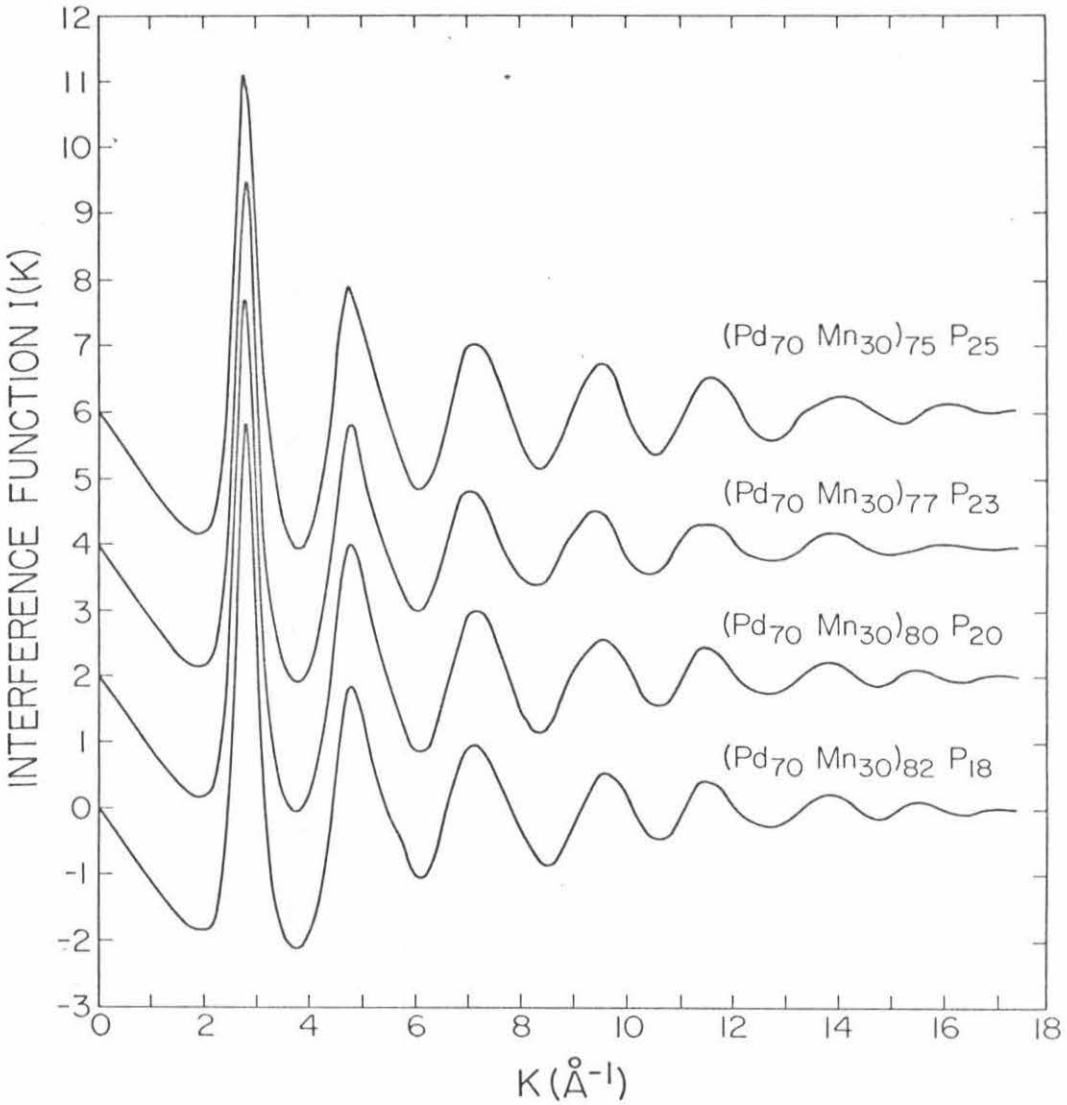

Fig. 20. Interference function for $(Pd_{70}Mn_{30})_{100-y}P_y$ alloys with various phosphorus concentrations

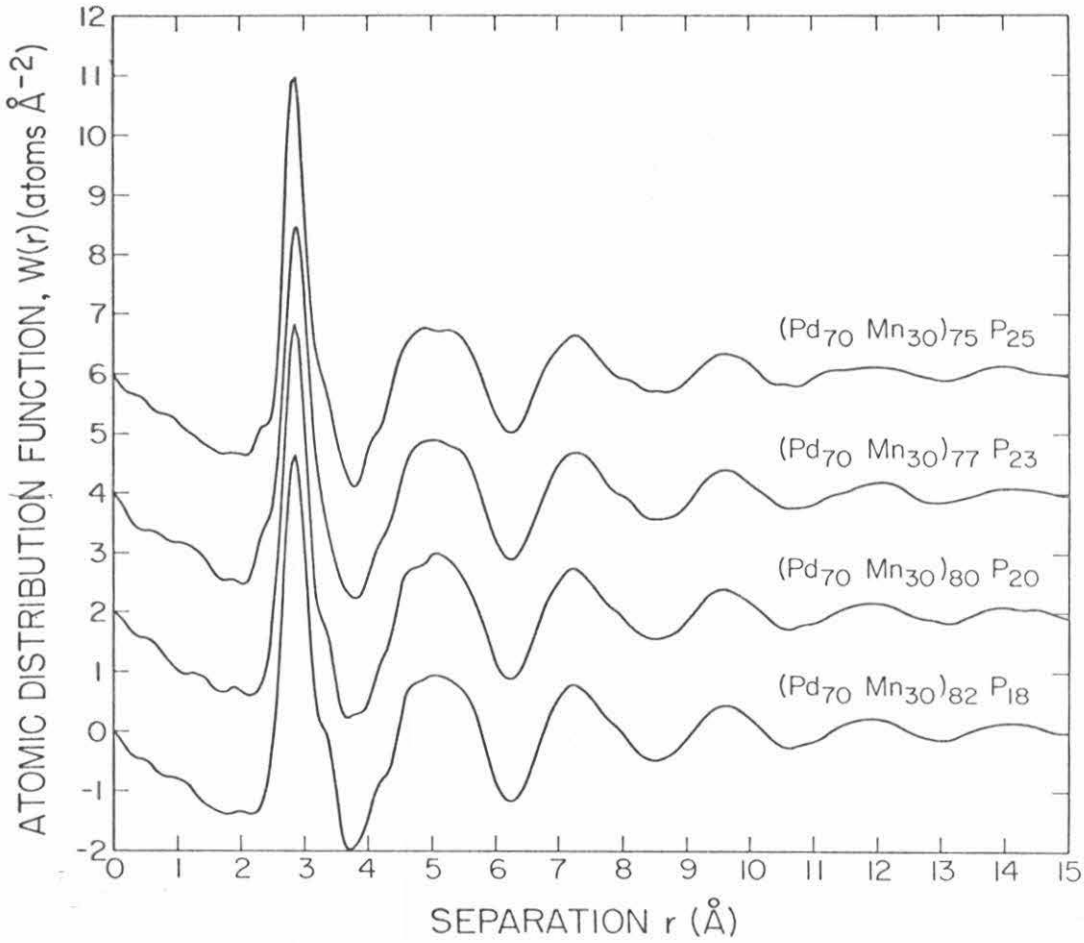

Fig. 21. Atomic distribution function for $(Pd_{70}Mn_{30})_{100-y}P_y$ alloys with varied concentration of phosphorus

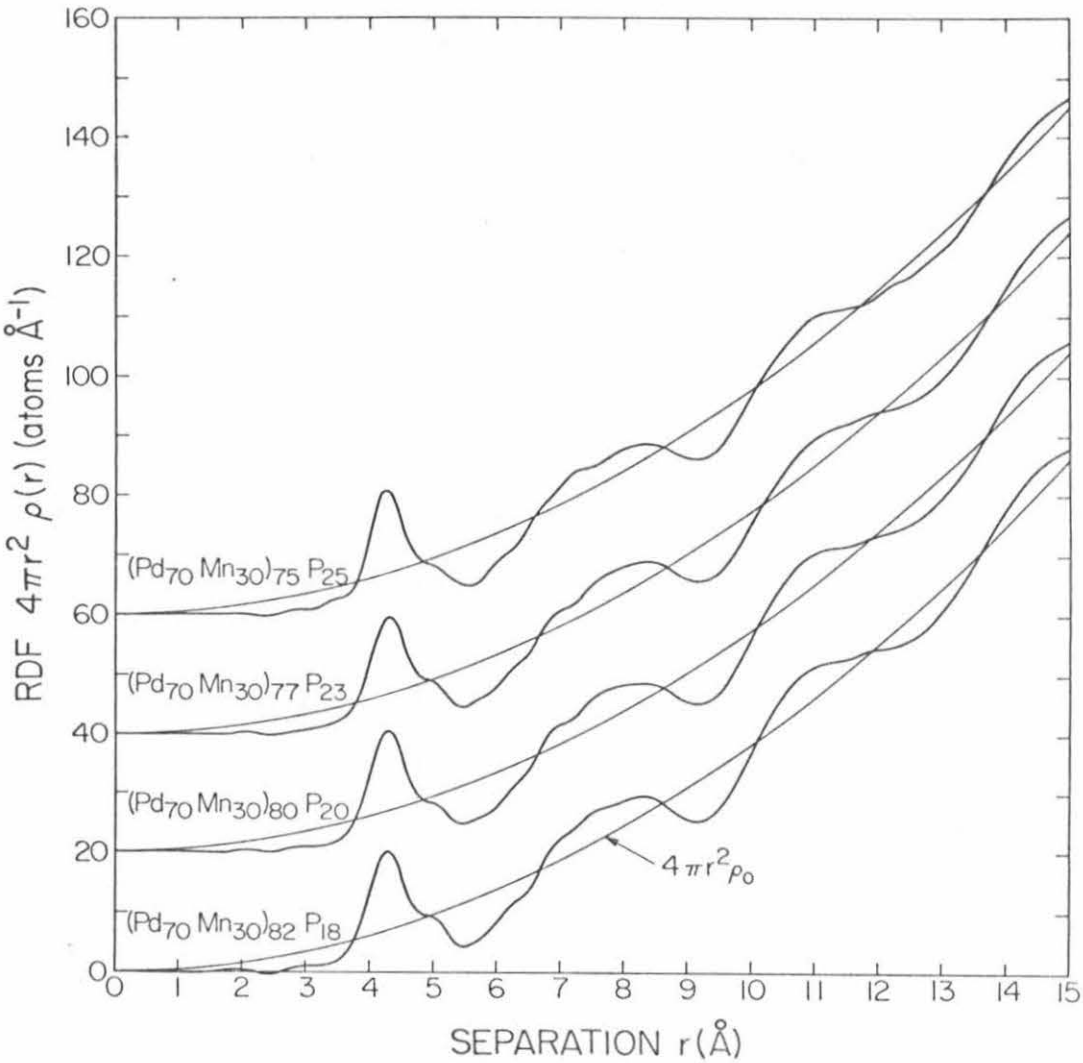

Fig. 22. Atomic radial distribution function (RDF) for amorphous $(Pd_{70}Mn_{30})_{100-y}P_y$ alloys (oscillating curve). The smoothly rising curve represents the average atomic density $4\pi r^2\rho_o$. The zeros have been systematically shifted for alloys having y greater than 20.

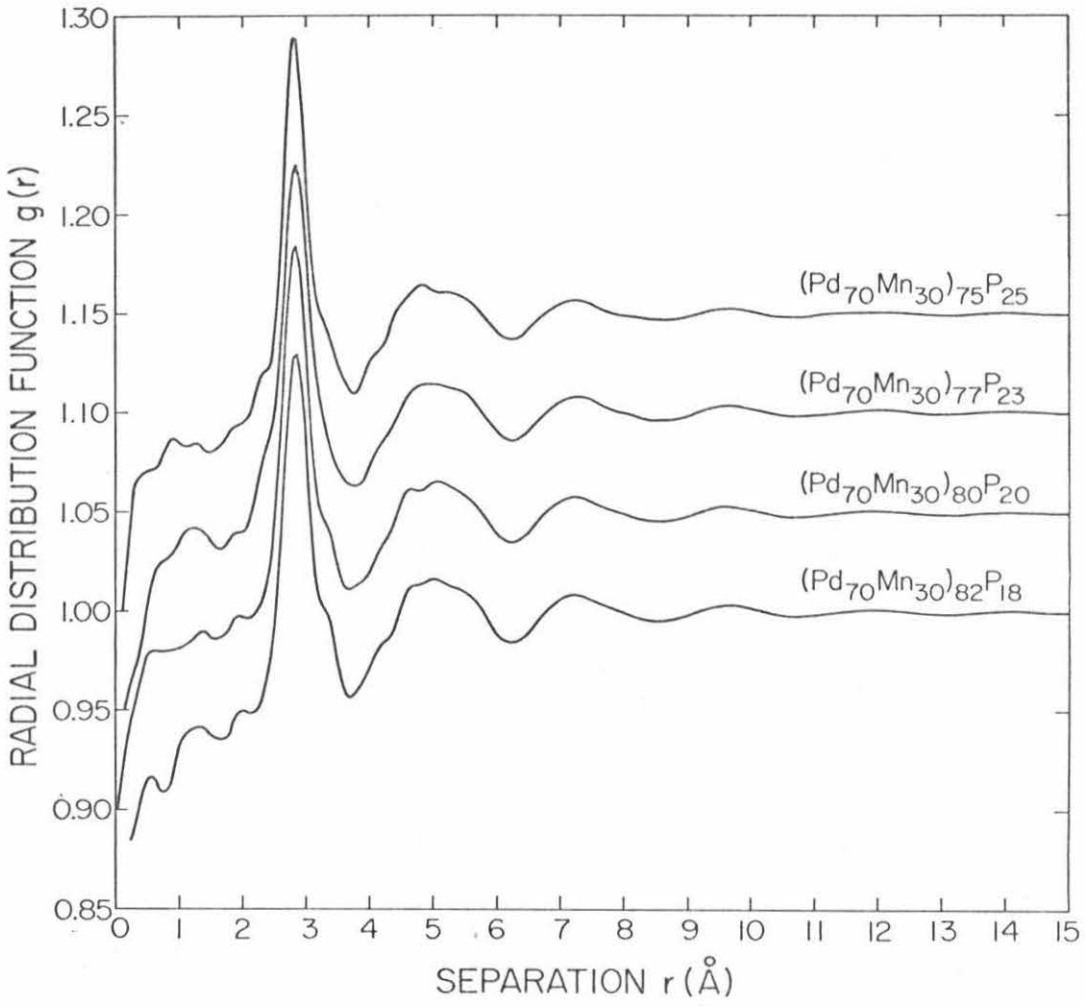

Fig. 23. Radial distribution function for amorphous $(Pd_{70}Mn_{30})_{100-y}P_y$ where 1 represents perfect disorder. Respective curves were systematically shifted by 0.05.

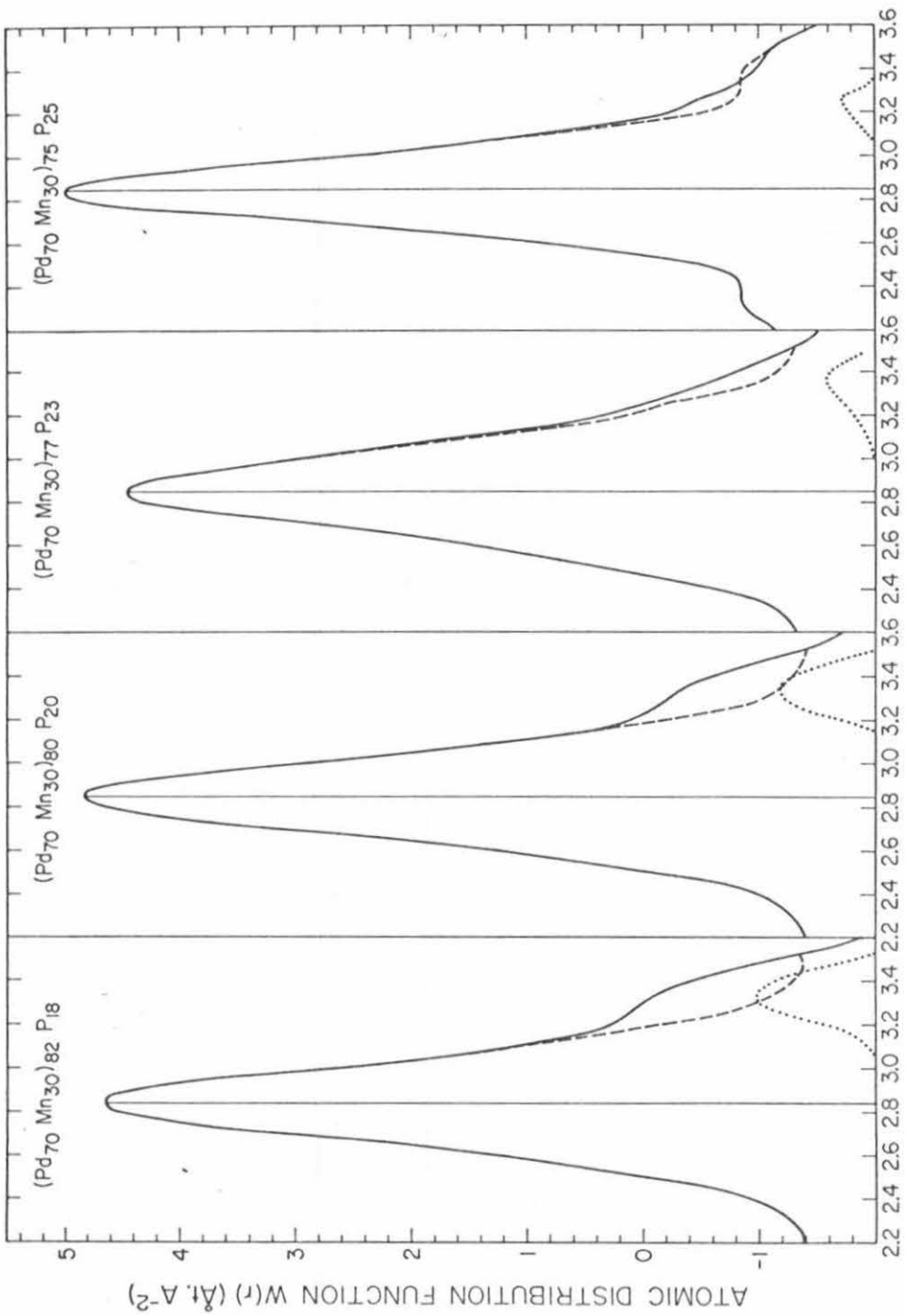

Fig. 24. First peak of the atomic distribution function (solid line), symmetrical left side (dashed line), subtraction of the two curves (dotted line)

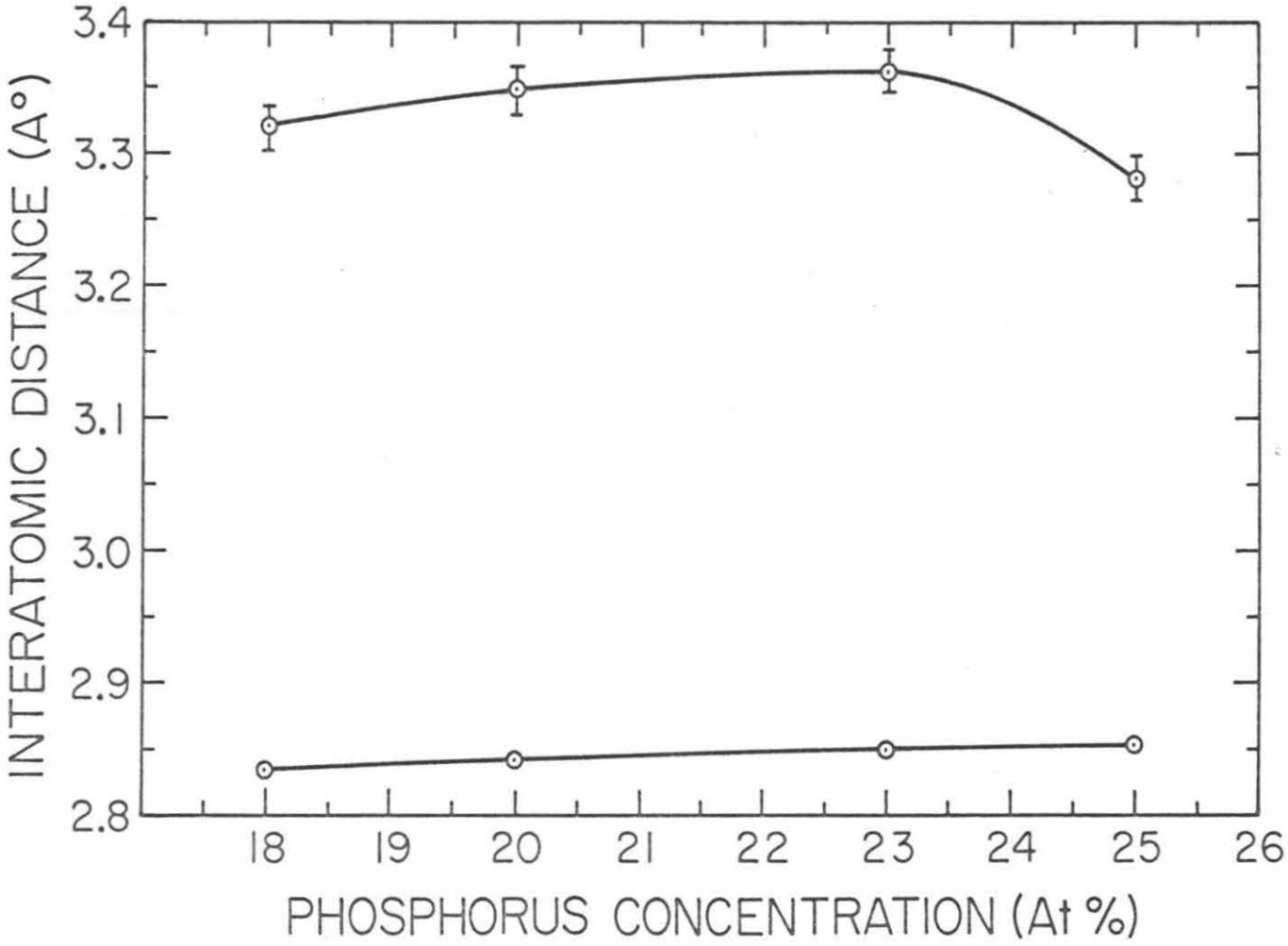

Fig. 25. Metal-to-metal (θ) and maximum position of the shoulder of the right hand side of the first peak ($\bar{\theta}$) versus phosphorus concentration.

Table XIII. Relative Positions of Maxima in I(K) and W(r)

	K_i/K_1			r_i/r_1			$K_1 \cdot r_1$
Alloy composition	i=1	i=2	i=3	i=1	i=2	i=3	
$(Pd_{70}Mn_{30})_{82}P_{18}$	1.00	1.72	2.57	1.00	1.76	2.53	7.88
$(Pd_{70}Mn_{30})_{80}P_{20}$	1.00	1.71	2.56	1.00	1.77	2.53	7.90
$(Pd_{70}Mn_{30})_{77}P_{23}$	1.00	1.72	2.53	1.00	1.77	2.54	7.90
$(Pd_{70}Mn_{30})_{75}P_{25}$	1.00	1.71	2.54	1.00	1.76	2.53	7.93

2. Palladium-Cobalt-Phosphorous Alloy System

X-ray diffraction measurements using CuK_α radiation was made on eight amorphous alloys having the composition $(Pd_{100-x}Co_x)_{80}P_{20}$ where $15 \leq x \leq 50$ which was obtained by rapid quenching from the liquid state. Unfortunately, we could not study the distribution function with MoK_α because of the high fluorescence expected and consequently low peak to background ratio. From the careful scanning by CuK_α radiation of the first amorphous peak we extracted the grain size parameter, Table VII, as well as the convincing evidence of the nonpresence of any microcrystals which would have shown as peaks superimposed on the amorphous band.

IV. ELECTRICAL RESISTIVITY

The amorphous alloys which were the object of this investigation exhibit characteristic metallic transport properties. The study of electrical resistivity and specifically its variation with temperature and composition is of particular interest. The existence of localized moment, due to the presence of a transition metal element, suggested low temperature experiments in order to investigate the existence and the type of effect the Kondo phenomenon does have in these alloys. High temperature resistivity measurements yielded information on the transport mechanism and the transformation from the amorphous to the crystalline state.

The Pd-Mn-P alloys constitute a suitable amorphous system for studying the influence of composition on the electrical resistivity, since the ternary alloys could be obtained in an amorphous structure over a relatively large range of metal and metalloid compositions. More specifically amorphous alloys could be obtained from 15 to 38 at.% manganese to a constant phosphorus concentration of 23 at.% and keeping the metallic contents at $(Pd_{70}Mn_{30})_{100-y}P_y$ the concentration of phosphorus could vary from 17 to 26 at.%. The incentive for the present work is to study the effect of the 3d band filling of the first transition metal group, the phosphorus concentration effect which acts as an electron donor, and the transition metal concentration effect on the transport properties. The presence of a magnetic element makes the alloy quite sensitive to spin interaction, which, depending on the concentration and valency of the "d" shell of the

transition metal, the phosphorus content and the temperature, determine the magnitude of the localized moment.

A. Experimental Procedure

Rectangular samples of about 18 mm × 5 mm were cut from the 40 to 60μ thick foil. Current and potential leads of 0.005 inch diameter platinum wire were spot welded on the specimens with the potential leads 12 mm apart approximately. Measurements were made with a constant current of 100 mA measured as the potential drop across a standard 0.1μ resistor. The voltage range was between 10 and 20 mv. The current and potentials were measured using a potentiometer with maximum sensitivity of 10^{-5}mv. The dimensions of the samples were determined by use of a micrometer. Variation of the thickness within the sample was about ±5% and the precision was ±2% for the other dimensions. Although the relative error is very good, the error on the absolute value of the resistivity is ±10%.

Temperatures were measured with a calibrated Ge crystal from 4.2°K to 78°K and with a copper-constantan thermocouple from 77 to 300°K. The sensors were placed close to the samples located inside the brass resistivity probe. For the high temperature range, 300°K to 1000°K, a spot welded platinum rhodium thermocouple was used. The temperature accuracy was 0.1°K.

Comparison between the resistivity data using point contact technique and spot welding technique was made in the range 3.5 to 100°K and no variation in the shape of the resistivity minimum was observed for all the alloys measured.

B. Brief Review of Relevant Theories

1. Localized Electronic States in Disordered Alloys

Quantum mechanical motion could exist in certain physical phenomena

without any particular thermal activation among sites at which the mobile entities--either electrons or spins--may be localized. In such situations it is believed that transport occurs not by motion of the free carriers or the spins, which are scattered randomly through the medium, but in some sense by a series of quantum mechanical jumps from one site to another. Another interesting feature of this model is the randomness of interactions of any entity with its nearest neighbors in a random arrangement of electronic or magnetic spin. The suggestion that, for an electron in a disordered one-dimensional lattice, all characteristic solutions of the Schrödinger equation are localized was first made by Mott and Twose[49] who gave a proof for a particular model of a disordered Kronig-Penny lattice. This was extended by Borland[50] and Borland and Bird[51] to the case of a random distribution of delta functions. It might be worthwhile to define here what is meant by the localized state of an electron. The definition is that if the Schrödinger equation for an electron in the field of a disordered potential V is

$$\frac{d^2\psi}{dx^2} + \frac{2m}{h^2}(E - V)\psi = 0$$

Then all bounded solutions in the range $-\infty < x < \infty$ have a maximum value for some value x_n and decay exponentially to zero as $\exp\{-\gamma|x - x_n|\}$ as $|x_n - x|$ tends to infinity, each solution ψ_n has a characteristic energy E_n. It may happen that a localized state may have two or more peaks of comparable height at a distance, say X, from each other. If so, we should expect two states, in one of which ψ would have the same sign in both peaks, in the other, opposite signs; the energy separation between them would be of order $E \exp(-\gamma X)$. As

X increases, the proportion of configurations in which this happens will decrease exponentially. Within a given range of energies, states are either localized or non-localized. This is a quantitative difference; if states are localized an electron placed in a given region will not diffuse away. There will thus exist critical energies E_c dividing ranges in which states are localized from those which are not. For localized states ψ falls off as $\sin kr \exp(-\gamma r)$ and γ tends to zero as $E \to E_c$. For non-localized states the mean free path L leads roughly to the electron wavelength λ as $E \to E_c$.

The only quantitative work on the condition for localized states is that of Anderson[52]. Anderson considers essentially the tight binding model, in which a single band of energy levels is formed from s-like atomic orbitals with bandwidth 2JZ where Z is the coordination number and J an overlap energy integral. Instead of considering a random variation of J due to an amorphous structure, Anderson imposes on each site a potential energy V, which has a random spread of value $\langle V \rangle$. He finds that if $\langle V \rangle / J$ is large enough, all eigenstates are localized; for smaller values some are not. His results are expressed in terms of the connectivity of the lattice, but it appears that states become localized when $\langle V \rangle$ is greater than about six times the bandwidth. With this model there is no boundary E_c between localized and non-localized states.

In considering the conduction band, Frohlich[53], Gubanov[54] and Banyai[55] suggested that in amorphous materials localized states may exist in a tail below the conduction band, and that in ionized materials a polarization round the trap will always increase the depth

of the localized state. The interesting problem then arises as to what conditions the states in the minimum of density of state $N(E)$ versus E curve will be localized. Naturally the answer is difficult to predict but will depend on the distance and strength of interaction between atoms. Large deviations will always be associated with short mean-free path as in amorphous alloys, unlike the crystalline case, the same field is responsible for deviations and for the mean free path. In general, a perturbation strong enough to lower $N(E)$ by 50% will produce a mean free path of the order of the interatomic distances. Mott does not expect that mean free paths shorter than this could occur. Thus it seems that localized states do occur when the factor g defined by $g = N(E)/N(E)_{\text{free electron}}$ falls below 0.5.

The density of state in amorphous material as found by Faber[56] is close to the free electron theory

$$N(E) = \frac{4\pi k^2}{8\pi^3} \frac{dk}{dE}$$

2. The Kondo Effect

Sarachik, Corenzwit and Longinotti[57] have shown that the appearance of a minimum in the resistivity versus temperature curve is directly related to the existence of a magnetic moment and a temperature dependent susceptibility. Kondo[17], in his treatment, accepts the existence of a well localized moment and interprets the resistivity minimum phenomena by the interaction between the spin $\vec{s}$ of the conduction electrons and the localized magnetic moment $\vec{S}$

independent of the structure or degree of order of the system. A general expression for a Kondo type resistivity is

$$\rho = \rho_L + x\rho_p + x\rho_i + 3(3n\, J_{sd}\, \rho_i/E_F)\, \ell n\, T \qquad (27)$$

where ρ_L is the lattice resistivity, ρ_p is the resistivity due to the potential introduced by the transition metal, x is the concentration of the transition metal, ρ_i is the temperature independent part of the spin resistivity, n is the number of conduction electrons per host atom, and E_F is the Fermi energy. If the s-d exchange interactions $J_{sd} < 0$ this corresponds to an antiferromagnetic coupling between the conduction "s" electron and the localized "d" electrons and equation (27) gives a minimum at a temperature T_m. The fact that the temperature dependent term for the amorphous varies as T^2 instead of T^5 which is found in crystalline alloy will give a T_m at

$$T_m = (3n\, J_{sd}\, \rho_i/2E_F\, a)^{1/2}\, x^{1/2} \qquad (28)$$

The Kondo treatment drawback of resistivity diverging as T goes to zero, was solved by Nagaoka[18]. Nagaoka has shown that if $J_{sd} < 0$ the perturbation treatment of Kondo breaks down below a critical temperature T_K and that near the Fermi surface there appears a quasi-bound state between the conduction electron spins and the localized d spins. This bound state is the consequence of a collective effect, where the moment of the conduction electrons in the vicinity of the transition metal atom compensates the moment of the localized spins rather than that of a singlet spin state in which a single electron is bound to the magnetic atom. Therefore the resistivity saturates for $T \ll T_K$.

It was thought for some time that T_K exists only at low temperatures but it was pointed out by Schrieffer[58] that T_K could vary between the order of millidegrees to beyond the melting point as it depends on the density of states $N(E)$ and the Fermi temperature by the following relation:

$$T_K \simeq T_F \exp(-1/N(E)\ |J_{sd}|)$$

3. Possible Origins of a Negative Temperature Coefficient of Resistivity

(a) In 1958 Chandrasekhar and Huhn[59] using an expression suggested by Jones[60] explained the negative temperature coefficient of resistivity of a number of γ phase uranium-molybdenum alloys by a two-overlapping-bands model of which one is narrow. Such a band structure was shown to be reasonable for α and γ phase uranium by Friedel[61]. Blatt[62] used the model suggested by Ziman[63] to predict the observed temperature dependence of the Hall coefficient of the above mentioned alloys using a conductivity equation given by

$$\sigma = \sigma(n) + \frac{\pi^2}{6}(kT)^2 \left(\frac{\partial^2 \sigma(\varepsilon)}{\partial \varepsilon^2}\right)_{\varepsilon = \eta} \tag{29}$$

where

$$\sigma(\varepsilon) = \frac{e^2}{12\pi^2\hbar^3}\left[\tau(\varepsilon) \langle v_c(\varepsilon)\rangle^2 N_c(\varepsilon)\right]$$

$N_c(\varepsilon)$ is the density of state in the conduction band, $\langle v_c(\varepsilon)\rangle = (1/h)\nabla_k \varepsilon$ is the expectation value of the velocity of an electron of energy ε in the conduction band and $\tau(\varepsilon)$ is the relation time. If

the density of final states from the scattering processes which limits the conductivity is denoted by $N_f(\varepsilon)$ the following expression could be written

$$[\tau(\varepsilon)]^{-1} = Q\, N_f(\varepsilon)$$

where Q could represent number of defects, impurities, localized states, or any scattering mechanism. Therefore departure from the normal temperature dependence of resistivity may arise from:

(1) A temperature dependent scattering mechanism leading to an anomalous variation of Q with T, which includes significant departures of the phonon spectrum from Debye model as a result of high scattering centers.

(2) A sufficiently rapid variation of $N_f(\varepsilon)$ with ε to make the second term on the right hand side of equation (29) of significant magnitude. This mechanism which is due to Jones[60] assumes that the band structure of the metal is such that two bands overlap near the Fermi energy: one band which is broad, the conduction band (s electrons) and the other a narrow band (d electrons). Blatt assumes, as did Jones, that the only function which exhibits rapid energy dependence near the Fermi energy is $N_f(\varepsilon)$, the density of state in the narrow "d-band", and that the effectiveness in this narrow band is so large that the current is carried almost exclusively by the electrons (or holes) in the broad conduction band; under these assumptions the resistivity[60] is given by

$$\rho(T) = \rho(\eta_0, T)\left[1 - \frac{\pi}{6}(kT)^2 \left\{3\left(\frac{N_f'}{N_f}\right)^2 - \left(\frac{N_f''}{N_f}\right)\right\}\right] \qquad (30)$$

where each prime (') denotes differentiation with respect to ε , and all quantities in brackets are evaluated at η_o , the Fermi energy at $T = 0^oK$. Equation (30) was obtained from the results for the transport coefficients[64] and the usual expansion of the relevant integrals in the degenerate limit[65].

If it is further assumed that the d-band is of standard form, (30) reduces to

$$\rho(T) = \rho(\eta_o,T)[1 - \frac{\pi^2}{6} (\frac{kT}{\Delta E})^2] \qquad (31)$$

Here E is the energy difference between the Fermi energy at $T = 0^oK$ and the edge of the "d" band, and $\rho(T)$ is proportional to T^2 .

(3) A dependence of the band structure on temperature leading to anomalous variations of $N_f(\varepsilon)$, $N_c(\varepsilon)$ and/or $v_c(\varepsilon)$ with temperature (semiconductors).

(4) Another approach was pointed out by Ziman[63] where the conductivity can be accounted for by the assumption that the scattering of an electron by each atom is small and that it can therefore be calculated from the atomic pseudopotential by using the Born approximation for the scattering and the experimentally determined pair distribution functions for the relative position of the atoms. This was done by Bhatia and Krishnan[66]. Sinha[67] concluded that the negative slope of the resistivity versus temperature curves for amorphous $(Pt_{100-x}Ni_x)_{75}P_{25}$ with $20 \leq x \leq 50$ was due to a high Fermi energy of about 6.9 eV and that this corresponded to the position of the first peak in the x-ray interference function $I(K)$ at which $I(K)$

decreased with increasing temperature.

(5) Theorists and experimentalists agree fairly well on how the measured quantities as a function of temperature[68] do behave in an alloy containing paramagnetic spins. Nagaoka[18] attributed the low temperature T^2 behavior to condensation or spin compensated states. Others[63,52] attributed the T^2 behavior to other variations of s-d interaction. Kaiser and Doniach[69] attributed the T^2 behavior in CuAl and MnAl to localized spin fluctuations LSF. A localized spin fluctuation is the repeated scattering between an electron and a hole of opposite spin on the impurity site. It has a lifetime τ_o which is given by

$$\tau_o = \pi \rho_d(\varepsilon) [1 - U \rho_d(\varepsilon)]^{-1} \tag{32}$$

where U is the Coulomb repulsion between localized "d" electrons in the Anderson model[52] and $\rho_d(\varepsilon)$ is the density of the Fermi level of a "d" electron state of position E_d and width Δ

$$\rho_d(\varepsilon) = \Delta[\pi(E_d^2 + \Delta^2)]^{-1} \tag{33}$$

In the Hartree-Fock sense, the alloy is non-magnetic $(U\rho_d(0) < 1)$ and will exhibit at low temperatures $(kT << \tau_o^{-1})$ nonmagnetic transport properties and susceptibility, with some weak additional contribution of the spin fluctuations (correlation effects). This is the spin-compensated state. However, as soon as the temperature reaches the degeneracy temperature which is τ_o^{-1} rather than Δ as in the case of a virtual bound state, the spin fluctuations behave classically as would a well-defined spin (Curie paramagnetism). In other

words, when the temperature becomes of the order τ_o^{-1} the spin fluctuations are slower than the thermal fluctuations of the temporary moment that they describe. At this temperature and above, there is no physical difference between a spin fluctuation and a genuine spin; the system behaves as if it were magnetic (resistance minimum, Curie law for the susceptibility, etc.). The transition is smooth, as it should be in a system involving a limited number of degrees of freedom, and occurs at what may be called Kondo-like transition temperature T_K [52]. Rivier and Zukermann[70] showed that the Kondo temperature obtained from the spin fluctuations theory given by

$$kT_{LSF} = \tau_o^{-1} \tag{34}$$

agrees with the experimental and theoretical values deduced from the resistivity in the spin compensated state and from the susceptibility, both at high temperatures and at $T = 0$. They showed that T_{LSF} indicates only a change of regime; analytically it is not the well-defined temperature of Abrikosov[71] or of Suhl[19].

The Kondo temperature according to Abrikosov

$$kT_{K_a} = D \exp(-1/\rho(\varepsilon)\, J) \tag{35}$$

usually quoted as T_{K_a}, is associated with the maximum in the high temperature expression for the resistivity. For the localized spin fluctuations, one finds that $kT_{K_a} \ll \tau_o^{-1}$ lies outside the validity range of the high-temperature resistivity formula. The true resistance maximum does not occur at the Kondo temperature, as appears in the results of Suhl and Wong[19]. Moreover, while equation (35) is

independent of the ordinary (spin-nonflip) potential, T_{K_a} is modified by potential scattering in the curves of the latter authors. It is also the case of T_{LSF} where $\rho_d(\varepsilon)$ via E_d is affected by the potential.

C. Experimental Results

1. Low Temperature Measurements

a. Palladium-cobalt-phosphorus

The amorphous Pd-Co-P alloys investigated show metallic conduction. At room temperature their electrical resistivity is three times the resistivity of the stable crystalline phases obtained by annealing at 600°C for 15 days. The values obtained for the amorphous alloys at room temperature range from 143 to 298 μΩ-cm. The dispersion of the values is, however, too large to show clearly the influence of composition. These variations are attributed to the variations in the local atomic order in the amorphous structure which results from unavoidable variations in the actual rate of quenching from point to point in a given specimen. As seen from Table XIV, these variations can be as high as 60 μΩ-cm for two different specimens from different foils. As shown by Boucher[72] even within the same foil variations do exist. The order of magnitude of the resistivity values is the same as that previously reported for amorphous Pd-Ni-P and Pd-Fe-P and no trend is easily detectable in terms of the kind of transition metal in the alloy.

Like Pd-Ni-P and Pd-Fe-P, the Pd-Co-P alloys show a small but well defined resistivity minimum. This minimum appears at temperatures

ranging from 23 to 56°K depending on alloy composition. Moreover, it was found that, for temperatures between the minimum temperature T_{min} and about 80-118°K the resistivity assumed a T^2 behavior. Above the T^2 range, a good linear relationship with temperature appears to be dominant which tends to incline parallel toward the x axis. The slope of this region which for comparison was computed between 200 and 300°K was found to increase with decrease in metallic content, at a fixed concentration of glass former of 20 at.% P. The low temperature resistivity curves are shown in Fig. 26.

The existence of a resistivity minimum, and the presence of Co led to consideration of a possible Kondo effect[17]. Therefore, the resistivity $\rho(T)$ at low temperature was tentatively approximated by a function of the form:

$$\rho(T) = \rho_o + \beta T^2 - \alpha \ln T - \Delta\rho_o \qquad (36)$$

The determination of these parameters was performed by plotting $\rho(T)$ versus T^2 to obtain ρ_o and β and then by plotting the difference $\rho(T) - \rho_o - \beta T^2 = R_{spin}(T)$ versus $\ln T$. Equation (36) gives a resistivity minimum at temperature

$$T_{min} = (-\alpha/2\beta)^{1/2} \qquad (37)$$

which we call $(T_{min})_{calculated}$, the α and β parameters were detained from Figs. 27 and 28, and all the resistivity parameters are listed in Table XV, together with $(T_{min})_{experimental}$. Table XIV gives interesting resistivity parameters, namely ρ_{max} (resistivity at 4.2°K)

Table XIV. Coefficients of Electrical Resistivity

Composition	Sample #	$\rho_{max}(4.2^{o}K)$ $10^{-4}\Omega$ cm	ρ_{min} $10^{-5}\Omega$ cm	$\frac{\rho_{max}-\rho_{min}}{\rho_{min}}$ 10^{-2}	$\frac{\rho_{300}-\rho_{200}}{\Delta T}$ 10^{-4} cm/^{o}K
$(Pd_{50}Co_{50})_{80}P_{20}$	1	1.3838	1.3815	1.66	15.38
	2	1.6346	1.6321		18.30
$(Pd_{55}Co_{45})_{80}P_{20}$	1	2.334	2.3278	2.66	17.14
	2	2.9253	2.9180	2.50	21.43
$(Pd_{60}Co_{40})_{80}P_{20}$		2.4655	2.4574	3.29	14.50
$(Pd_{65}Co_{35})_{80}P_{20}$	2	1.7983	1.7907	4.24	13.30
	1	1.8103	1.8024	4.38	9.10
$(Pd_{70}Co_{30})_{80}P_{20}$	2	1.8693	1.8596	5.21	8.70
	1	1.5721	1.5632	5.69	6.40
$(Pd_{75}Co_{25})_{80}P_{20}$		1.7834	1.7731	5.80	10.00
$(Pd_{80}Co_{20})_{80}P_{20}$	1	1.8194	1.8074	6.63	5.1
	2	1.7938	1.7822	6.50	8.7
$(Pd_{85}Co_{15})_{80}P_{20}$	1	1.8345	1.8223	6.69	8.7
	2	1.5927	1.5804	7.78	6.0

Table XV. Electrical Resistivity Parameters

Composition	Sample #	$\beta(10^{-11})$	$\rho_o(10^{-4})$	$\alpha(10^{-7})$	T_{min}obs.	Maximum T^2 of range	T_{min}cal.
$(Pd_{50}Co_{50})_{80}P_{20}$	1	0.1416	1.3807	-1.98	23.23 ± 3.0	77.46	26.4
	2				22.30 ± 2.1		
$(Pd_{55}Co_{45})_{80}P_{20}$	1	0.2016	2.9161	-5.25	25.50 ± 1.1	79.46	36.08
	2				24.85 ± 3.2		
$(Pd_{60}Co_{40})_{80}P_{20}$		0.1751	2.4451	-6.50	29.50 ± 1.6	85.30	43.08
$(Pd_{65}Co_{35})_{80}P_{20}$	1	4.760	1.8014	-4.17	41.70 ± 1.9	114.02	66.18
	2				37.90 ± 2.1		
$(Pd_{70}Co_{30})_{80}P_{20}$	1	5.260	1.8582	-4.83	50.46 ± 4.3	118.02	67.76
	2				56.40 ± 1.2		
$(Pd_{75}Co_{25})_{80}P_{20}$		6.425	1.1719	-6.75	40.11 ± 2.08	109.04	72.48
$(Pd_{80}Co_{20})_{80}P_{20}$	1				44.18 ± 2.8		
	2	5.625	1.7812	-7.25	42.08 ± 4.0	100.16	80.28
$(Pd_{85}Co_{15})_{80}P_{20}$	1	6.950	1.8210	-6.6	38.06 ± 4.4	94.87	68.78
	2				40.37 ± 5.8		

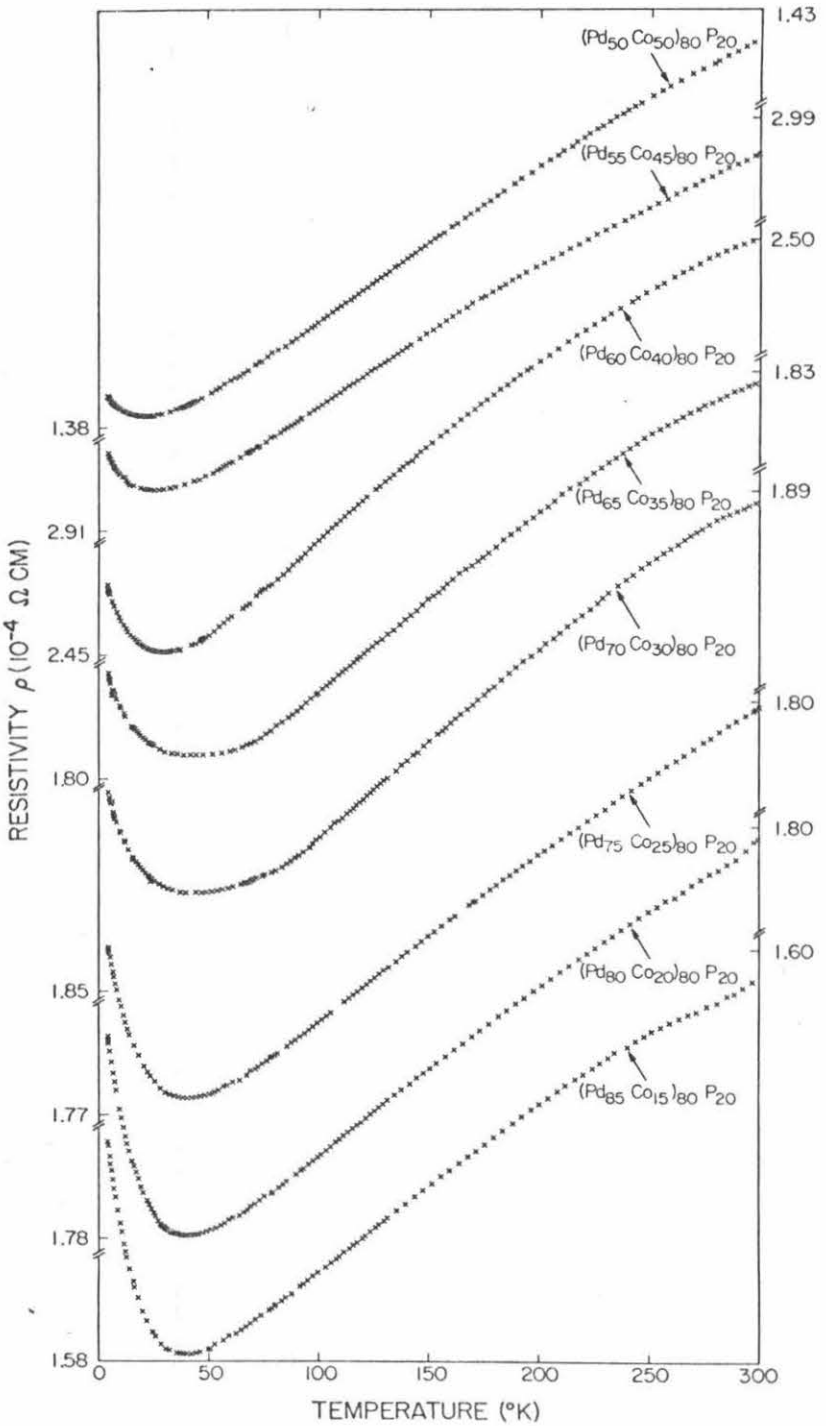

Fig. 26. Electrical resistivity at low temperatures of $(Pd_{100-x}Co_x)_{80}P_{20}$

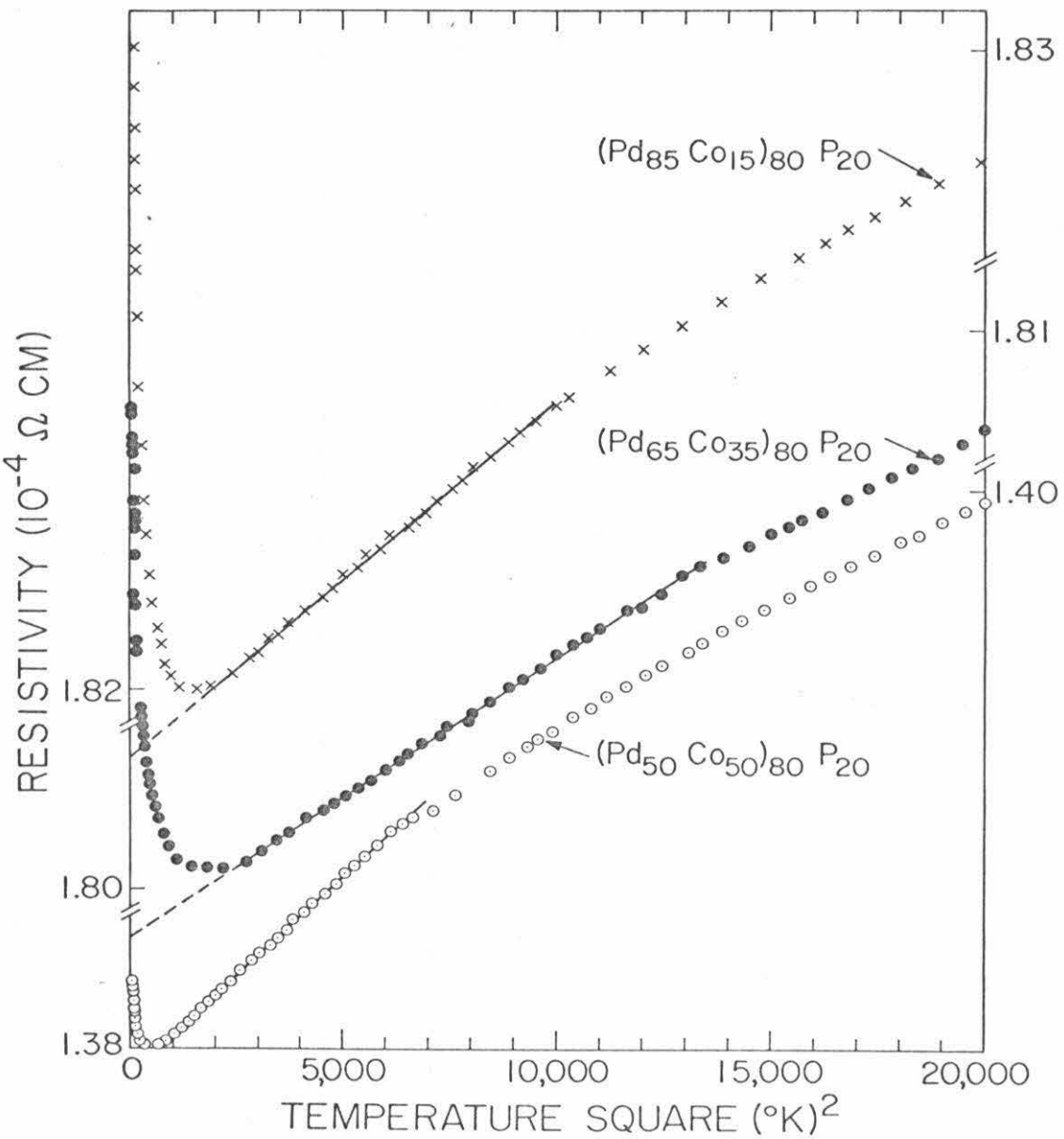

Fig. 27. Electrical resistivity versus T^2 of amorphous $(Pd_{100-x}Co_x)_{80}P_{20}$

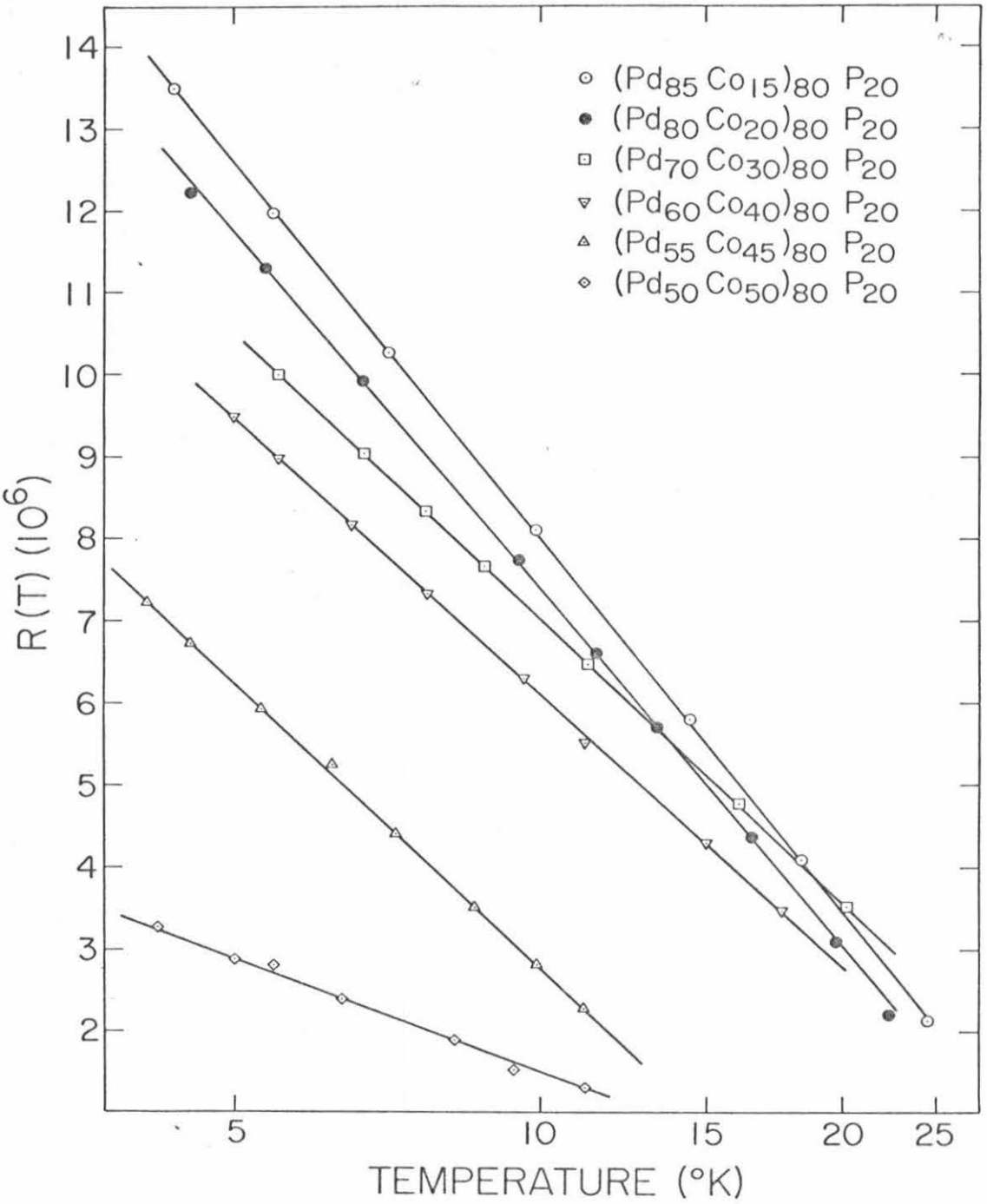

Fig. 28. Residual resistivity versus ℓn T of amorphous $(Pd_{100-x}Co_x)_{80}P$

and ρ_{min} (the resistivity minimum), $(\rho_{max} - \rho_{min})/\rho_{min}$ and $(\rho_{300} - \rho_{200})/\Delta T$ which will be used in the discussion.

b. Palladium-manganese-phosphorus alloys

The temperature dependence of electrical resistivity of these alloys is shown in Figs. 29 and 32. As was explained in (IV-B.1) the presence of a magnetic transition element, a high valence electron donor "phosphorus", and structural disorder, resulted in localized electronic states in Pd-Mn-P alloys. The interesting feature is that $d\rho/dT$ is negative and of the order of 10 to 20 (10^{-2} $\mu\Omega$-cm) with phosphorus concentration having a larger effect on the slope of the resistivity temperature curve than manganese. The room temperature electrical resistivity increases with both manganese and phosphorus concentrations. The somewhat high resistivity in Pd-Mn-P[155] compared to other Pd-M-P alloys where M stands for a transition "3d" metal suggests an appreciable spin disorder contribution which is still noticeable in the helium range. As shown, these alloys possess at lower temperature an additional temperature dependent negative contribution to the resistivity which is maximum for 15 at.% Mn and smears out as the concentration of Mn increases to 38 at.%. This additional negative contribution generally obeys the logarithmic law of Kondo. For $T < 10^{o}K$ the resistivity is proportional to T^2.

The behavior of the resistivity above $200^{o}K$ may be interpreted in terms of the magnitude of the localization of the electrons. This is clearly seen in the expression $\rho_{300} - \rho_{\ell}/\Delta T$ where ρ_{ℓ} is the onset of the almost linear region, as the concentration of phosphorus changes from 17 to 26 at.%. To interpret these observations, a

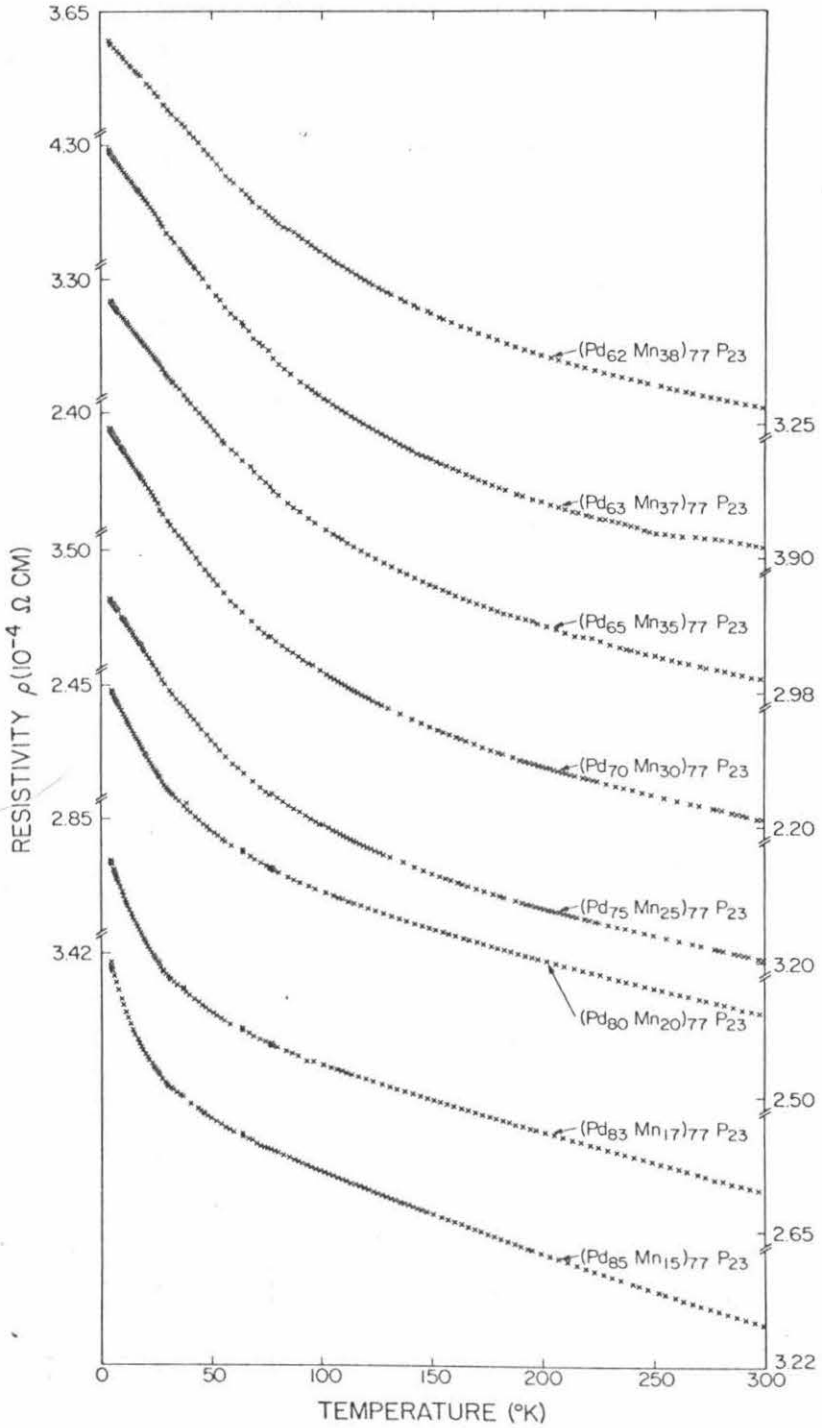

Fig. 29. Electrical resistivity versus temperature for amorphous $(Pd_{100-x}Mn_x)_{77}P_{23}$

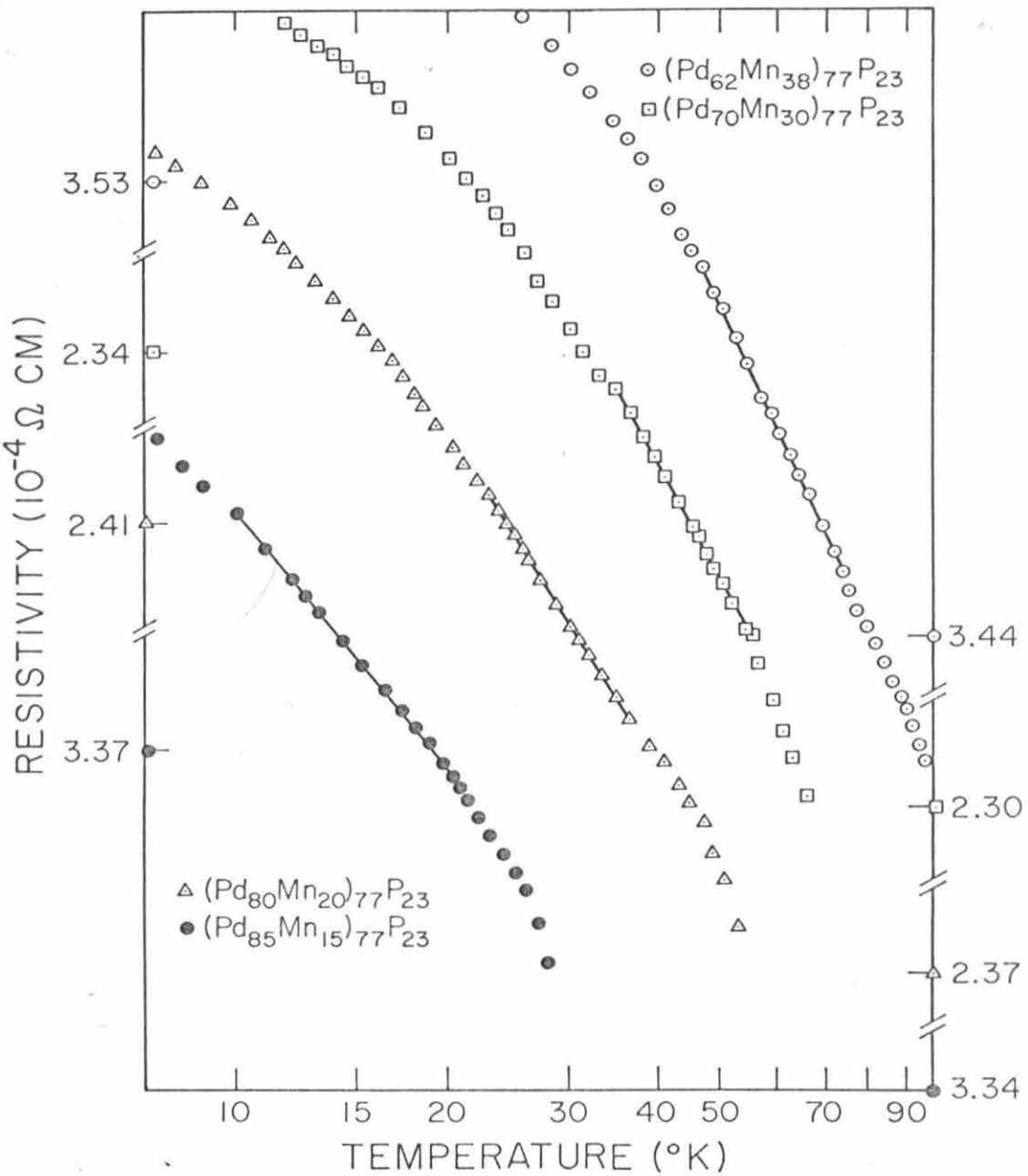

Fig. 30. Resistivity versus ℓn T of amorphous $(Pd_{100-x}Mn_x)_{77}P_{23}$

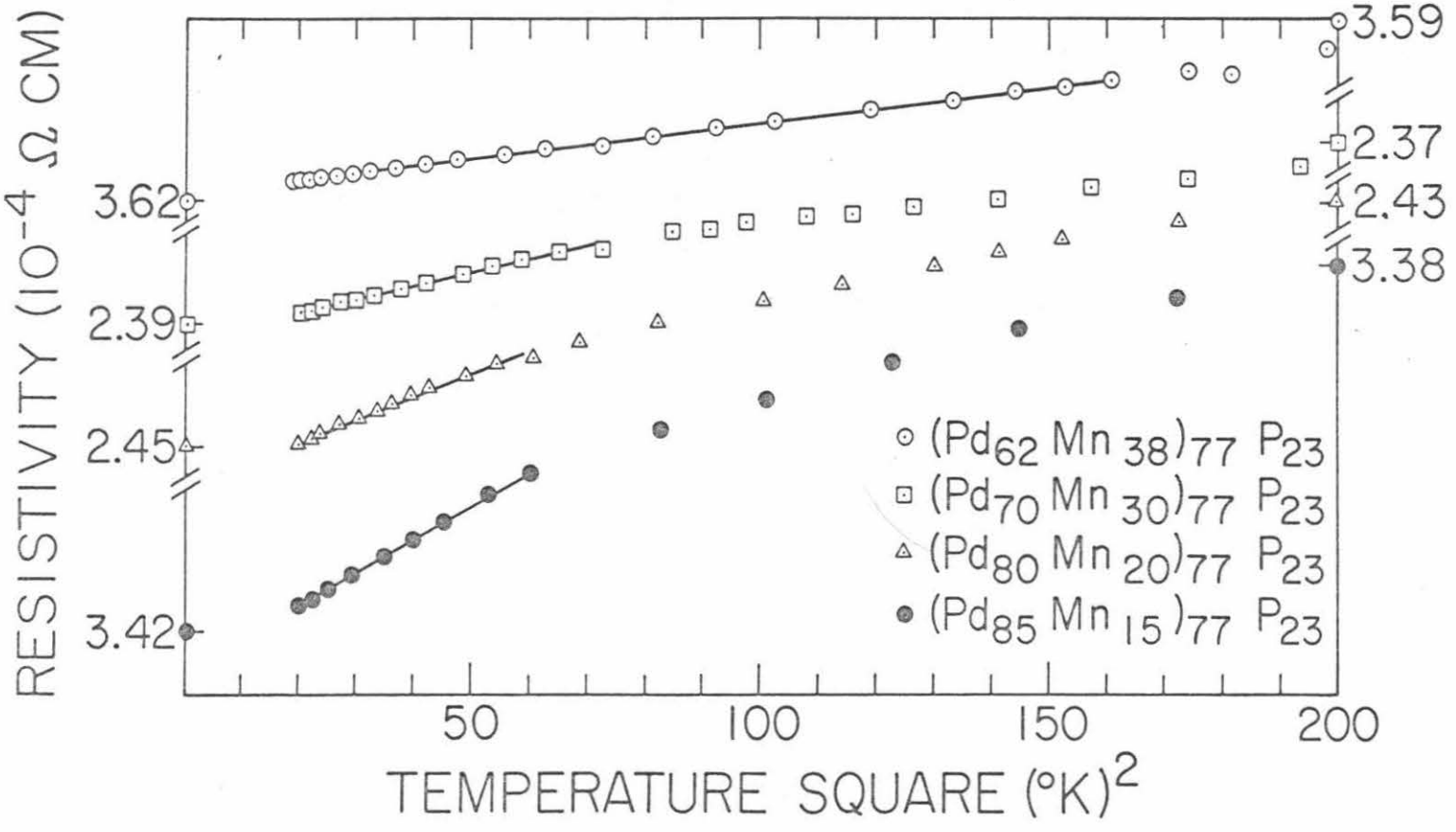

Fig. 31. Resistivity versus T^2 of amorphous $(Pd_{100-x}Mn_x)_{77}P_{23}$

Table XVI. Coefficients of Electrical Resistivity

Composition	Sample #	$\rho_{max}^{4.2^oK}$ $10^{-4}\Omega$ cm	$\rho_{4.2}-\rho_{300^oK}$ $10^{-5}\Omega$ cm	T^2range (^oK)	T_d (^oK)	T'_d (^oK)	γ $10^{-7}\Omega$ cm/^oK	$\frac{\rho_\ell-\rho_{300}}{\Delta T}$ $10^{-8}\Omega$ cm
$(Pd_{62}Mn_{38})_{77}P_{23}$	1	3.621	3.54	12.0	44.3	73.2	0.78	4.817
	2	3.137	4.04		47.5	68.9		4.087
$(Pd_{63}Mn_{37})_{77}P_{23}$		4.296	3.85	11.2	45.2	70.3	0.92	3.949
$(Pd_{65}Mn_{35})_{77}P_{23}$		3.283	2.94	10.1	39.2	65.1	1.17	4.255
$(Pd_{70}Mn_{30})_{77}P_{23}$	1	2.452	2.49	8.1	34.9	50.4	1.36	2.706
	2	2.319	2.32		35.2	52.1		3.317
$(Pd_{75}Mn_{25})_{77}P_{23}$		3.465	2.63	7.7	30.2	43.2	1.47	3.959
$(Pd_{80}Mn_{20})_{77}P_{23}$	1	2.447	1.60	7.3	23.4	35.4	1.54	2.846
	2	3.970	2.70		21.3	32.1		3.111
$(Pd_{83}Mn_{17})_{77}P_{23}$		2.829	2.22	8.2	16.1	25.2	1.82	3.048
$(Pd_{85}Mn_{15})_{77}P_{23}$	1	3.453	1.31		12.1	18.1		3.268
	2	3.416	1.76	7.7	10.0	20.4	2.33	3.719

Table XVII. Electrical Resistivity Parameters

Composition	Sample #	β $10^{-7}\Omega$ cm/$^oK^2$	T_K (^oK)	ρ_o $10^{-4}\Omega$ cm	β_{LSF} $10^{-7}\Omega$ cm	T_{LSF} (^oK)	T_c (^oK)	T_ℓ (^oK)
$(Pd_{62}Mn_{38})_{77}P_{23}$	1	5.97	80.3	3.6814	6.149	443.4	221.7	224.2
	2							221.8
$(Pd_{63}Mn_{37})_{77}P_{23}$		4.93	-	-	5.968	431.9	215.4	219.8
$(Pd_{65}Mn_{35})_{77}P_{23}$		3.48	-	-	3.812	409.6	204.8	206.4
$(Pd_{70}Mn_{30})_{77}P_{23}$	1	2.18	58.2	2.5107	2.388	368.6	184.3	182.5
	2							186.7
$(P_{75}Mn_{25})_{77}P_{23}$		1.29	-	-	1.427	365.3	152.7	166.2
$(Pd_{80}Mn_{20})_{77}P_{23}$	1	0.84	41.6	2.5067	0.997	264.7	132.3	124.3
	2							127.5
$(Pd_{83}Mn_{17})_{77}P_{23}$		0.53	-	-	0.654	234.8	117.5	113.9
$(Pd_{85}Mn_{15})_{77}P_{23}$	1							91.3
	2	0.29	28.4	3.4781	0.2607	209.5	104.70	89.5

phenomenological formula for the resistivity for $T < 200^{o}K$ may be written as

$$\rho = \rho_{o} - [\alpha + \beta(T/\theta)^{2} - \gamma \ell n\ T + \varepsilon T] \qquad (38)$$

where α represents the temperature independent part of the resistivity, $\beta_{N}T^{2}$ is the Nagoaka spin compensated state by conduction electron at $\theta = 1$, while β_{LSF} is the localized spin fluctuation parameter at the spin fluctuation temperature $\theta = T_{LSF}$. The third term is the Kondo type contribution to the resistivity and εT is the non-magnetic temperature dependent resistivity. Using the phenomenological equation (38) it was possible to determine the temperature dependent part of the resistivity $\rho_{spin}(T)$ by plotting $\rho(T)$ versus $\ell n\ T$, Figs. 30 and 33. The ρ_{spin} varied as $\gamma \ell n\ T$ in the range $T_{d} < \rho_{spin} < T_{d}'$ where T_{d} is the temperature at which ρ_{spin} deviates from the logarithmic temperature dependence and T_{d}' is the onset of the logarithmic temperature dependence. Figs. 31 and 34 show the T^{2} temperature range of resistivity. Tables XVI and XVIII show ρ_{max} at $4.2^{o}K$, at which, due to its scattering values, no trend with composition was detected. $(\rho_{4.2} - \rho_{300^{o}K})$, which increases with both phosphorus and manganese concentration, is explainable in terms of higher electron phonon scattering, since the number of conduction electrons increases; and $(\rho_{\ell} - \rho_{300^{o}K})/T$ reflects the slope of the high temperature range of resistivity where ρ_{ℓ} is the onset of the flattened range of the resistivity curve.

The slope of the resistivity versus temperature increases between 1.04 and 6.29 ($10^{-8}\Omega$ cm/^{o}K) in the range of temperature between

200 and 300°K as the concentration of phosphorus increases between 17 and 26 at.%. This behavior will be used as an indication of the magnitude of the electron localization with change in metallic composition and glass former content. The parameters of resistivity T_d, T_d', T^2 range, β, α, are listed in Tables XVII and XIX. The temperature T_d' varies linearly with Mn concentration as shown in Fig. 58. Below T_d, $\Delta\rho$ increases more slowly than $-\ell n\ T$, approaching a constant value at lower temperatures. These observations can be explained in terms of the formation of quasibound[73] spin localized states. The lowest temperature range of the resistivity was computer fitted once to Nagaoka spin compensated state formula[73]

$$\rho = \rho_o[1 - \beta_N(T/T_K)^2] \tag{39}$$

giving ρ_o and T_K, and another time in the LSF expression[69] for low temperatures

$$\rho = \rho_o'[1 - \beta_{LSF}\frac{\gamma^2}{3}(T/T_{LSF})^2] \tag{40}$$

to obtain β_{LSF} and T_{LSF}. The results are listed in Tables XVIII and XIX, T_c being the Kaiser-Doniach transition from T^2 to T dependence of the resistivity which occurs around $T_c = 0.5\ T_{LSF}$. The resistivity of high manganese, high phosphorus $(Pd_{62}Mn_{38})_{75}P_{25}$ is shown in Fig. 35.

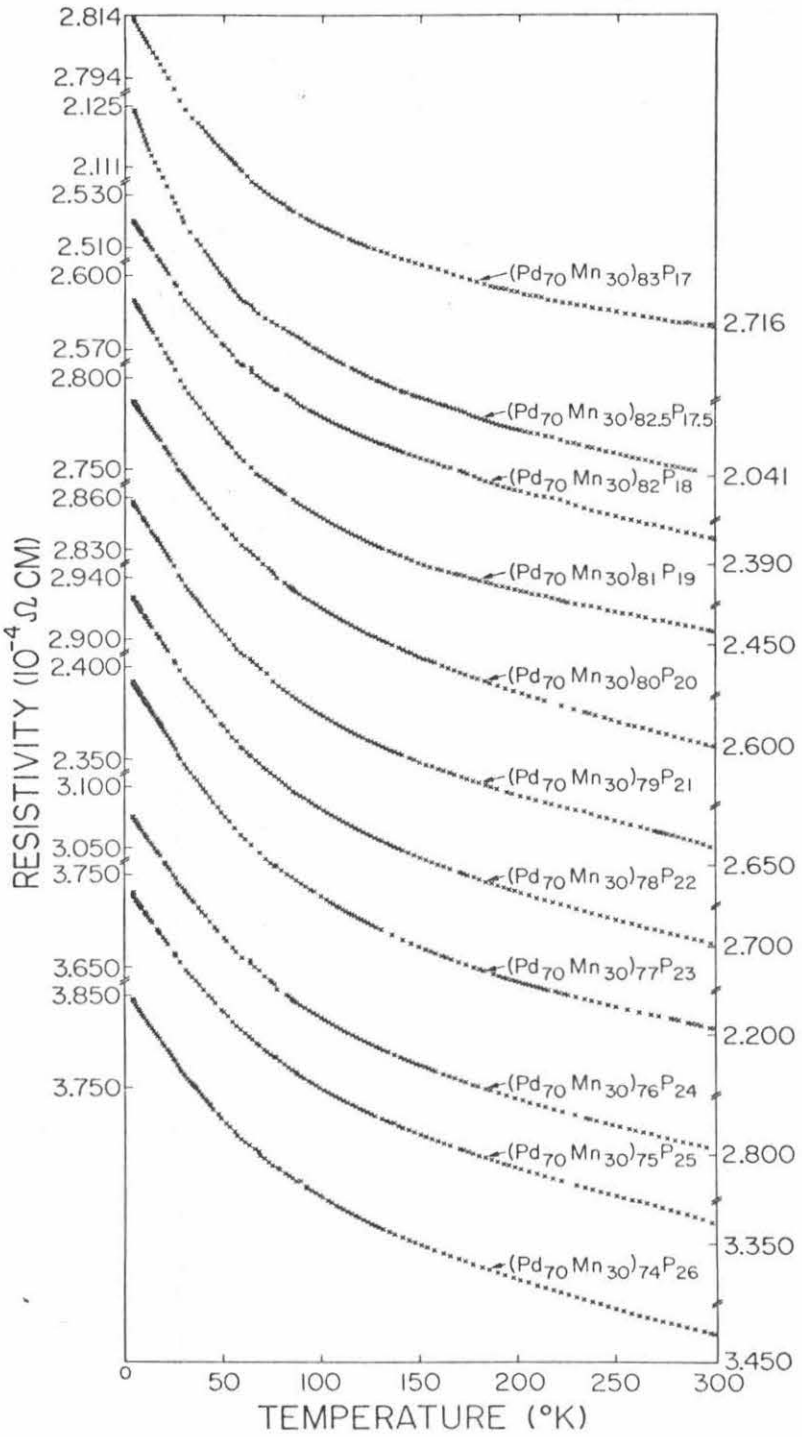

Fig. 32. Electrical resistivity versus temperature for amorphous $(Pd_{70}Mn_{30})_{100-y}P_y$. The scale of the resistivity varies from graph to graph.

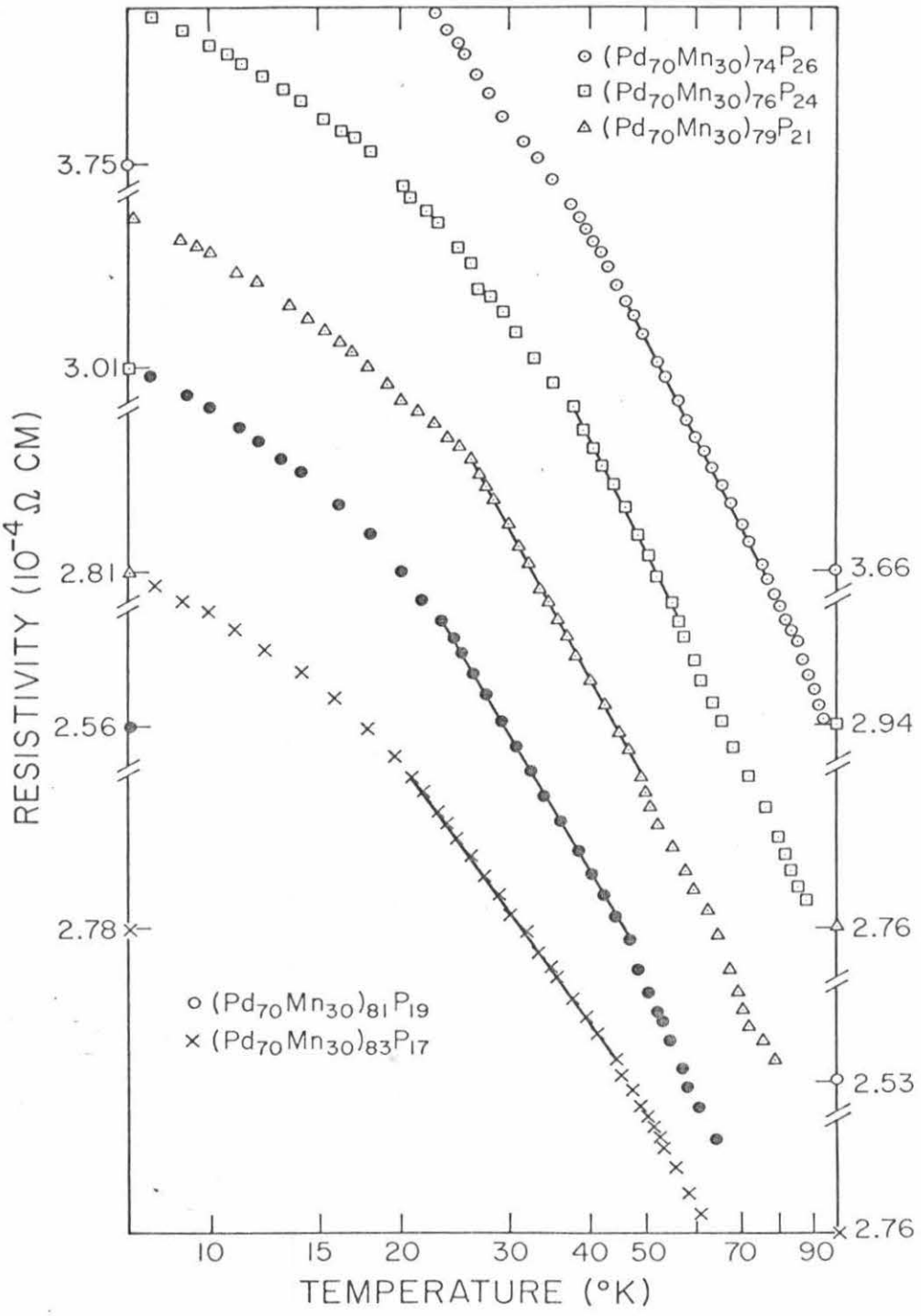

Fig. 33. Resistivity versus ℓn T of amorphous $(Pd_{70}Mn_{30})_{100-y}P_y$

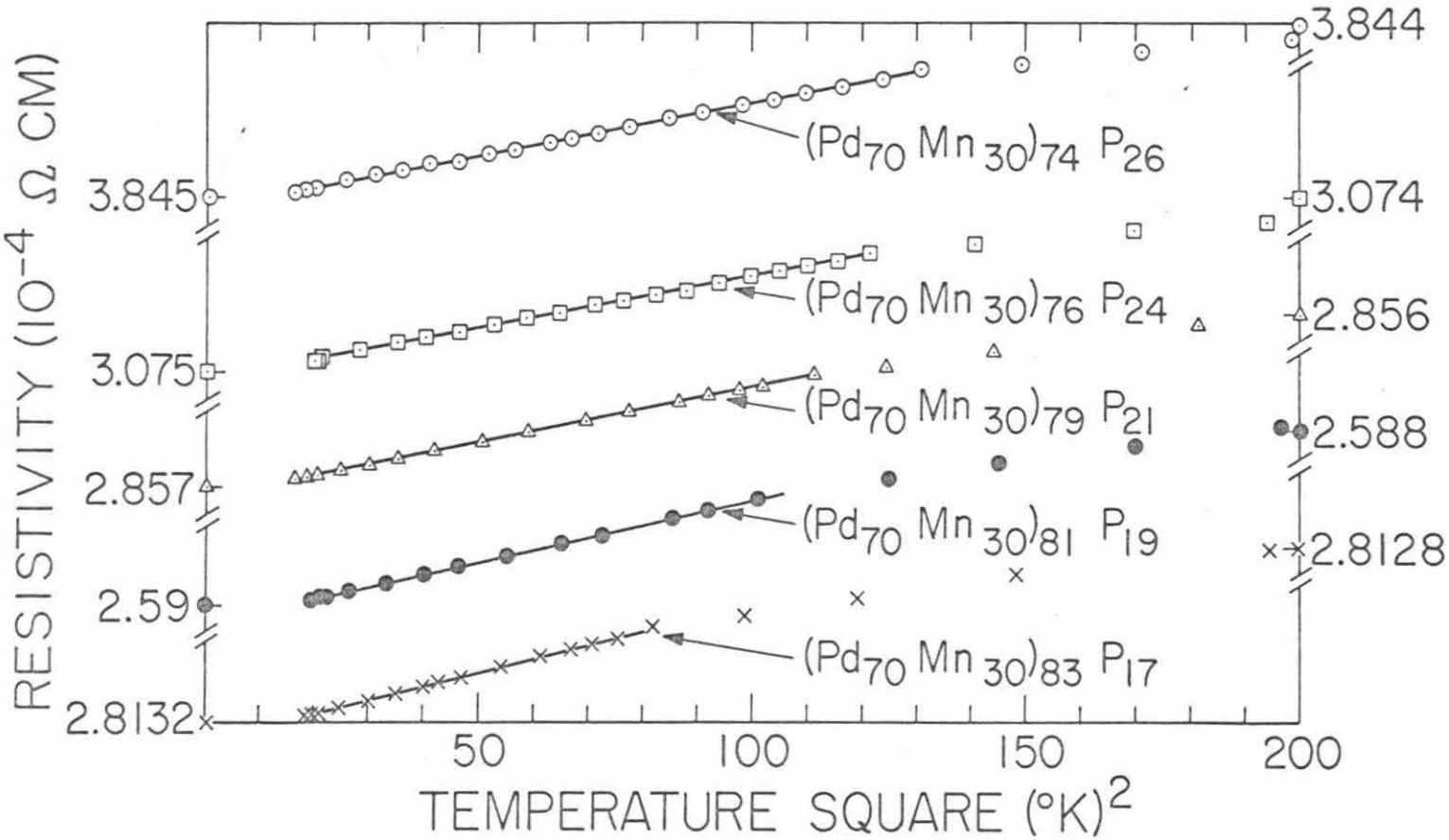

Fig. 34. Resistivity versus T^2 of amorphous $(Pd_{70}Mn_{30})_{100-y}P_y$

Table XVIII. Coefficients of Electrical Resistivity

Composition	Sample #	ρ_{max} 4.2°K $10^{-4}\Omega$ cm	$\rho_{4.2}-\rho_{300°K}$ $10^{-5}\Omega$ cm	$\frac{\rho_{200}-\rho_{300}}{\Delta T}$ $10^{-8}\Omega$ cm	T^2_{range} (°K)	T_d (°K)	T'_d (°K)	γ $10^{-7}\Omega$ cm/°K
$(Pd_{70}Mn_{30})_{83}P_{17}$	1	2.8132	1.16	1.04	8.1	21.7	43.8	0.88
	2	2.0151	1.08	1.28				
$(Pd_{70}Mn_{30})_{82.5}P_{175}$		2.1237	0.82	1.07	11.2	19.0	43.4	0.81
$(Pd_{70}Mn_{30})_{82}P_{18}$	1	2.8125	1.38	2.36	9.1	22.5	48.1	0.96
	2	2.5199	1.20	1.82	8.7	20.6	42.6	
$(Pd_{70}Mn_{30})_{81}P_{19}$		2.6098	1.54	1.49	10.2	22.4	48.0	1.15
$(Pd_{70}Mn_{30})_{80}P_{20}$		2.7871	1.87	3.00	9.1	23.3	47.1	1.40
$(Pd_{70}Mn_{30})_{79}P_{21}$		2.8575	1.98	3.02	10.7	26.4	48.1	1.32
$(Pd_{70}Mn_{30})_{78}P_{22}$	1	2.6238	1.98	2.93				
	2	2.9274	2.26	3.34	9.2	29.4	46.2	1.62
$(Pd_{70}Mn_{30}{}_{77}P_{23}$	1	2.4518	2.49	2.56	8.3	34.9	50.4	1.36
	2	2.3194	2.32	3.43		35.2	52.1	
$(Pd_{70}Mn_{30})_{76}P_{24}$		3.0754	2.71	4.25	11.2	38.5	54.3	1.85

Table XVIII - Continued

Composition	Sample #	$\rho_{max}^{4.2^oK}$ $10^{-4}\Omega$ cm	$\rho_{4.2}-\rho_{300^oK}$ $10^{-5}\Omega$ cm	$\frac{\rho_{200}-\rho_{300}}{\Delta T}$ $10^{-8}\Omega$ cm	T^2_{range} (^oK)	T_d (^oK)	T'_d (^oK)	γ $10^{-7}\Omega$ cm/^oK
$(Pd_{70}Mn_{30})_{75}P_{25}$	1	4.2526	3.57	6.14				
	2	3.7287	3.56	5.97	9.6	43.7	66.5	1.93
$(Pd_{70}Mn_{30})_{74}P_{26}$	1	3.8453	3.65	5.98	13.1	49.3	71.9	
	2	3.6796	3.34	6.29	11.4	48.5	73.2	1.12
$(Pd_{62}Mn_{38})_{75}P_{25}$	1	3.3736	3.52	5.13	14.1	50.3	73.8	1.98
	2	3.5175	3.61	5.26	18.8	52.9	75.1	2.12

Table XIX. Electrical Resistivity Parameters

Composition	β_N $10^{-7}\Omega$ cm/$^oK^2$	T_K (^oK)	ρ_o $10^{-4}\Omega$ cm	β_{LSF} $10^{-7}\Omega$ cm	T_{LSF} (^oK)	T_c (^oK)	T (^oK)
$(Pd_{70}Mn_{30})_{83}P_{17}$	1.90	55.8	2.894	2.106	432.6	216.3	220
$(Pd_{70}Mn_{30})_{81}P_{19}$	2.15	61.9	2.683	2.231	437.4	218.7	223
$(Pd_{70}Mn_{30})_{78}P_{22}$	2.62	58.3	2.983	2.493	428.6	214.3	218
$(Pd_{70}Mn_{30})_{76}P_{24}$	2.94	72.8	3.792	2.652	448.2	224.6	232
$(Pd_{62}Mn_{38})_{75}P_{25}$	4.46	81.6	3.638	4.684	464.2	232.1	225

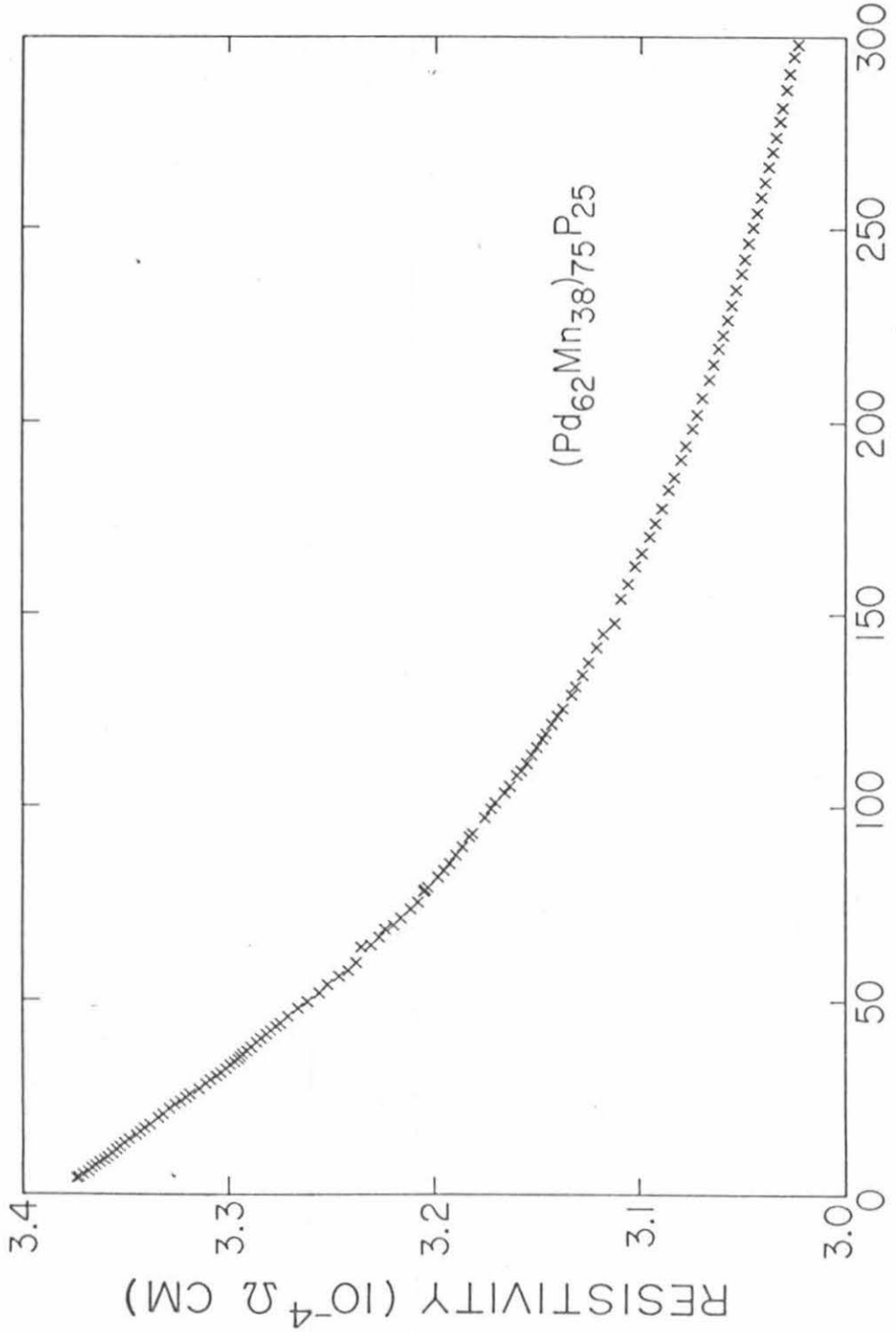

Fig. 35. Resistivity versus temperature of amorphous $(Pd_{62}Mn_{88})_{75}P_{25}$

2. High Temperature Measurements

The high temperature resistivity measurements were performed at a constant rate of heating of approximately 1.5 to 2.0°C/min. Under these conditions the resistivity versus temperature curves of all the amorphous alloys have almost the same shape up to the crystallization temperature. The behavior after crystallization depends on the intermediate phase or phases that come out which in turn depends on the composition. The resistivity increases with temperature (Pd-Co-P) Fig. 36, or decreases with a small temperature coefficient of the order of 10^{-4} μΩ cm per °K (Pd-Mn-P) Figs. 37 and 38, until a crystallization temperature t_{crys} is reached. At this temperature the resistivity drops sharply at first, then reaches a minimum before increasing again up to the melting point of the alloy.

The important results of the resistivity measurements are summarized in Tables XX and XXI. For each composition, the following characteristic parameters are given: the coefficient μ which is the slope of the change of resistivity with temperature determined between 300°K and the onset of crystallization, the crystallization temperature t_{crys} with a dispersion parameter Δt_{crys}, and the temperature t_N which is related to the small increase of resistivity for some Pd-Co-P shortly after crystallization. The absolute coefficient μ is higher in Pd-Mn-P than in Pd-Co-P. By increasing the transition metal content the resistivity slope increases, which is attributed to higher scattering from the localized electronic states. As expected, similar behavior is observed with increase in phosphorus content due to greater number of electrons being transferred from the

Table XX. Electrical Resistivity Parameters Above Room Temperature

Composition	μ $10^{-9}\Omega$ cm/^{o}K	$t_{crys} \pm \Delta t$	t_N	$\mu_{cooling}$ $10^{-8}\Omega$ cm
$(Pd_{50}Co_{50})_{80}P_{20}$	8.00	607.7 ± 20	-	12.4
$(Pd_{70}Co_{30})_{80}P_{20}$	8.32	623.1 ± 12	-	10.5
$(Pd_{80}Co_{20})_{80}P_{20}$	8.58	614.2 ± 8	642.3	9.60
$(Pd_{85}Co_{15})_{80}P_{20}$	8.72	618.8 ± 5	630.7	9.63

Table XXI. Electrical Resistivity Parameters above Room Temperature

Composition	μ $10^{-8}\Omega$ cm/^{o}K	$t_{crys} \pm \Delta t$	$\mu_{cooling}$ Ω cm/^{o}K
$(Pd_{85}Mn_{15})_{77}P_{23}$	-3.78	587.5 ± 10.6	2.1×10^{-8}
$(Pd_{62}Mn_{38})_{77}P_{23}$	-4.82	589.3 ± 17.8	7.8×10^{-8}
$(Pd_{70}Mn_{30})_{82}P_{18}$	-1.83	623.0 ± 18.0	1.9×10^{-8}
$(Pd_{70}Mn_{30})_{78}P_{22}$	-3.36	625.0 ± 22	0.7×10^{-8}
$(Pd_{70}Mn_{30})_{74}P_{26}$	-6.19	589.0 ± 25	-0.9×10^{-8}

glass former to the metal. The cooling curve shows interesting results. The temperature coefficient upon cooling is higher in Co than in Mn and is positive, which confirms the metallic character of the final crystalline phases. The decrease in the magnitude of the slope with decrease in transition metal contact is easily attributed to a decrease in metallic character. This belief is made clearer by the change of the phosphorus concentration which shows that the resultant phases after crystallization have a predominant metallic behavior for 18 at.%P, semi-metal for 22 at.%P, and a negative slope for 26 at.%P. From the experimental curves, it appears that the crystallization temperature is rather well defined; and it tends to change less with change in metal concentration than with change in glass former. As the temperature increases above T_{crys}, the resistivity decreases in one step $(Pd_{85}Mn_{15})_{77}P_{23}$ or in several steps $(Pd_{62}Mn_{38})_{77}P_{23}$. The intermediate crystalline steps in $(Pd_{100-x}Mn_x)_{77}P_{23}$ increase as the Mn content increases, while the crystallization temperature becomes broader and less sharply defined. In all alloys the irreversibility of the resistivity change was observed as it cooled from T (after crystallization) to T (lower temperatures) by a drastic change of slope. This confirms the concept of metastable intermediate phases and that additional increase in resistivity above the linear increases is not a reversible phenomenon and might be the result of structural changes in the amorphous alloy. Another remark is that in all Pd-Co-P alloys there is a slight change of slope around the Curie temperature which will be confirmed by magnetic and induction measurements.

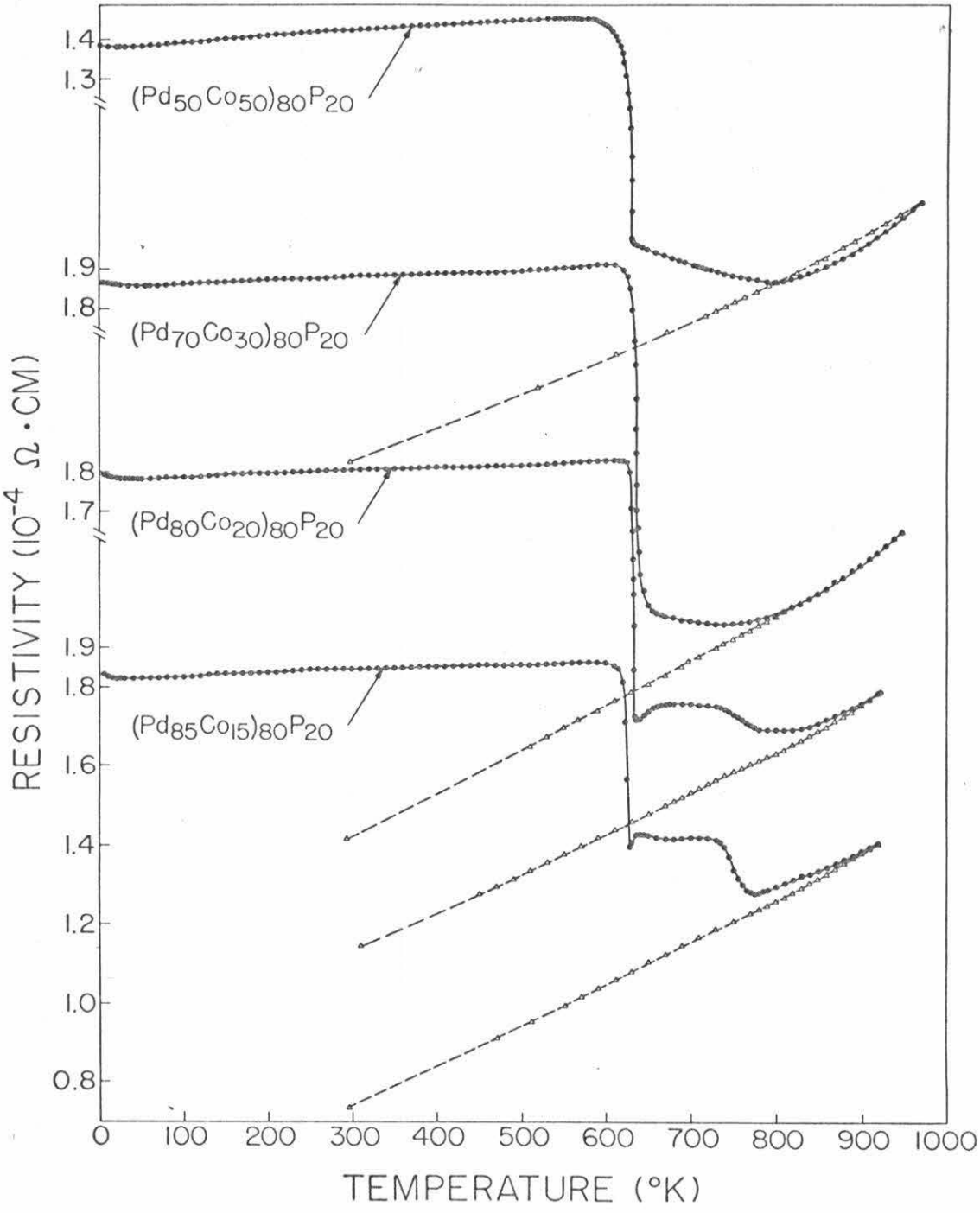

Fig. 36. Electrical resistivity of amorphous $(Pd_{100-x}Co_x)_{80}P_{20}$ measured with an average heating rate of 2 °C/min. The dashed lines reflect the cooling curves.

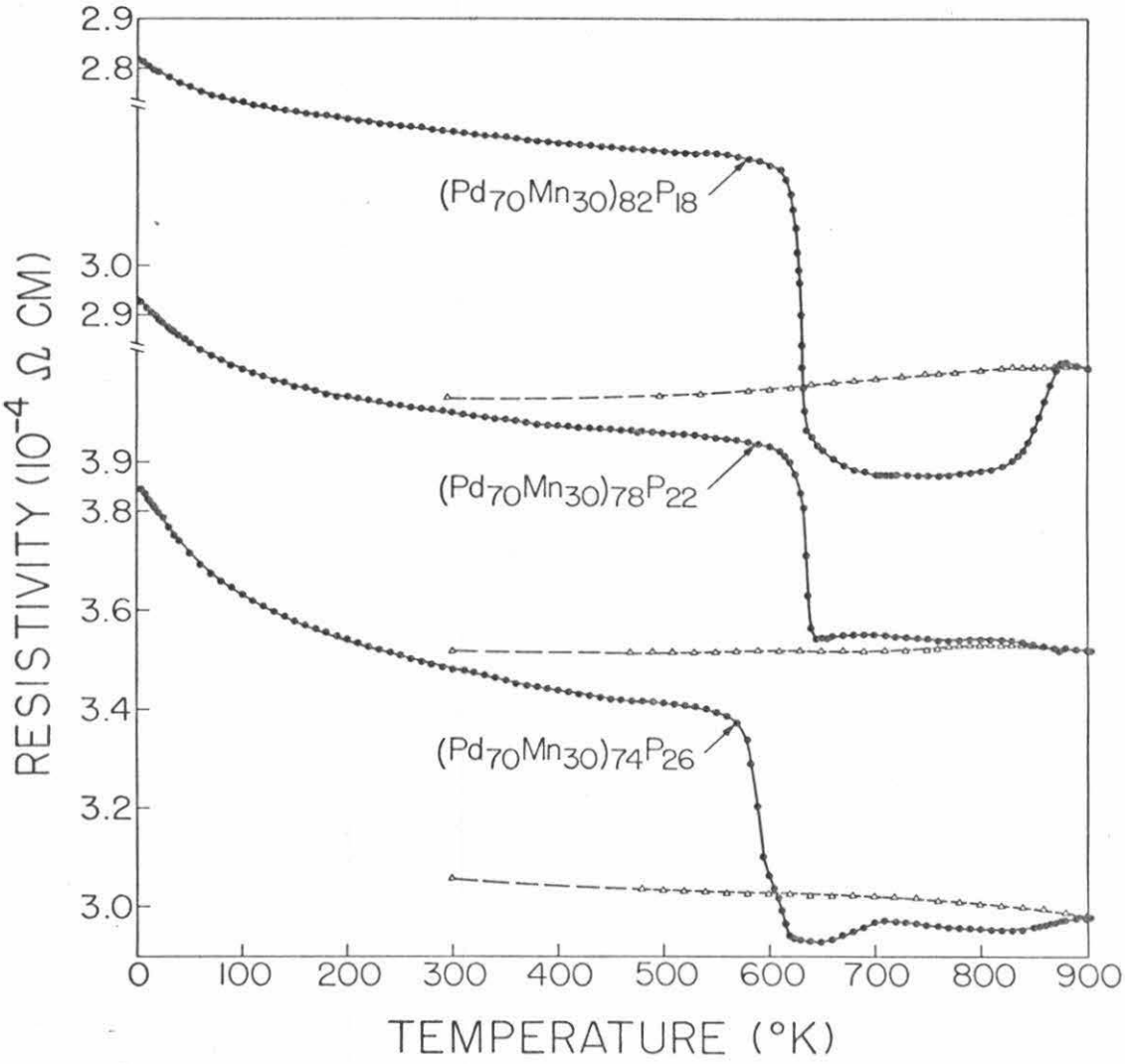

Fig. 37. Electrical resistivity of the amorphous $(Pd_{70}Mn_{30})_{100-y}P_y$. The dashed line reflects the cooling curve.

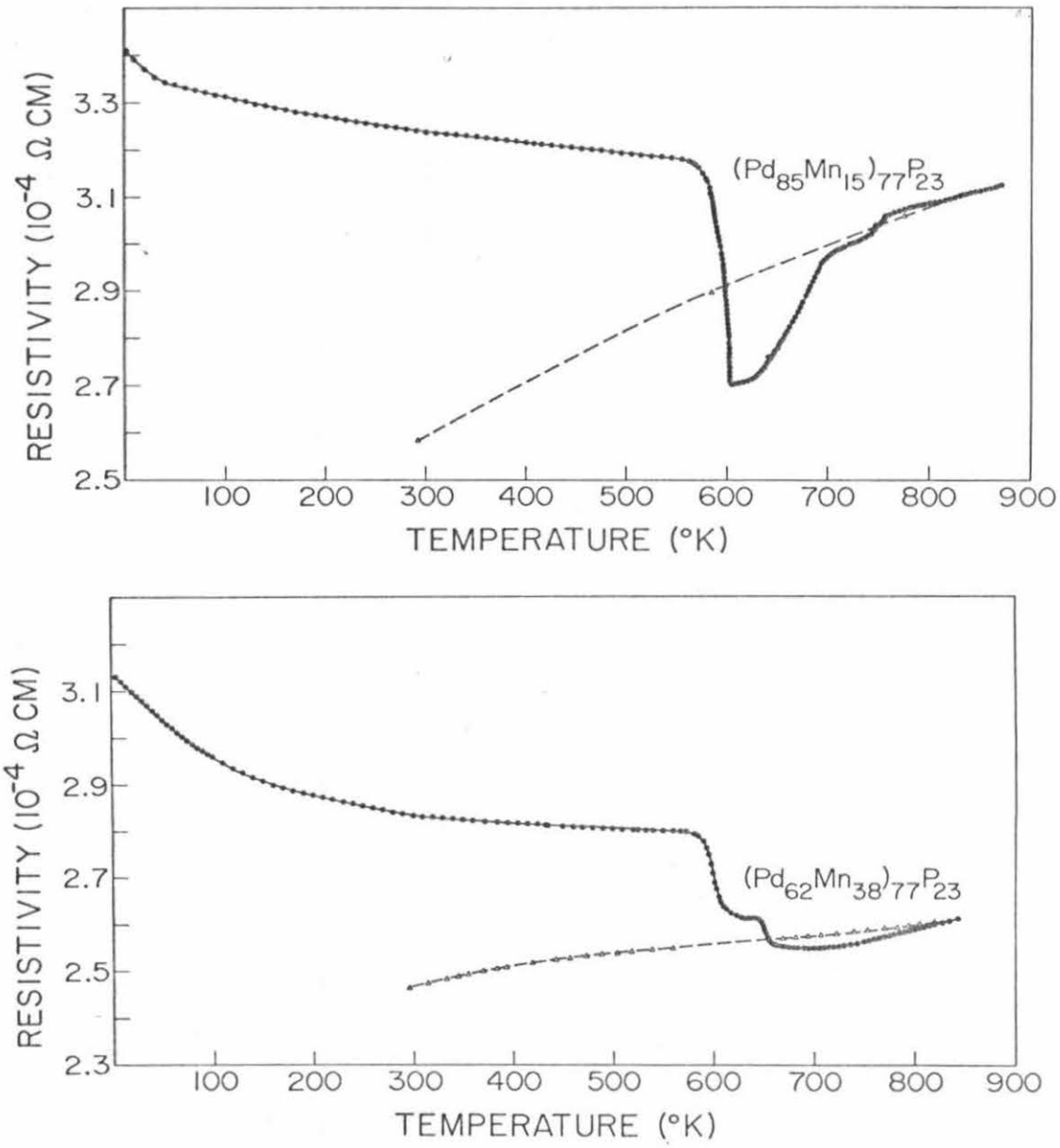

Fig. 38. Electrical resistivity of the two ends of the amorphous range of composition of the alloy system $(Pd_{100-x}Mn_x)_{77}P_{23}$. The dashed line reflects the cooling curve.

The high temperature resistivity measurements were partially helpful in following the crystallization process. The increase in resistivity in low cobalt amorphous alloys in the range $635^{o}K$ might be related to the formation of highly stressed crystalline regions. Such high stress regions in crystals probably act as additional scattering centers during the earliest stages of their existence before they are annealed out. The sharp drop in resistivity observed at T_{crys} corresponds to the rapid growth of crystalline metastable phases which revert to a phase mixture at higher temperatures.

V. MAGNETORESISTIVITY

A. Experimental Procedure

The specimens used in this study were the same as those used in the resistivity measurements. The transverse magnetoresistivity was measured for all of the amorphous Pd-Mn-P and Pd-Co-P alloys with the four-probe method at $T = 4.2^{o}K$. The magnetic field was applied perpendicular to the current and varied from zero to 10 kOe. Since in some cases the magnetoresistivity was very small, special attention was given to the selection of a current source. All measurements are reported in terms of $\Delta\rho_H$ divided by the zero field resistivity $\rho_{H=0}$ at $T = 4.2^{o}K$ which is plotted in terms of the applied magnetic fields.

B. Effect of Localized Spins on the Magnetoresistance of Amorphous Metals

In normal metals the quantity $(\rho-\rho_o)/\rho$ increases in a weak magnetic field H as H^2. This positive magnetoresistance generally obeys Kohler's rule which states that for alloys of differing residual resistance ρ_o, where $\Delta\rho$ is the change of resistance in a field H, the parameter $\Delta\rho/\rho_o$ is a function of H/ρ_o. This rule was explained in terms of the orbits of an electron in a magnetic field by assuming that the electron traverses only a small part of its orbit between collisions. The dimensions of this effect[74] are then

$$\Delta\rho/\rho_o = \text{constant } (eHL/mcv)^2 \qquad (41)$$

v is the Fermi velocity in the metal, L is the mean free path, and the others are well known parameters. The magnetoresistance becomes

quite different when, for instance, a small concentration of paramagnetic spins are introduced to a non-magnetic metal matrix or when the matrix becomes highly disordered. The effect of the magnetic field is then to decrease the resistivity. Schmitt[15] and Yosida[16] found that the relative change of resistance caused by the interaction between the conduction electron and the localized spin should be proportional to M^2, where M is the magnetization of the system consisting of these localized spins. Béal-Monod and Weiner[75] explained the theoretical basis of the negative magnetoresistance. Their results give

$$\Delta\rho_H = -\frac{3\pi m}{2E_F e^2 h} V_o J_{sd}^2 \sigma_\alpha^2 \{1 + (\frac{\mu_B}{\mu_{eff}})^2\} \qquad (42)$$

where e and m are the charge and mass of the electron, E_F the Fermi energy, J_{sd} the s-d exchange integral, x the atomic concentration of the transition metal, V_o the atomic volume, σ_α the magnetization of the transition metal in μ_β per atom, and μ_{eff} the effective magnetic moment. At lowest temperatures, deviations from the above equations may occur which Sasaki[76] attributes to the Kondo effect caused by the paramagnetic moments. The above equation is valid for $T > T_K$ but can be extended[16] to the case where $T \sim T_K$ if σ_α is the measured magnetization. Physically the negative magnetoresistance is due to the freezing out of the internal degree of freedom of the localized spin. The normal positive magnetoresistance may take over at strong magnetic fields or at a high concentration of weak or nonmagnetic metal content. This model satisfies the Anderson[11] theory of a low concentration of localized moment as found on manganese in

copper and as one would expect, Balkanski and Geisman[77] found that the negative magnetoresistance disappears in the case of heavily doped n-type silicon.

C. Experimental Results

Since the magnetoresistance at 300°K and 77°K are not large enough to be measured with any accuracy, only the data at 4.2°K are presented here. The results are shown in the form of $\Delta\rho_H/\rho_{Ho}$, where ρ_{Ho} is the resistivity at zero field. For Pd-Co-P the negative magnetoresistivity continuously increases with increase in cobalt concentration, Fig. 39, while for $(Pd_{100-x}Mn_x)_{77}P_{23}$ the negative magnetoresistivity increases from $x = 15$ to $x = 30$ at.% then decreases to be almost field independent for $n = 30$ at.% Mn as shown in Fig. 40. For $(Pd_{70}Mn_{30})_{100-y}P_y$ the magnetoresistivity is positive at low phosphorus content, $y = 17$ to 20 at.%, then changes sign and continuously increases with increase in phosphorus content up to $y = 26$ at.%, Fig. 41. An attempt will be made to explain the magnetoresistance behavior in terms of the transition metal concentration and the magnitude of localization.

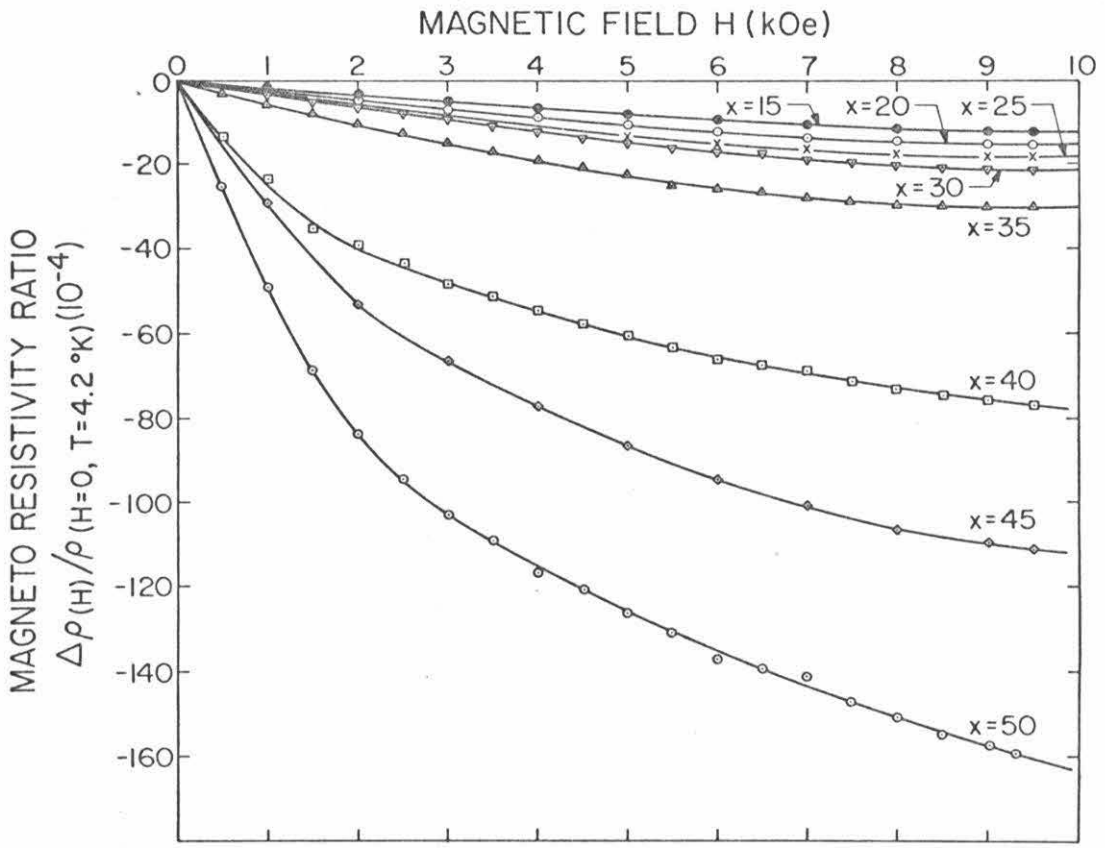

Fig. 39. Negative magnetoresistance ratio vs. magnetic field at 4.2°K for $(Pd_{100-x}Co_x)_{80}P_{20}$

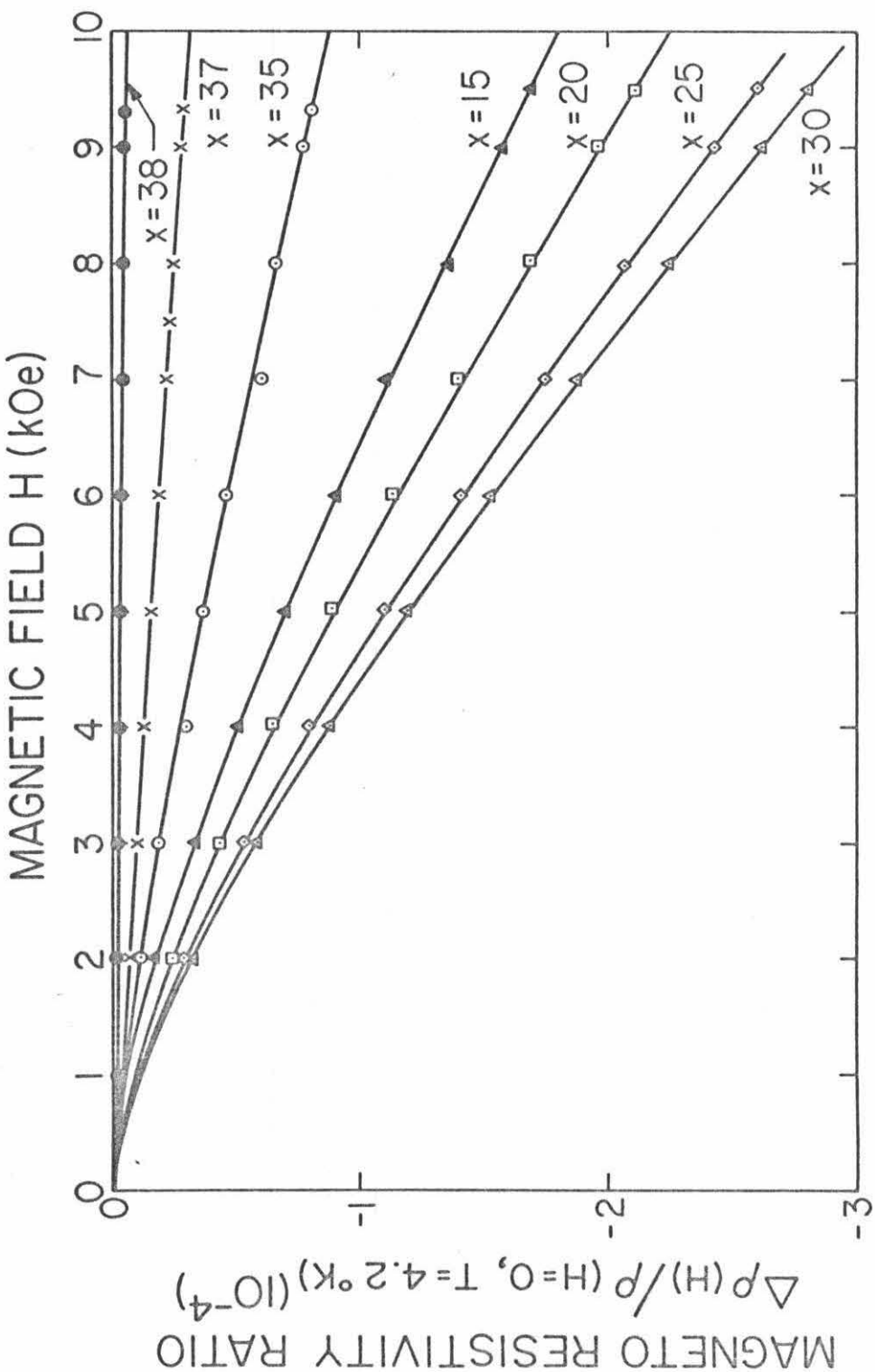

Fig. 40. Negative magnetoresistance ratio vs. magnetic field at 4.2°K for $(Pd_{100-x}Mn_x)_{77}P_{23}$

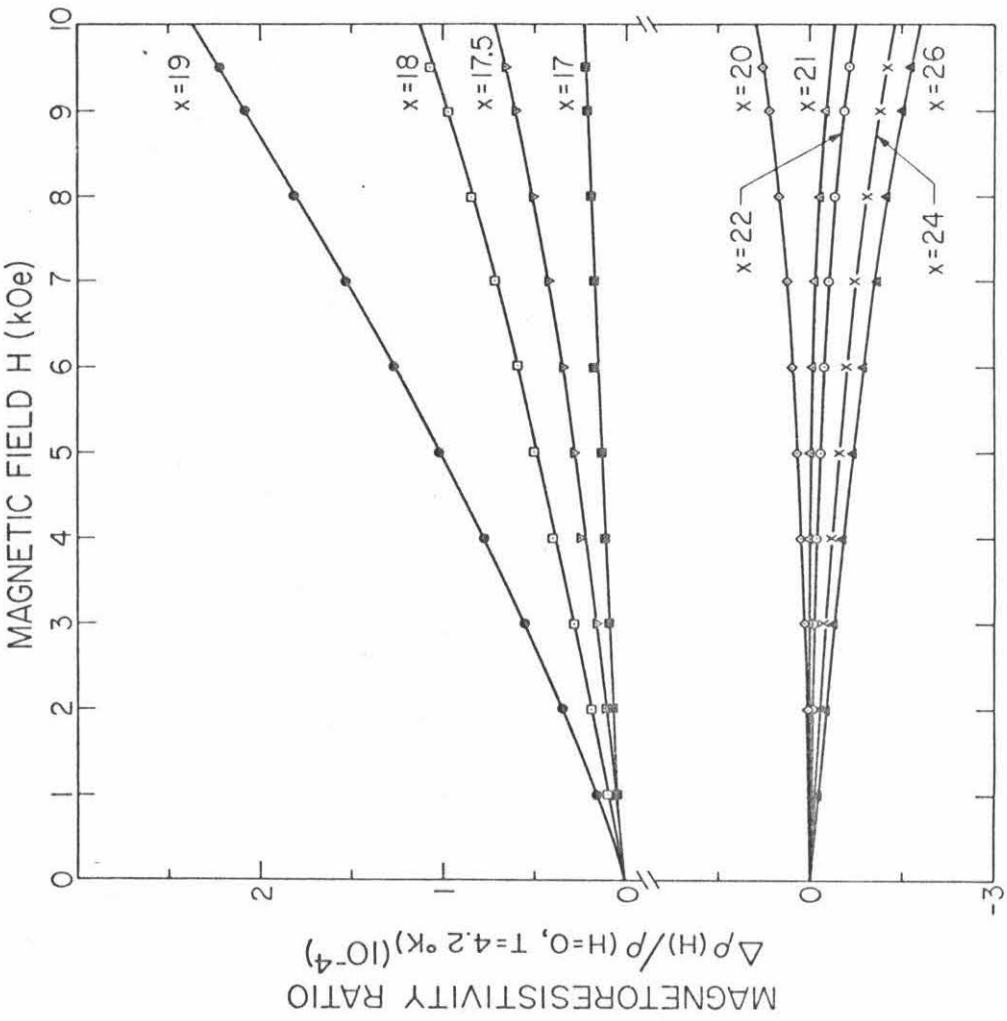

Fig. 41. Negative magnetoresistance ratio vs. magnetic field at 4.2°K for $(Pd_{70}Mn_{30})_{100-y}P_y$

VI. MAGNETIC PROPERTIES

The force F in dynes exerted on a sample of mass ((in grams) by a magnetic field of gradient dH/dZ (oersteds/cm) is given by $F = m\sigma\ (dH/dZ)$ where σ is the specific magnetization in cgs units per gram. For a paramagnetic substance, the specific magnetization is proportional to the applied field H (oersteds) so that the force is given by $F = m\chi H\ (dH/dZ)$ where χ, the magnetic susceptibility in cgs units per gram, is the proportionality constant. Thus σ and χ can be calculated in a straightforward manner from experimental measurement of the force exerted on the sample by a field gradient.

The susceptibility of a paramagnetic species can be represented by Curie-Weiss equation

$$\chi = \frac{C}{T - \theta_p}$$

where T is the absolute temperature and θ is the paramagnetic Weiss constant. The constant C is

$$C = \mu_{eff}^2/3k \quad \text{per atom}$$

where k is the Boltzmann constant and μ_{eff} is the effective paramagnetic moment per atom. The effective moment can be determined by plotting the reciprocal susceptibility versus temperature and obtaining the slope, $1/C$, of the linear portion. The Weiss constant is the extrapolation of this linear portion to $1/\chi = 0$. To determine the saturation magnetization of a substance, μ_{sat}, that is, the magnetization at infinite applied field, an extrapolation of the measured

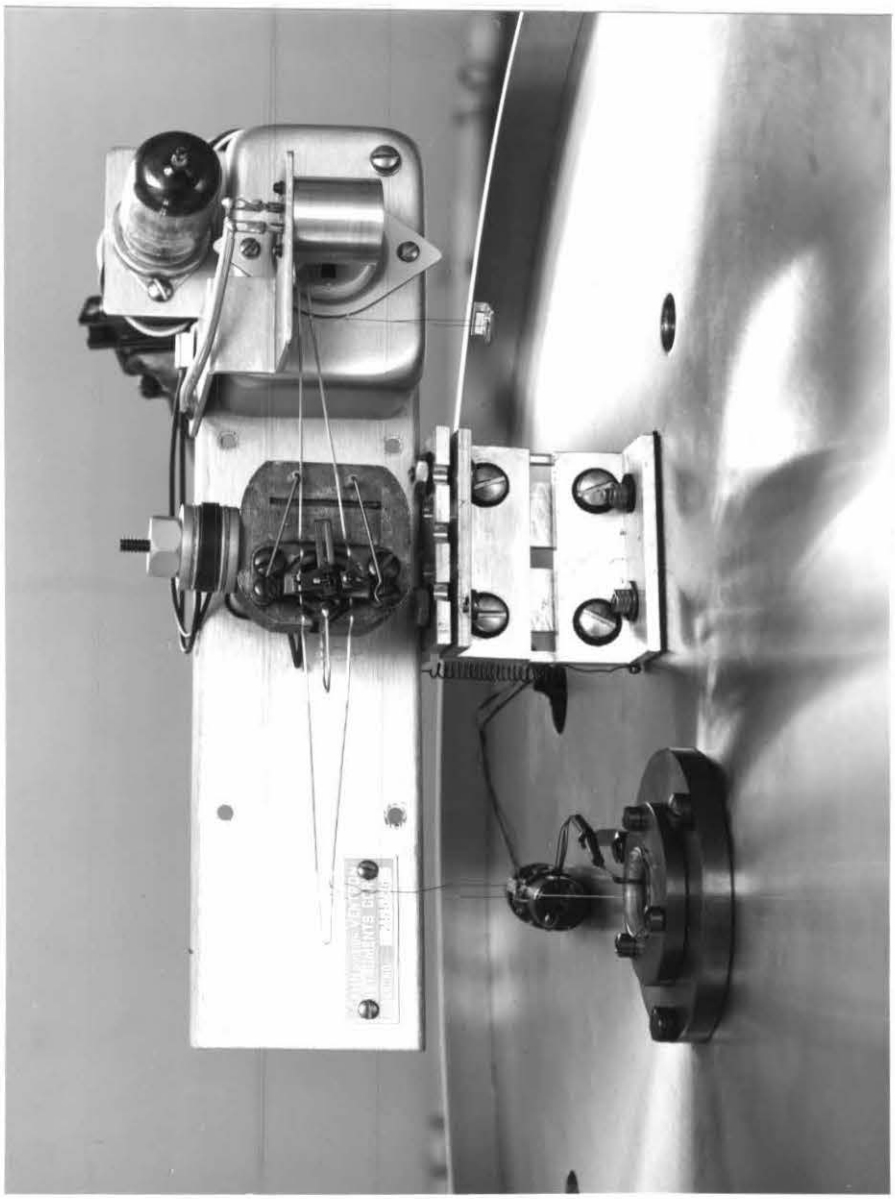

Fig. 42. Electromagnetic weighing mechanism

magnetization σ versus the reciprocal of the applied field was utilized. The effective field is the applied field minus the demagnetizing effect, or $H_{eff} = H - NI$ where N is the demagnetizing factor and I is the magnetization per volume. Then, $I_{sat} = d$ where d is the density. The demagnetizing factor is dependent on the shape of the sample. In the present experiments the thickness to diameter ratio of the thin states was 10^{-3} and as the samples were placed parallel to the lines of force, the demagnetization constant was assumed to be zero. To verify this assumption, an identical slab of nickel in disc form was used and the measured saturation magnetization differed by 0.8% from the theoretical M value for Ni. Magnetic moments are normally expressed in terms of the Bohr magneton. Specific magnetization is readily converted to the number of Bohr magnetons per atom by $\mu = M\sigma/BN$ where μ is the number of Bohr magnetons per formula unit, B is the value of the Bohr magneton (9.27×10^{-21} ergs/gauss), N is Avogadro's number, and M is formula weight.

A. Apparatus

All magnetic measurements were made using a 6-inch electromagnet equipped with a constant force pole cap. The force gradient was 10.25 kO_e^2/cm for 0.4 inches under a pole piece gap of 1 inch. The force exerted on the sample was measured using an R. G. Cahn null-balance, Fig. 42. The output of the electromagnetic balance was connected to a digital voltmeter which allowed a sensitivity of 5 microvolts for 0.1 microgram, at an accuracy of 10%. The temperature measurements were made with a GaAs TG cryogenic sensor with an excitation current of 10 μA. Its heat dissipation is 1.5×10^{-5} watts at $4^{o}K$

and its useful range is from below $1^{o}K$ to $400^{o}K$. No magnetic effect was claimed by the manufacturer up to 20 kOe. The sample was put into a gelatine capsule and suspended from the electrobalance with 0.003 inch quartz fiber. The balance under a bell jar was in connection with a quartz tube, housing the heater and the thermometer, while the gelatine capsule holding the sample was hanging freely from the balance. The sample chamber was supported into a standard dewar assembly. The magnetometer and peripheral apparatus are shown in Fig. 43. The magnetic field strength (H) was determined with a Bell incremental gaussmeter with an accuracy of 0.01%; however, because of the field gradient reported, the field accuracy was 0.05%.

The magnetic field gradient (dH/dZ) was determined by measuring the force on samples of known specific magnetization. Finally the force H(dH/dZ) was determined at several positions to determine the region of constant force by plotting H(dH/dZ) versus H .

B. Calibration

Spectrographically pure nickel and pure palladium containing 3 ppm of Fe were used as standards and the calibration was verified by comparison of the measured susceptibility with the susceptibility of pure $HgCo(SCN)_4$. The ultimate sensitivity of the magnetometer under the available conditions was 6×10^{-7} emu/g with a field of 7 kOe.

The calibration of the GaAs sensor was made against a standard Ge crystal and a calibrated standard Cu-Constantan thermocouple. The GaAs was then checked against the transit Curie point of nickel $358^{o}C$ and the transition temperature of palladium $90^{o}K$.

Fig. 43. Magnetometer and peripheral apparatus

The accuracy of the magnetization obtained for the above unit is estimated to be 1.5%. However, at small magnetization values or low fields below 1 kOe the uncertainty may reach 5 to 7%.

C. Measuring Technique

After preparation and x-ray investigation to determine if the sample is amorphous, small pieces were chosen in such a way as to evade irregularity due to rapid quenching and were put flat into the capsule so that the field in the magnet would be in the plane of the sample. The capsule was weighed empty and then with the sample. The amount of sample and the range of the mass dial was decided by the properties of the amorphous alloys. The dewar and bell jar assembly were pumped out and the sample chamber was filled with 10 mm Hg of helium gas. To determine the thermomagnetic properties from 4.2°K to 300°K at a constant field strength of 6 kOe the system was heated at the rate of 2°K per minute. The field dependency was obtained by increasing the field in steps of 0.5 kOe up to a maximum of 6.9 kOe, the force of interaction between the sample and the field was recorded at each step.

D. Experimental Results

1. Low Temperature Measurements

Magnetic moments of Pd-Co-P and Pd-Mn-P alloys were measured between 4.2 and 300°K in a magnetic field of 6.0 kOe. The magnetization curves are shown in Figs. 44, 46 and 48 for various compositions of the three series of amorphous alloys studied. The magnetic susceptibility is plotted as a function of temperature in Figs. 45, 47 and 49. The magnetization versus magnetic field of the two ends of the cobalt concentration at 300, 77 and 4.2°K is shown in Fig. 50. Similar results for $(Pd_{63}Mn_{37})_{77}P_{23}$ are shown in Fig. 51, as an example, as no variation in

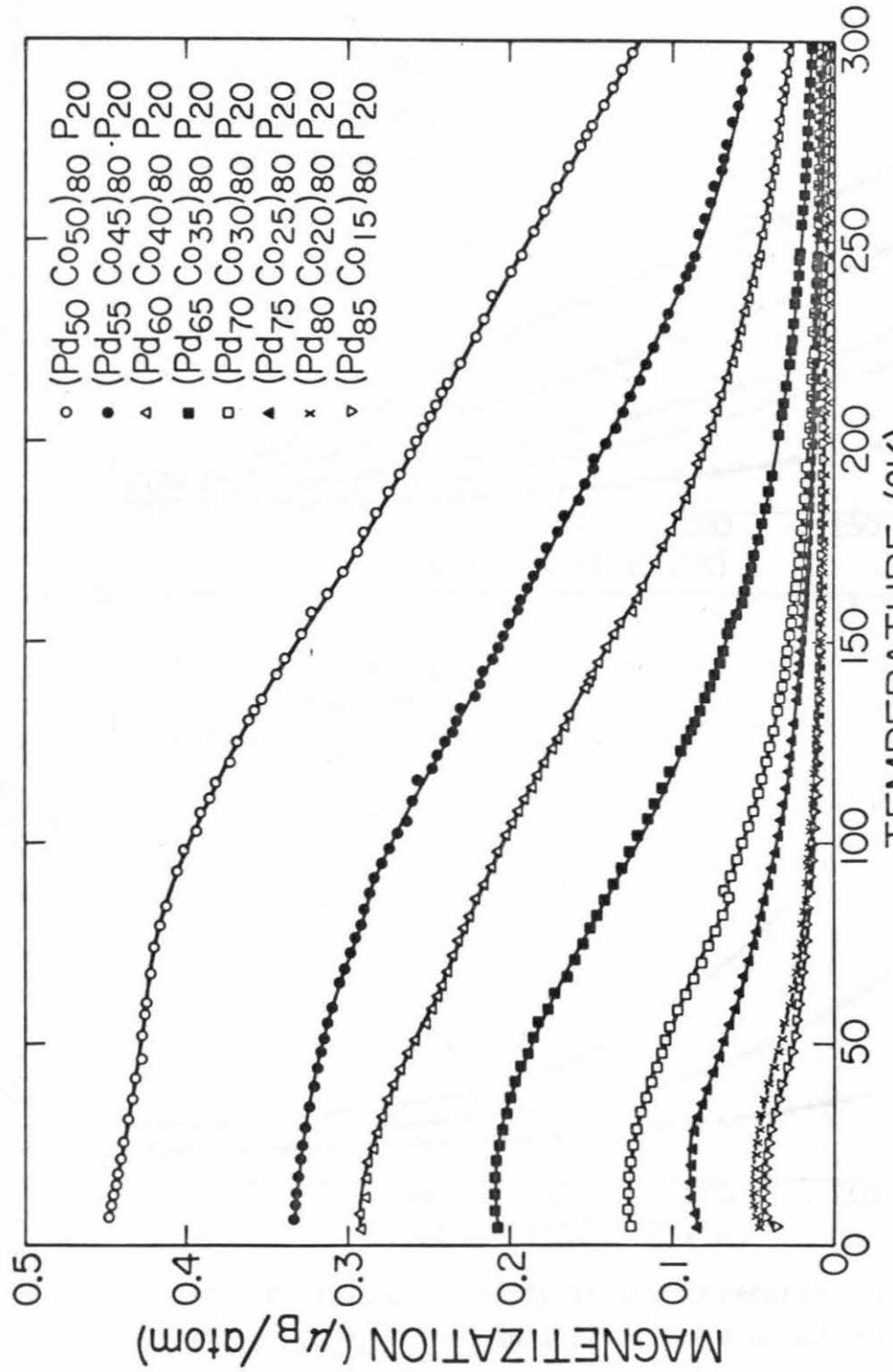

Fig. 44. Magnetic Moment versus Temperature curves for $(Pd_{100-x}Co_x)_{80}P_{20}$ at an applied field of 6.0 kOe

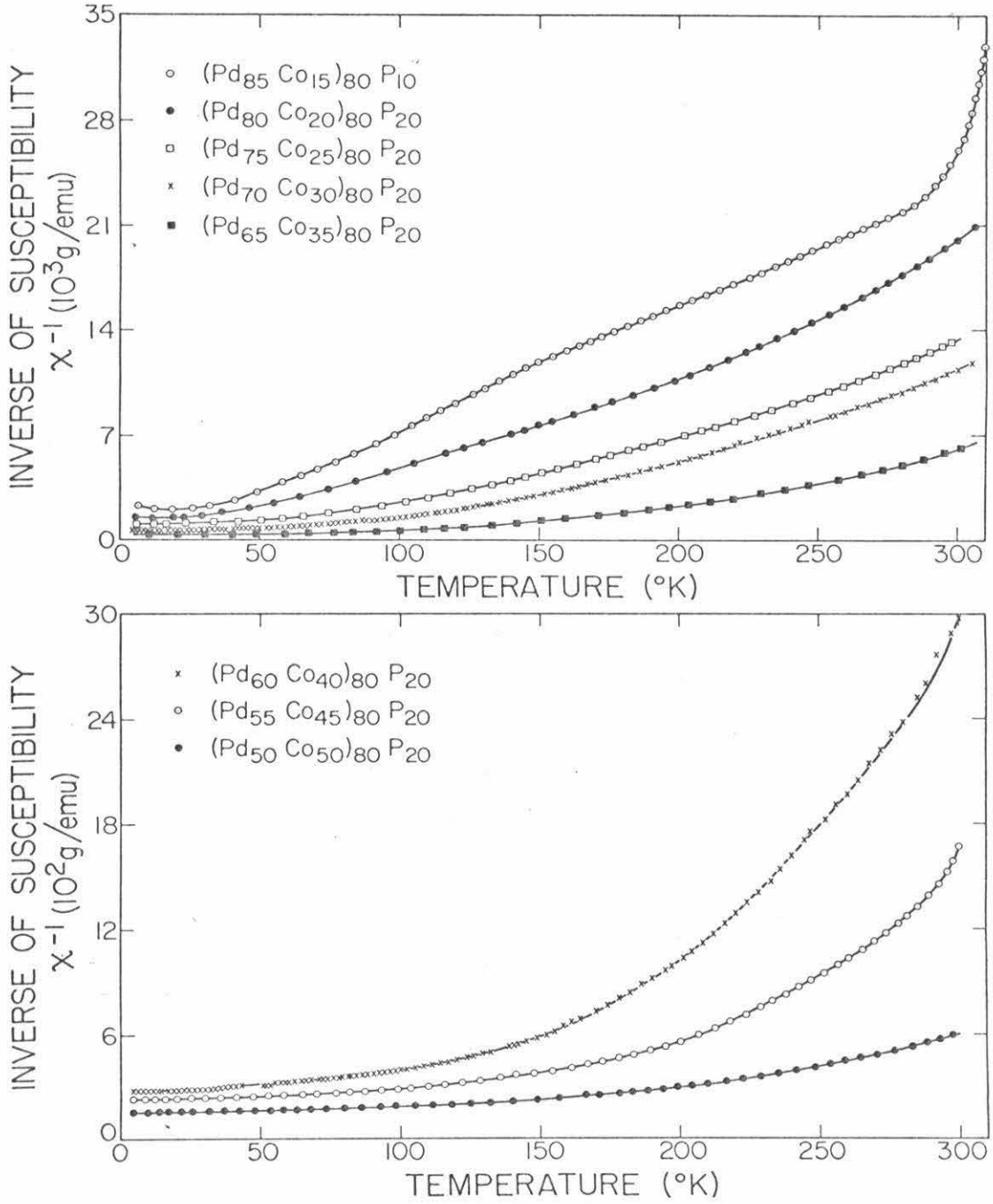

Fig. 45. Reciprocal susceptibility versus Temperature curves for $(Pd_{100-x}Co_x)_{80}P_{20}$ at an applied field of 6.0 kOe

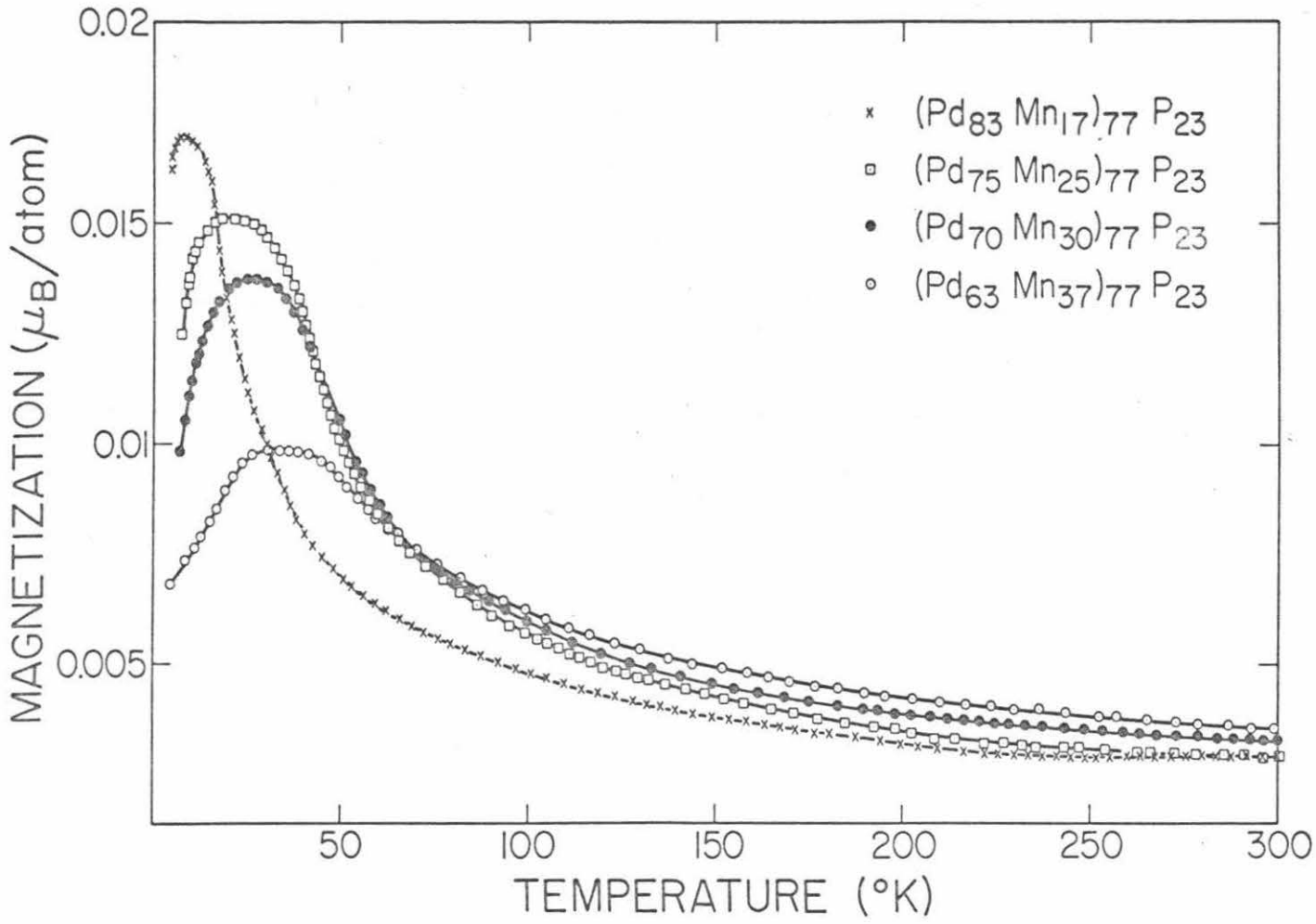

Fig. 46. Magnetic Moment versus Temperature curves for $(Pd_{100-x}Mn_x)_{77}P_{23}$ at an applied field of 6.0 kOe

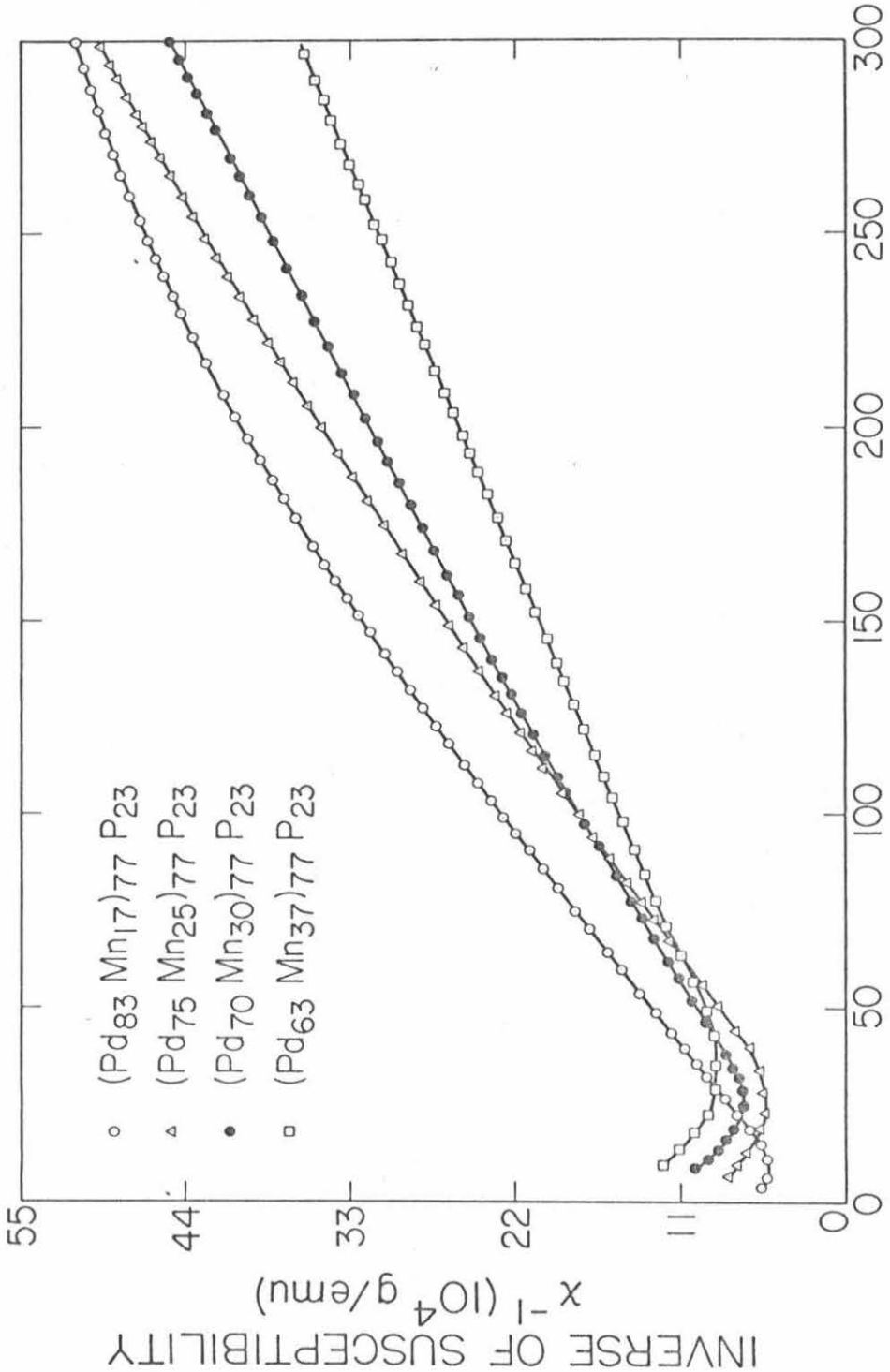

Fig. 47. Reciprocal susceptibility versus temperature curves for $(Pd_{100-x}Mn_x)_{77}P_{23}$ at an applied field of 6.0 kOe

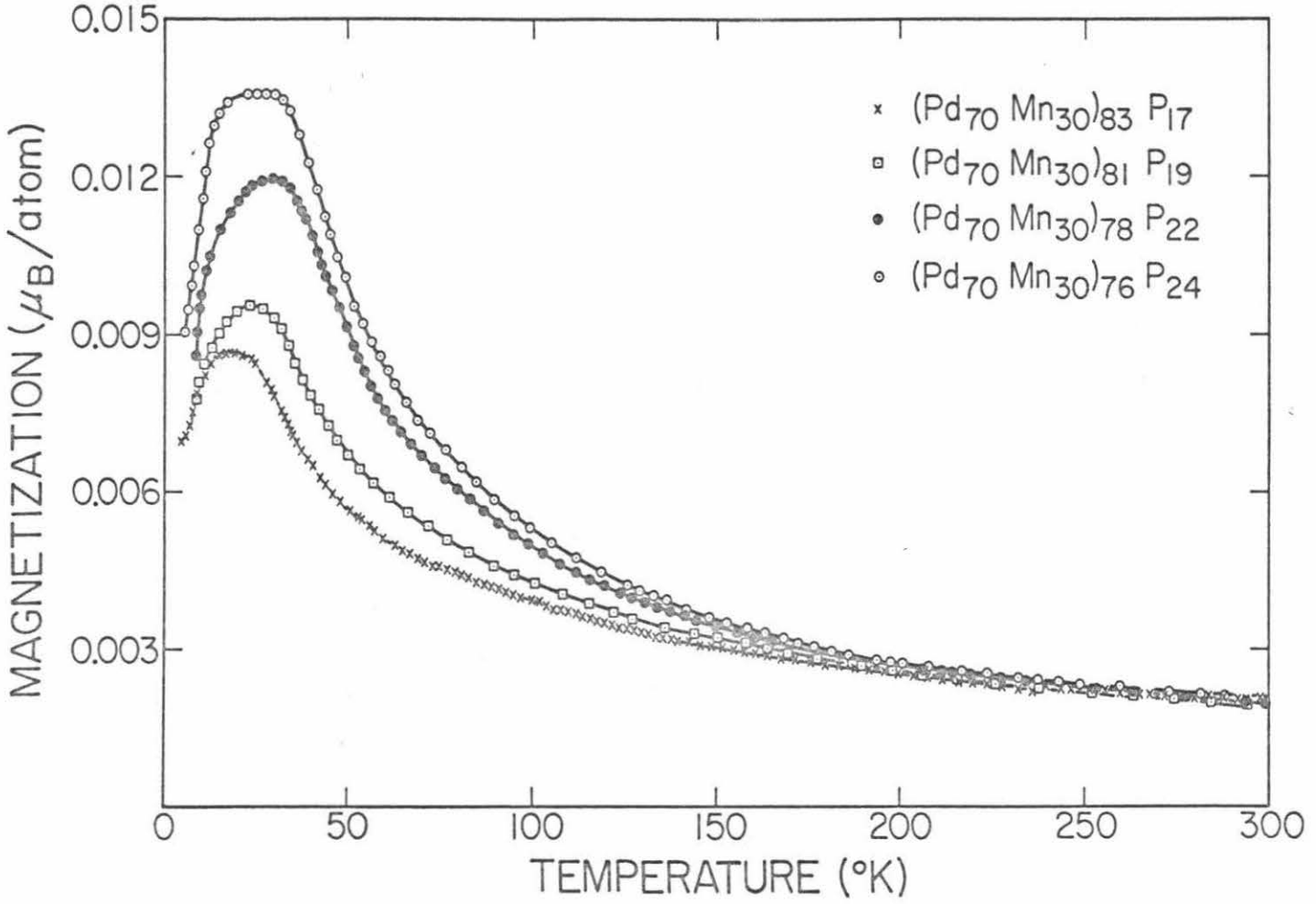

Fig. 48. Magnetic Moment versus Temperature curves for $(Pd_{70}Mn_{30})_{100-y}P_y$ at an applied field of 6.0 kOe

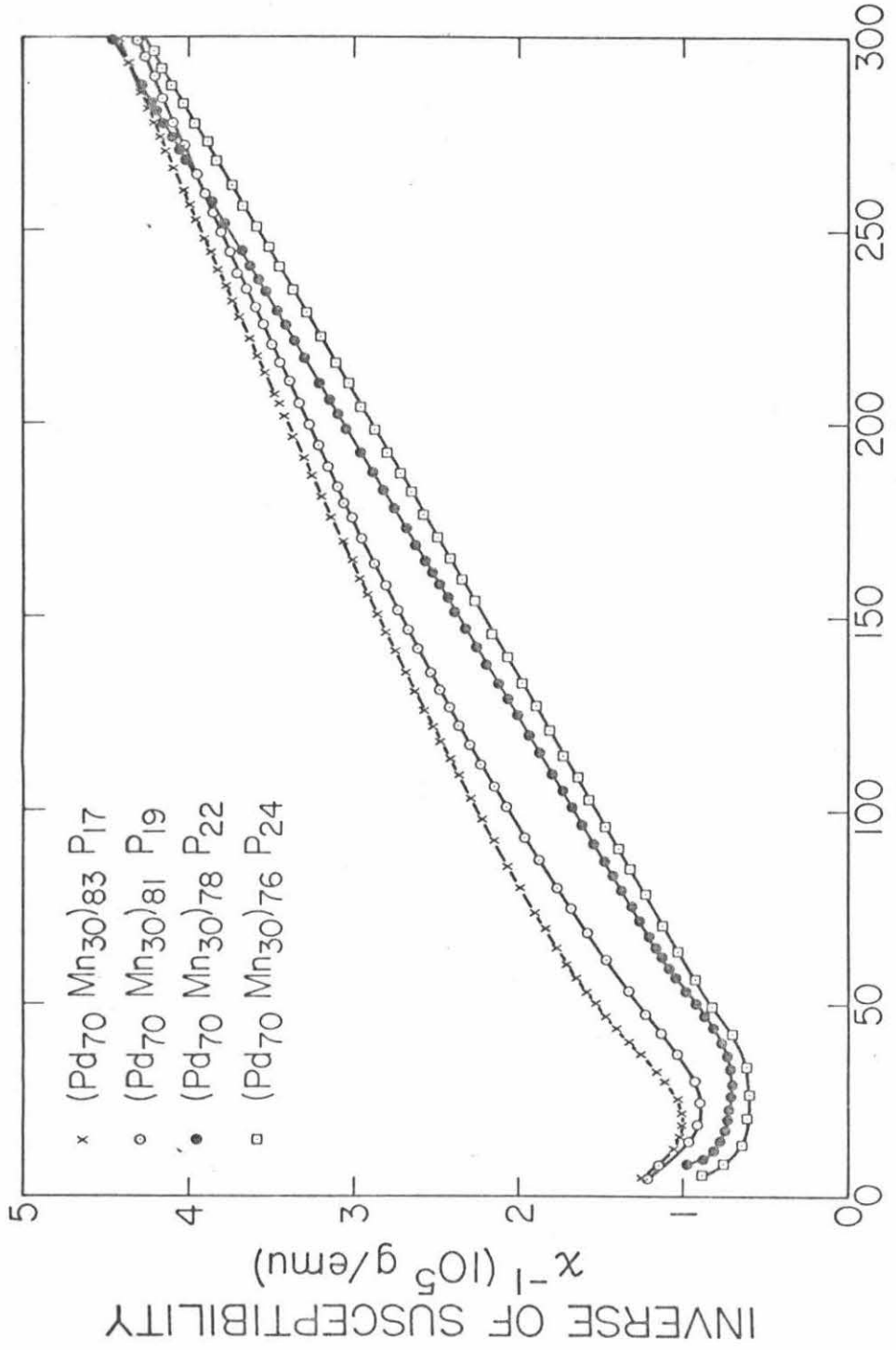

Fig. 49. Reciprocal Susceptibility versus Temperature curves for $(Pd_{70}Mn_{30})_{100-y}P_y$ at an applied field of 6.0 kOe

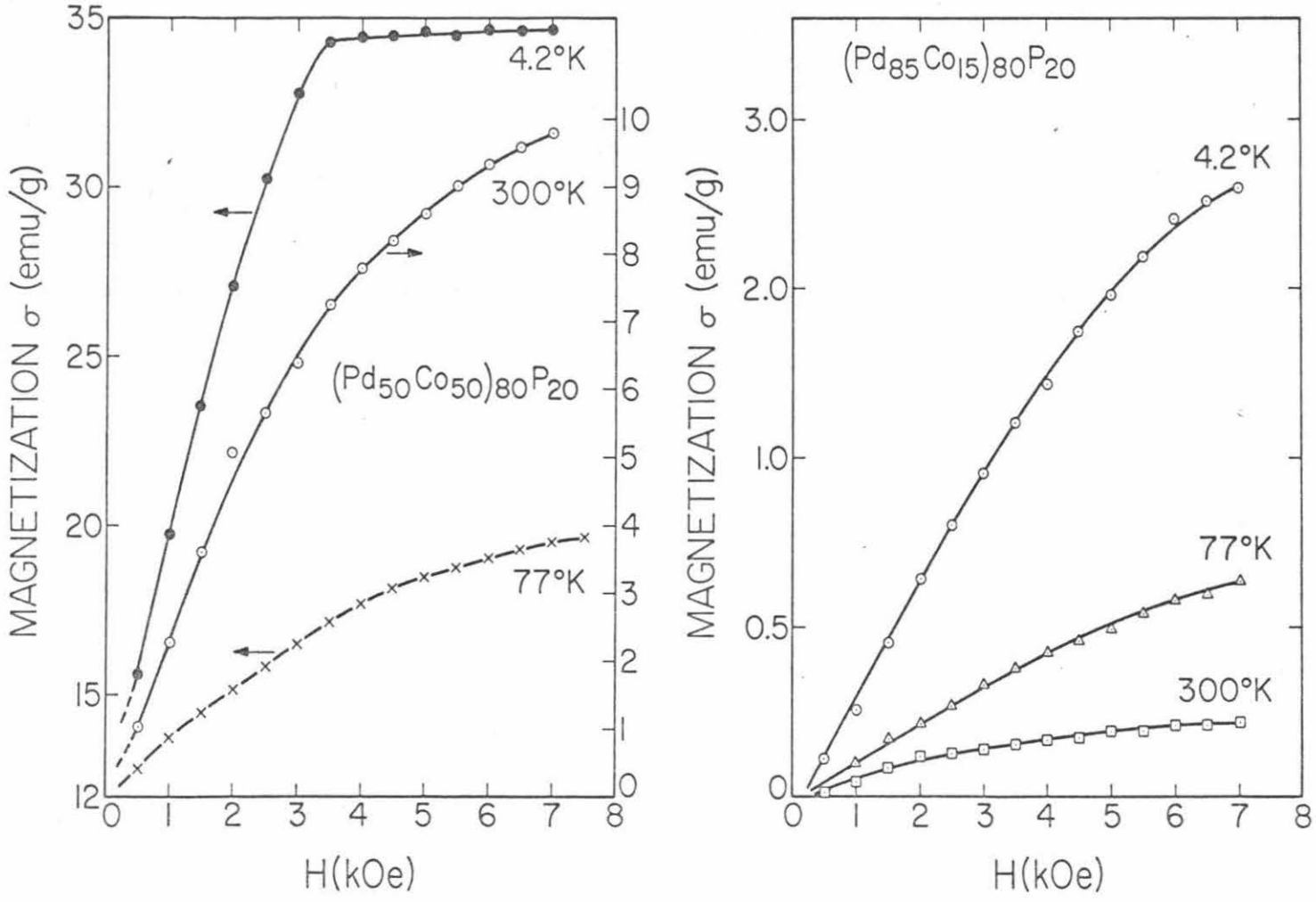

Fig. 50. Isothermal plots of magnetizations versus applied field for the two ends of the amorphous range in $(Pd_{100-x}Co_x)_{80}P_{20}$ alloys

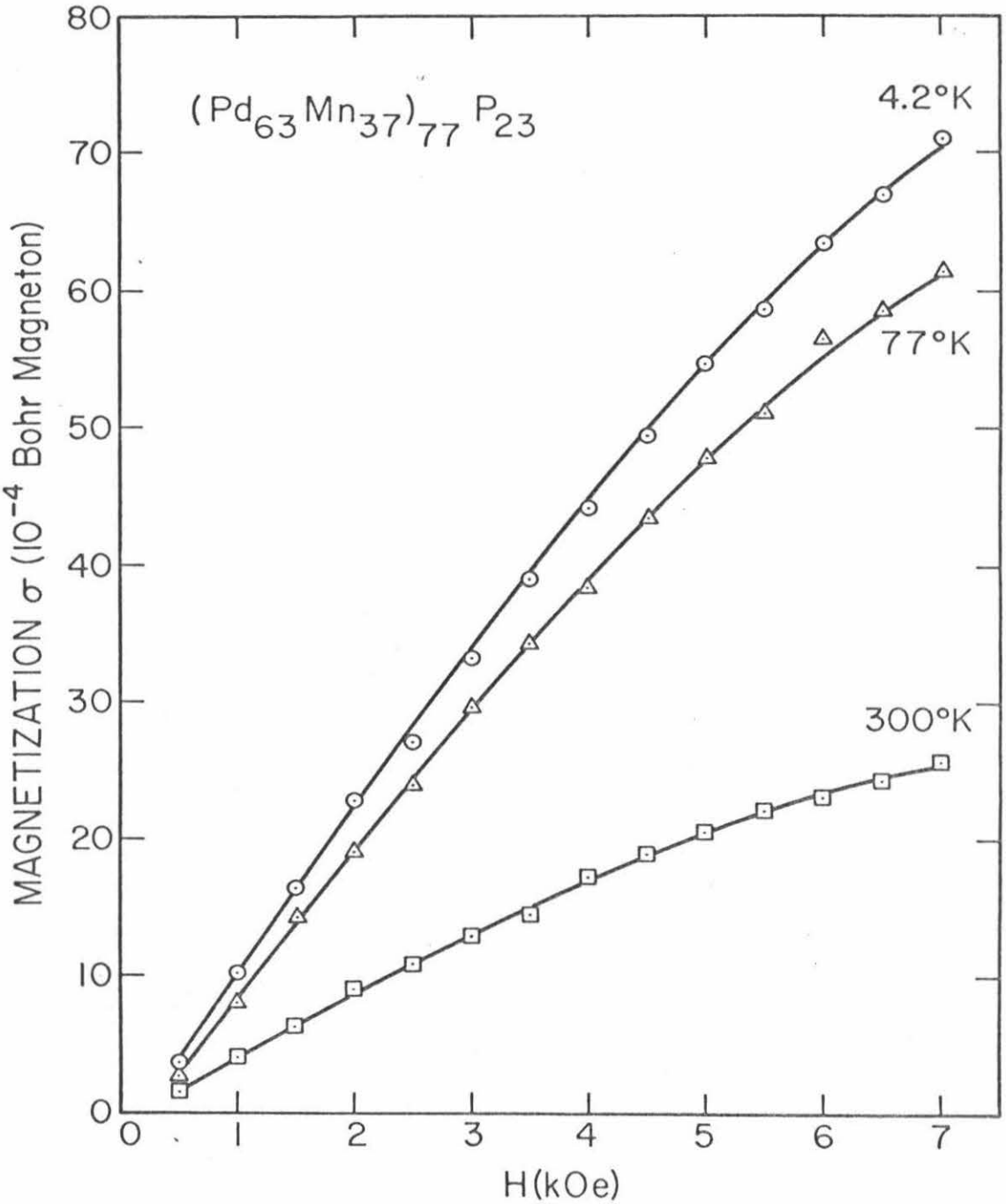

Fig. 51. Isothermal plots of magnetization versus applied field for the amorphous $(Pd_{63}Mn_{37})_{77}P_{23}$ alloys

the shape of the magnetization versus field is observed with varying either the manganese or phosphorus concentration. For a given temperature and a given field the magnetization increases with increase in phosphorus content and with increase manganese in $(Pd_{100-x}Mn_x)_{77}P_{23}$.

2. Magnetic Transition Temperature Determination

Since for Pd-Co-P the magnetic transition temperature is above room temperature for most of the alloys (of the series studied) as shown in Table XXII, a method based on an AC inductance coil which constituted one part of a Wheatstone inductance bridge with a lock-in amplifier as a null detector was used. The output signal of the lock-in amplifier was plotted on an x-y recorder against temperature.

The sample was cut into rectangular shapes, five or six in number, and holding among themselves a platinum-platinum rhodium thermocouple carefully calibrated against a standard thermocouple; they were spot welded for easy manipulation. As the temperature increased through the Curie point, the sample underwent a magnetic transition which caused an appreciable change in the sample coil inductance. A typical output signal for a sample of composition $(Pd_{60}Co_{40})_{80}P_{20}$ is shown in Fig. 52 and the Curie temperature versus cobalt concentration is plotted in Fig. 53.

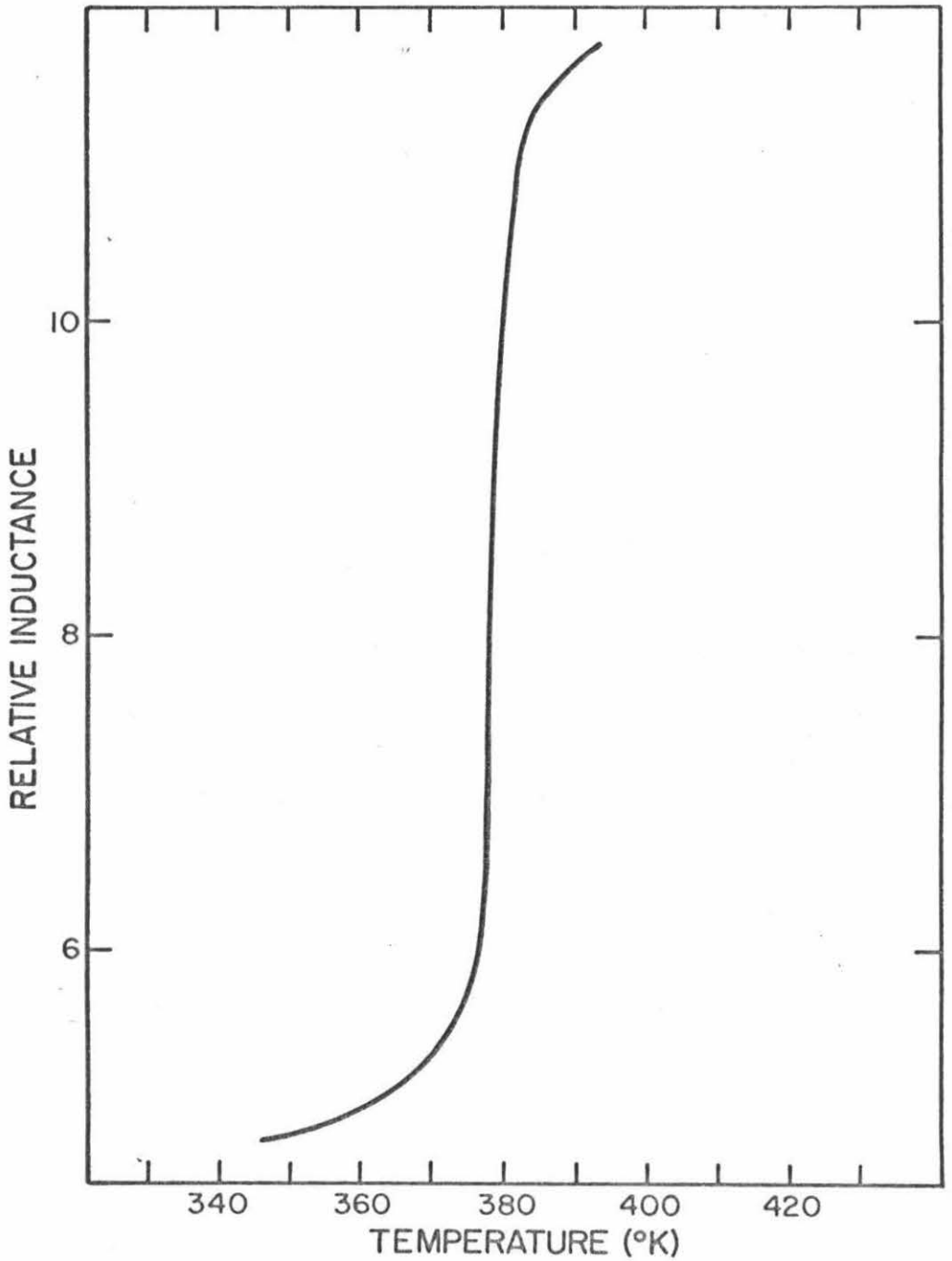

Fig. 52. Relative inductance versus temperature for amorphous $(Pd_{60}Co_{40})_{80}P_{20}$ sample

Table XXII. Curie Temperature for Pd-Co-P Amorphous Alloys

Composition	T_{Curie}
$(Pd_{50}Co_{50})P_{20}$	398 - 399 ^{o}K
$(Pd_{55}Co_{45})P_{20}$	381 - 383 ^{o}K
$(Pd_{60}Co_{40})P_{20}$	368 - 370 ^{o}K
$(Pd_{65}Co_{35})P_{20}$	354 - 356 ^{o}K
$(Pd_{70}Co_{30})P_{20}$	345 - 343 ^{o}K
$(Pd_{75}Co_{25})P_{20}$	329 - 330 ^{o}K
$(Pd_{80}Co_{20})P_{20}$	302 - 304 ^{o}K
$(Pd_{85}Co_{15})P_{20}$	272.50 ^{o}K

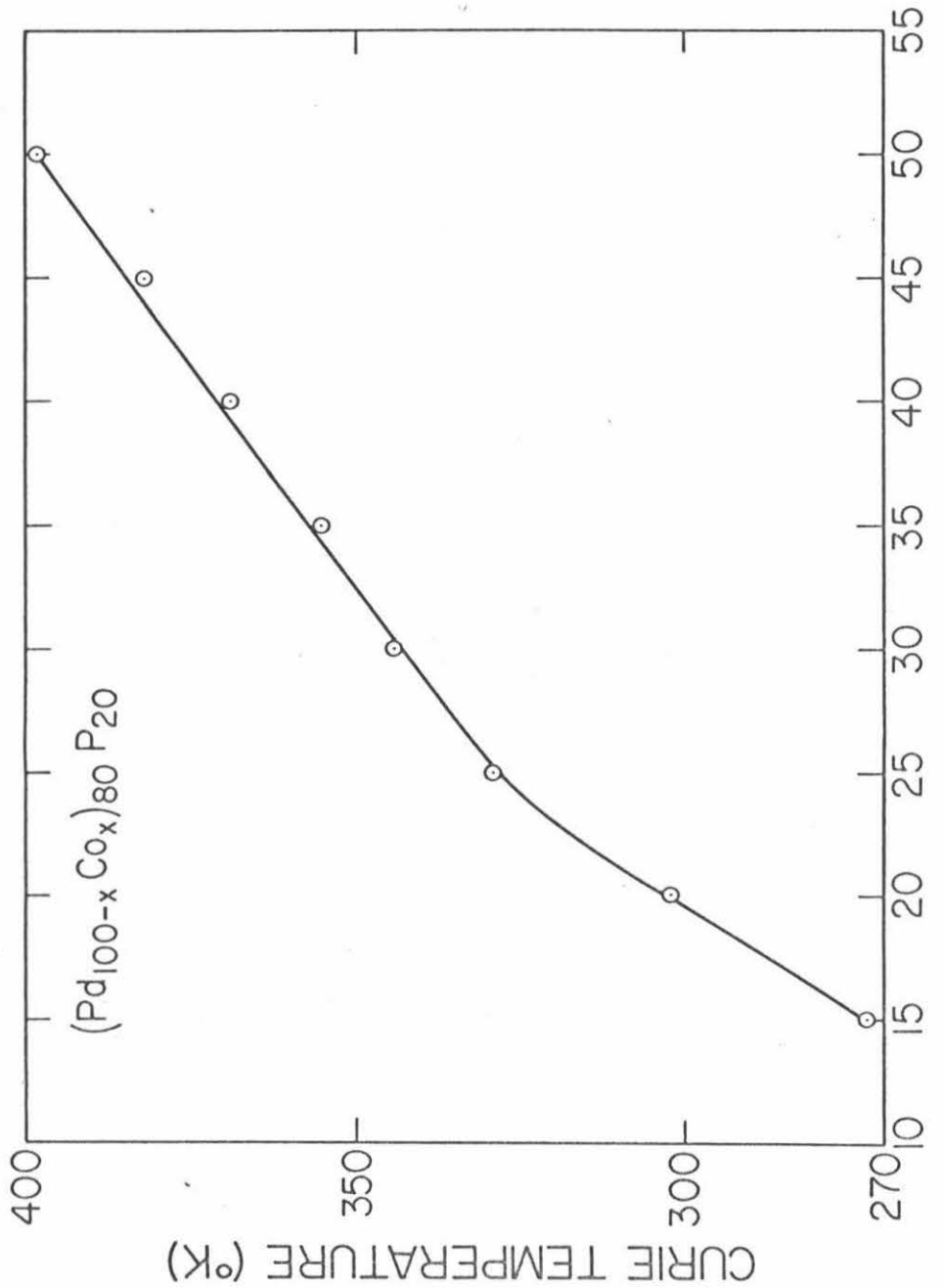

Fig. 53. Curie temperature versus cobalt concentration in $(Pd_{100-x}Co_x)_{80}P_{20}$

VII. DISCUSSION

A. Structure Investigation

It is shown that by reference to only the technique of x-ray diffraction measurements and electron microscopy analysis, precise information on the short range order governing amorphous metallic alloys could be obtained. Functions which convey quantitative information about the structure have been determined and compared with similar ones generated by computer simulated models. The experimental intensity data were processed using standard technique established in this laboratory[79].

Many attempts were made to describe the short range order existing in amorphous materials. A crystalline f.c.c. and h.c.p. was first proposed as a possible description[6]. Then a quasi-crystalline model based on the intermetallic compound Pd_4P gave better agreement for Pd-Ni-P and Pd-Fe-P[7]. The weakness of the quasi-crystalline model is in its structural validity, as it consists in applying a Gaussian broadening function to each peak to account for the mean-square displacements thus hiding and transforming many of the characteristics of the structure. Experimentally, the quasi-crystalline approach cannot explain the smooth varying functions with composition (i.e., density, nearest neighbors, apparent grain size, configurational entropy[80] and Gibbs free energy[81]). Two other approaches are left which come closer to a solution: the hard sphere model which favors the attractive potential between the spheres as a guiding criterion, and the repulsive potential favored by the Bernal model[9] packing structure.

Recent work by Finney[82] on the statistics of random packing showed that the structure of liquids can be characterized in terms of relatively simple geometrical entities and their statistical distribution. This "geometrical entities" model has the advantage that it accounts not only for the size and concentration of the constituents but also for the affinity among the atomic components. As noted by Sadoc[8], this structural "heap" of molecules has the advantage of taking into consideration the fact that the small spheres promote a special arrangement for the larger ones. These small spheres have more of an influence than just filling the holes of a random packing which neglects the directionality and length of the covalent bonding, which constitutes a reasonable percentage of the alloys. The "structural entities" model is in accord with Turnbull's suggestion[83] of a free-volume model for molecular transport in dense fluids and liquid-glass transitions. Accordingly, the atoms of manganese and palladium would preferentially surround the atoms of phosphorus to the extent of preventing the network of the matrix to form Pd-Pd, Mn-Mn or P-P clusters in Pd-Mn-P. Also Gargill[84] noted that the x-ray diffraction patterns of all amorphous metallic alloys are similar, confirming that the degree of short range order is of the same magnitude in all glassy alloys and no internal boundaries exist. The method of compilation of the atoms will influence the symmetry of the first peak as noticed by Finney and Bennett[82,85], as well as the shapes and intensities of the high angle peaks.

In the present alloys, the average value of the first coordination number is 12.6 atoms, indicating a dense packing of the

neighboring atoms. The density is high and of the order of 9 g/cm^3. The three-dimensional entity through which we might encode the coordinate data obtained by direct measurement could be a network of tetrahedra with sphere centers at every apex[86]. Finney[82] suggested that a "Voronoi polyhedron" model has advantages over the simple tetrahedral net as only one polyhedron is associated with each center. He could generate distribution functions structurally consistent with those obtained from liquids and glassy alloys, using Monte Carlo[87,81] methods on the basis of geometrical polyhedra. Supporting evidence for this model can be found in known theories (Brillouin[91], Shannon[92]) and configurational entropy evaluation[80].

1. Effect of Increase in Manganese Concentration in Amorphous $(Pd_{100-x}Mn_x)_{77}P_{23}$ Keeping the Phosphorus Content Constant

(a) As in previous alloys Pd-Ni-P and Pd-Fe-P, the position of the first peaks in I(K) and W(r) in Pd-Mn-P were related by the equation $K_1 \cdot r_1 \simeq 8.0$. The composition dependent rate of shift in the position of the first peak of the x-ray diffraction pattern is least accentuated in Mn, becoming increasingly noticeable as M changes from Mn to Fe to Ni. The higher value peaks do not follow a uniform trend with the transitional metal change nor with the increase in M concentration. The shift in the first peak to higher K values is much greater than the corresponding shifts for higher order peaks. In addition, the ratios of r_2/r_1 and r_3/r_1 , although tending to decrease with increase in M concentration, are far from being simple relations in terms of compositional size or concentration. There is

no straightforward correlation between the position parameters in the real (r) and Fourier (K) space of highly disordered structures, even though r_1 and $1/K_1$ are both linearly dependent functions of composition. The rate of change with Mn concentration might be explained in terms of the greater disorder in the Mn system, as the ratio of r_2/r_1 for Fe and Ni are respectively 1.66 and 1.65, while for Mn $r_2/r_1 = 1.82$ is much closer to the liquid metals in which $1.8 \leq r_2/r_1 \leq 2.0$.

(b) The intensity of the first peak in the interference function decreases, and its width, whose inverse can be regarded as a measure of the apparent grain size, increases. A comparison of the present results for Pd-Mn-P (grain size 14.33 to 12.1 Å) with those of Pd-Fe-P (grain size 14.3 to 13.3 Å) and Pd-Ni-P (grain size 12.4 to 11.8 Å) at the same range of transition metal content indicates no systematic trend of the grain size parameter with the size of the transitional metal content. This behavior can be better understood by looking at the transition metal and the metalloid, not in terms of hard inert spheres, but allowing for a variation of the interacting elements with chemical affinity as well as possible size variations with the change of the valence of the metal and metalloid.

(c) The average number of nearest neighbors tends to increase, which could be explained in terms of the fact that manganese, which is smaller than palladium, tends to enter much more easily into the domain of influence of the phosphorus. This is made possible by the wide range of valences available for manganese, and because the

chemical bonding between Mn and P is much stronger than between Mn and Pd, thus reducing the bond length.

(d) The density of the amorphous alloys decreases linearly with increase in manganese concentration, which is expected in view of the size effect. The crystalline density is higher than the amorphous one, which indicates the higher degree of disorder of the amorphous structure.

(e) To analyze the asymmetry in the first peak of the atomic distribution function, a symmetrical curve was traced by taking the mirror image of the left side with respect to the location of the maximum (Figs. 17 and 18, dashed line). The difference between this curve and the experimental one was plotted and is represented by the dotted line. It is generally accepted that the peak in the symmetrical curve reflects the metal-to-metal nearest neighbor distances, while the asymmetrical component of the first peak in the atomic distribution function has received various explanations[79,93]. In Pd-Fe-P and Pd-Ni-P[7], the shoulder is on the right hand side of the first peak, while in Pd-Mn-P, the shoulder is on the left hand side of the maximum. The interesting splitting of the first peak was also found in the network of polyhedron by Finney[82] and was reported as a broadening by Mason[94,11]. The Voronoi polyhedron finer histogram revealed a splitting of the first peak into three parts, and a tentative geometrical interpretation of these peaks in terms of the characteristic features of the sphere arrangements was proposed[82]. It was suggested that the shoulder at the high angle side of the peak

corresponds to the existence of three-membered collineation as originally noted by Bernal[95] in earlier studied models. A slight departure of the collineation angle from π would tend to depress this shoulder. The two other peaks (short distance and high maxima) involve more complex geometrical entities. Bernal shows that the high intensity peak might be due to high frequency occurrence of tetrahedra in random arrays[95]. Finney[82] suggests that the low angle peak may be due to two tetrahedra having a common base (an element of pseudonucleus growth) and opposite apexes separated by a certain distance.

(f) Contrary to what was observed in Pd-Fe-P and Pd-Ni-P amorphous metallic alloys, there is no shoulder on the high angle side of the second peak of I(K), and the atomic distribution function does not have a double peak beyond the first maximum. Similar behavior was observed in Ni-Pt-P[39]. The splitting of the second peak was interpreted by Sadoc[8] in terms of atomic size and/or concentration effects, but Gargill[96] showed that hard equal-size spheres can give rise to second peak splitting. Woodcock[98] advanced a totally new approach for the understanding of liquid structure. According to his approach, the atomic distribution function of Pd-Mn-P could be pictured in terms of its resolved components: (i) unlike atom pair distribution function $W_u(r)$; (ii) like atom pair distribution function $W_\ell(r)$; and (iii) a covariance function between like and unlike atom occupation numbers $W_{u\ell}(r)$. The first peak of the unlike atom pair distribution function is high in intensity and narrow in width. It represents the tendency to form clusters and occurs at shorter range order (smaller r). The

like atom pair distribution representing the energetically repulsive encounters between ions occurs at higher "r", and the first peak in $W_\ell(r)$ is broad and diffuse compared to $W_u(r)$. Finally, damped oscillations depending on the ratio and positions of $W_\ell(r)$ and $W_u(r)$ show the degree of long range order existing. It is interesting to notice here that the "resolved pair distribution function" model would agree with the "Voronoi polyhedron" model in interpreting the shoulder on the low angle side of the first peak as due to shorter range order elements. Another confirmation of this interpretation can be deduced from the fact that the right hand shoulder is associated generally with r_2/r_1 of the order of 1.65, while the left hand shoulder is found in liquid copper[93] and gold and amorphous alloys like Pd-Mn-P, whose r_2/r_1 ratio is approximately 1.82 which is much closer to liquid metals in which $1.8 \leq r_2/r_1 \leq 2.0$. Judging from studies of attractive and repulsive pairs, the splitting of the second peak might be the result of a strong repulsion between the like pairs[97,98].

(g) The direct correlation function $C(r)$ is obtained solely from the radial distribution data. For insulators, $C(r)$ has no nodes, whereas for metals and ionic liquids, it has marked oscillations[47]. This suggests that $C(r)$ is closely connected with the pair interaction $\Phi(r)$. By analysis of the equations of the Born-Green, Percus-Yevick and hyperchain methods, it can be shown that they all yield $C(r) = -\Phi(r)/kT$ for sufficiently large r . It is implied, therefore, that this is a general result, and does not depend on approximate theories. The long-range oscillations could be interpreted as

reflecting the magnitude of conduction electron screening of the ions and present striking evidence that, even in liquid metals where the mean free path is short, the Fermi surface is quite sharp. Some evidence of the damping of the oscillations is found and it could be used to determine a rough value for the blurring of the Fermi distribution.

2. Effect of Increase in Phosphorus Concentration on Amorphous $(Pd_{70}Mn_{30})_{100-y}P_y$ Keeping the Metal Content Constant

(a) The effect of increasing phosphorus concentration is illustrated by a decrease in the intensity of the first peak, a broadening of the first several peaks, and a decrease of short range order reflected by a decrease of the number of intensity maxima. It might be significant to note that the wiggles present on the second peak seem to disappear above 20 at.% phosphorus, as well as a general tendency for the higher interatomic distance peaks to damp much faster and broaden as we increase the P content. The information contained at the high angle maxima of the atomic distribution function was made possible by the use of a very small damping factor which directly affects the short-range order and by extra care in eliminating the possible sources of parasite functions.

(b) The metal-to-metal distance increases slightly with the increase in phosphorus content which indicates, as expected, that the phosphorus does not go interstitially into the amorphous structure, but plays an important role by making the structural bonding more rigid, which gives rise to a larger metal-to-metal interatomic

distance and thus increases the local disorder in the alloy. The position of the shoulder on the high angular side of the atomic distribution function increases with the increase in phosphorus content up to 23 at.% and then decreases. The increase could be interpreted in terms of an increase in the formation of three-membered collineation entities.

(c) The number of maxima at higher interatomic distance which gives an insight on the short range order decreases from 7 to 6 in the range studied. The rate of damping of those maxima increases while they become wider and flatter approaching a perfect liquid-like structure. This loss of long-range structure periodicity and the smearing out of the diffraction pattern could be attributed to one or more of the following factors: (1) smaller crystalline size; (2) higher density of deformation type stacking faults; (3) higher internal strains and (4) a higher like-atoms repulsion distribution function. It was demonstrated[84] rather satisfactorily that the above mentioned effect cannot be due only to small crystallite size whose effect on calculated interference functions was mainly to broaden the peaks. There is no reason to believe that arguments (2) and (3) would be effective with change in phosphorus content and not with change in manganese concentration. Therefore, it is more plausible that the phosphorus increases the pair repulsion effect among the atoms, thus creating voids which are confirmed by the trend in the density and coordination number valences.

(d) The other factors fall within the comments made on the varied manganese concentrations.

In summary, the structure of amorphous alloys could be described quite satisfactorily in terms of "Voronoi polyhedron molecular entities". As the density increases, the following progressive development occurs until close packed structure is attained: (1) an inward movement of all peaks and minima toward lower "r", (2) rapid sharpening of the high angular side of the second peak and the incipient condensation of the left hand side of the first peak into a shoulder and eventually into a δ function. The existence of this δ function peak is a result of two hard-bonded equilateral triangles sharing a common side[89].

B. Electrical Resistivity

The phenomena governing the transport properties in crystalline alloys are well investigated by now, but there is still work to be done in the field of amorphous systems. Generally, these rapidly quenched alloys are of the formula Pd-M-G or Pt-M-G, where M is Cu, Ni, Co, Fe, Mn or Cr, and G is a glass former B, Si, C or P. These alloys have all the characteristics of metals except that they have a large residual resistivity of about 0.5 to $4 \times 10^{-4} \Omega$ cm. In all alloys a Kondo type resistivity dependence was observed at low temperature. It is of interest to notice that in general, at a constant phosphorus content of 20 at.%, all transition metals having more than half-filled valence shells give rise to a positive coefficient of resistivity, while Cr ($3d^5 4s^1$), Mn ($3d^5 4s^2$) and Cu ($3d^{10} 4s^1$) which have a stable

"d" shell configuration give rise to a negative coefficient of resistivity. A particular aim of this work is to interpret the experimental results in Pd-M-G in terms of the concept of localization of electron states as well as the width of the band energy which was derived by Anderson[52] and later developed by Mott[99]. Although the interpretation could be applied to a large variation of amorphous alloys containing a transition metal and a glass former, in this text all discussions are restricted to Pd-Mn-P as a type of negative temperature dependence and Pd-Co-P as a type of positive coefficient of resistivity.

1. Pd-Co-P Alloy System

The absolute value of the resistivity and its temperature dependence point out the metallic conductivity of the amorphous Pd-Co-P. Their resistivity at room temperature is three times that of the crystalline alloys obtained by annealing the samples for two weeks at 600°C. This result is ascribed to the high degree of disorder which characterizes the amorphous structure. The values obtained for the resistivity of the amorphous alloys at room temperature range from 143 to 298 μΩ-cm. The dispersion of values is too large to show clearly the influence of composition. The order of magnitude of the resistivity is the same as previously reported in amorphous Pd-Ni-P and Pd-Fe-P and no trend is easily detectable in terms of the kind of transition metals in the alloy.

Like all other Pd-M-P, the presence of M = "3d", transition metal dissolved into the amorphous media, tends to polarize the surrounding atoms via conduction electrons. Spin polarization of this

sort has been observed in magnetic susceptibility, electrical resistivity, specific heat, Mössbauer effect, neutron scattering, NMR and EPR measurements[100]. In addition, the range of the spin polarization around the magnetic atom has been shown to vary drastically with concentration. As shown in Section IV-C.1, the total resistivity below approximately 130°K can be fitted to a relation of the type:

$$\rho(T) = \rho_o + \beta T^2 - \alpha \ln T - \Delta\rho_o \qquad (36)$$

with ρ_o, $\Delta\rho_o$, α and β being parameters depending on the composition and the structure of the amorphous alloys. These parameters were determined by plotting $\rho(T)$ versus T^2 to obtain ρ_o and β and then by plotting $R_{spin}(T) = \rho(T) - \rho_o - \beta T^2$ versus $\ln T$. The resulting parameters are listed in Table XV and a sample of those plots is shown in Figs. 27 and 28. From magnetic measurements (Sec. VI) the samples are shown to be ferromagnetic with a Curie temperature between 272°K and 398°K. Magnetoresistivity measurements (Sec. V) show the coexistence of ferromagnetism with paramagnetic ions. The βT^2 term is due to s-d interaction, and in the ferromagnetic atomically disordered alloys, the $\alpha \ln T$ term eventually becomes much larger than βT^2 and dominates the behavior of the resistivity leading to a minimum in the ρ-T curve. This is qualitatively analogous to the resistivity minima encountered in very dilute paramagnetic alloys like CuMn[10] (a few ppm of Mn) known as Kondo[17] alloys. In Pd-Co-P the problem is quite different, as instead of a very dilute paramagnetic alloy, one is faced with concentrated ferromagnetic alloys and the structure is disordered.

The explanation of the ($-\alpha$ ℓn T) term in equation (36) is a Kondo-type effect due to the state of spin ordering of the free paramagnetic ions. The resistivity of Pd-Co-P can be interpreted in terms of spin order-disorder phenomena in ferromagnetic alloys which was studied by several authors: Kasuya[14], van Peski-Tinbergen and Dekker[101], and De Gennes and Friedel[102]. Below the Curie temperature T_c the spin is generally ordered except for a few paramagnetic ions. Above T_c the alloy is paramagnetic and there only subsists a small local spin ordering due to the molecular field σ_{loc} of the nearest neighbors of each spin[102]. This leads to an increase of the resistivity ρ, aside from the phonon part due to spin-disordered contributions. Here the logarithmic variation of resistivity with temperature was observed down to $4.2^{o}K$ in all Pd-Co-P alloys as shown in Fig. 28, and this tends to imply a low Kondo temperature of about $T_K < 4^{o}K$. In dilute Kondo-type phenomena found in very dilute Fe in gold and Fe in copper, Kondo theory predicts that the depth of the minimum ($\rho_{max}-\rho_{min}$) is proportional to the concentration "x" and that the observed minimum T_{min} would vary in crystalline alloys as $x^{1/5}$. In amorphous alloys the temperature dependence resistivity term varies as T^2, which would result in T_{min} being proportional to $x^{1/2}$. On the other hand, the "pair model" introduced by Dekker[103], Brailsford and Overhauser[104] was found in agreement with recent work of Beal[105], who introduced the long-range RKY indirect exchange interaction between the localized moments explicitly. He found[105] that T_{min} is proportional to $x^{1/3}$ and $(\rho_{max}-\rho_{min})/\rho_{min}$ are independent of the concentration in crystalline alloys.

In Pd-Co-P the resistivity minimum decreases linearly as the Co concentration increases. The quantity $(\rho_{max}-\rho_{min})/\rho_{min}$ is proportional to the concentration (Table XIV) and decreases from 8 to 2% as the concentration of Co increases from 15 to 50 at.%, which indicates that the minimum is due to a correlation between independent localized spins.

The present result could therefore be attributed to the presence of paramagnetic ions in the ferromagnetically ordered alloys. The coexistence of a resistivity minimum phenomenon with ferromagnetism in disordered alloys may be associated with the facts that (1) d-d spin interaction is about 5-% weaker in the amorphous alloys than in the corresponding crystalline phase, and (2) extremely small concentrations of magnetic impurities are sufficient to yield a measurable Kondo effect. Therefore, due to uneven randomness and differences in the degree of short range order in the amorphous structure, a certain infinitely small number of transition metal atoms might find themselves shielded from all other transition metal atoms to behave like free spins. These localized "d" spins interact with the "s" conduction electron spins antiferromagnetically to give rise to the negative exchange integral "J". Moreover, the concentration of these localized moments is probably different from the overall "3d" transition metal concentration and also from one sample to another, which explains why the T_{min} is sometimes different as much as 6 ^{o}K from specimen to specimen cut within the same foil (Table XIV). The problem of interactions between impurities in a random alloy has been treated by

Marshall[106] and Klein[107] in terms of a probability distribution of internal fields (the value of these fields can be described by a continuous probability distribution function). Klein also found that the concentration dependence of the temperature of the resistance minimum depended on the form used for the distribution of these internal fields[108]. This explains the observed increase in T_{min} from 22 to 56 ^{o}K with decrease in Co concentration from 50 to 30 at.%, as the probability of finding a free spin increases with decreasing concentration. The almost constant behavior of T_{min} from 25 to 15 at.% cobalt might be interpreted in terms of an independent probability function due to a weak d-d exchange interaction at sufficient dilution. It is of interest to note that the Kondo minima are observed at low temperatures (almost the same temperature range in all Pd-M-P alloys) in order not to be smeared out by the phonon effect and because the scattering is low enough to prevent the ordering of the paramagnetic ions.

At temperatures above T_{min} the T^2 term is the dominant contribution to the resistivity until 77 to 118^{o}K where an almost linear variation with temperature is reached. The variation of the resistivity as T^2 can be explained in terms of the band structure of the Pd-M-P where 80 at.% are transition elements. The electron-electron interactions in the transition metals contribute substantially to the resistivity at low temperatures through collisions between the "s" electrons of the conduction band and the "d" electrons which are mainly localized (Section IV-B.1). Such s-d electron-electron interactions contribute a T^2 term in addition to the other factors[10]

which might also contribute a T^2 term like electron-paramagnon interactions. The decrease of α and β with increase in cobalt content is due to the increase in the interacting localized spin in terms of an increased internal field as seen elsewhere[109,110]. From equation (36) it can be derived that $T_{min} = (-\alpha/2\beta)^{1/2}$, which is conveniently called ($T_{min\ calculated}$). It is apparent (Table XV) that the experimentally observed minimum falls quite close to the calculated T_{min} values, which indicates a reasonably good fit of the phenomenological equation.

In Pd-Co-P the resistivity increases approximately linearly with temperature within the range 130° to 200°K, with an average slope of 10^{-2} μΩ cm/°K which is of the order of one-tenth that of the same crystalline phase. This small temperature coefficient of resistivity can be attributed to the large disorder of the amorphous structure, which makes the contribution of phonon scattering quite small. Above 200°K the resistivity tends to flatten toward the temperature axis. In this temperature range the transport properties are governed mainly by thermal excitations from the localized electron states to the conduction band. Eventually at high enough temperatures all the electrons have been excited to the conduction band which causes the flattening of the resistivity curve. To confirm this, the slope of the resistivity curve $(\rho_{300}-\rho_{200})/\Delta T$ was calculated as a common denominator range for all the alloys of this series (Table XIV). In Pd-Co-P, since the "d" band is nearly filled by electron transfer from phosphorus, there is probably only between 0.5 and 1 "s" conduction electron per atom, which would explain the small positive

coefficient of temperature observed for the resistifity.

In summary, we expect a resistivity minimum to occur in ferromagnetically, atomically disordered alloys, the minimum becoming less important as the transition metal concentration increases and the coefficients of $\ell n\ T$ and T^2 become smaller and strongly temperature dependent. The spin ordering in these kinds of alloys can be simulated as the ordering due to an applied "external field" or as an increase in "internal fields", due to an increase in transition metal concentration.

2. Palladium-Manganese-Phosphorus Alloys

The amorphous structure is particularly conducive to the existence of localized moments[52], especially in the presence of magnetic transition elements. These localized moments on Mn and the resulting s-d exchange interaction between the conduction electrons and the free paramagnetic ions[111] are manifested by an enhancement of the negative temperature dependence of resistivity at lower temperatures. A resistivity minimum, of course, would not be expected, as the base alloy already has a negative temperature coefficient of resistivity. In addition to the negative temperature dependence, these alloys show T^2 behavior at the lowest temperature range, $\ell n\ T$ at low temperatures, and an almost linear behavior at high temperatures. Chandrasekhar and Huhn[59] attempted to explain the negative temperature coefficient in γ phase uranium molybdenum alloys in terms of a "two overlapping bands model", of which one is narrow (Sec. IV-B.3). The result of their work is summarized by equation (31) which predicts that $\rho(T)$ is proportional to T^2 at low temperatures. Sinha[67] using Ziman's approach[63] suggested that the negative coefficient of $(Pt_{100-x}Ni_x)_{75}P_{25}$

($20 \leq x \leq 50$) is due to their high Fermi energy 6.9 eV, which corresponds to the position of the first peak in the x-ray interference function. But according to Friedel[10] the Fermi energy should be smaller than the reported value for the localized moments to exist. Earlier work[112] explained the T^2 behavior at low temperature by "Nagaoka spin compensated states" acting at lowest temperature range and a Kondo mechanism acting at a higher temperature range. Here by reference to the "localized spin fluctuation model"[69] (LSF), the negative temperature coefficient of resistivity, the T^2 behavior, and the $\ell n\ T$ will be explained and the transition to T dependence of the resistivity will be predicted.

Use of the LSF was first proposed by Lederer and Mills[113], who showed that the scattering of conduction electrons from time-dependent fluctuations of the magnetization at the site of a nearly magnetic transition metal "impurity" leads to a resistivity varying as T^2 at sufficiently low temperatures, as observed in dilute Pd-Ni alloys[114]. Babic et al[115], interpreted the decrease of the resistivity with increased temperature in MnAl, and Caplin[116] in CrAl, in terms of localized spin fluctuations. The mechanism by which the LSF operates is that the virtual bound state forces the phase shift to go to $\pi/2$ at zero temperature, so that the additional scattering due to spin fluctuations has the effect of pushing the scattering off resonance and hence reduces the resistivity as T increases.

The question then follows as to why the resistivity coefficient is negative in Pd-Mn-P and not in other Pd-M-P alloys where M = Co, Fe, and Ni? The explanation is possible in terms of many of the existing

theories:

(1) From Anderson's virtual bound state model[52], it is apparent that the enhancement of the negative contribution to the resistivity will be maximum when the virtual bound state is half full, $E_d = 0$ in equation (33). In Al, as expected, this occurs between Cr and Mn and is confirmed by susceptibility[119], residual resistivity, and thermopower measurements[125].

(2) Recent work by Cyrot[130] on amorphous alloys revealed that the shape of the d band is not changed in comparison to that of the crystalline case, except that the width is reduced by a factor $\sqrt{1-c}$ where c is the concentration of sites inaccessible to electrons when the atomic levels are infinite. This should make the off-resonance scattering easier. Preliminary results of Pd-Cr-P and Pd-Cu-P confirm the expected negative temperature dependence for these alloys.

Kaiser and Doniach[69] suggest that for LSF the resistivity behavior is of the form:

$$\rho(T) = \rho_o[1 - \tfrac{1}{3}\pi(T/T_{LSR})^2]$$

at low temperatures and

$$\rho(T) = \rho_o[1 - \tfrac{1}{2}\pi(T/T_{LSF})] \qquad (43)$$

at temperatures above $0.2\ T_{LSF}$.

Nagaoka's condensed state[18], on the other hand, predicts the behavior:

$$\rho(T) = \rho_o[1 - (T/T_K)^2] \qquad (44)$$

So although experimentalists and theorists agree on how the measurable quantities should behave as a function of temperature, the difference is in the mechanism and in the value of T_K and T_{LSF}, which results from the weighing factors in the relevant physical expressions[68]. Rivier[70], applying Anderson's electronic contribution equation to the transport properties (Ref. 11, equations (9)-(13)), demonstrated a physical equivalence between the Kondo-Nagaoka spin compensated state and LSF in a dilute alloy, nonmagnetic in the sense of Friedel[61] and Anderson[52], but where LSFs are important[21] at low temperatures ($kT << \tau_o^{-1}$) where τ_o is the lifetime of the LSF. Such a description includes both a conjecture by Schrieffer[58] that some dilute alloys (like transition metal in Al), traditionally viewed as nonmagnetic, are in fact Kondo compensated magnetic impurities, and Anderson's view[52] of the Kondo temperature as the boundary between the nonmagnetic and magnetic behavior in dilute alloys.

Mathematically, the spin compensated state and the LSF are not equivalent (Sec. IV-B.3), since the former is a magnetic state, while the latter is nonmagnetic. Physically, however, their effect on observed quantities like the transport coefficients or the susceptibility is the same. Conceptually, it is much easier to visualize a nonmagnetic alloy with spin fluctuations appearing magnetic at high temperatures ($1/\chi$ versus T) than with condensation at low temperatures of a magnetic impurity surrounded by conduction electrons.

The resistivity minimum and the $\ell n\ T$ behavior in the LSF model was explained by Levine[109] in terms of Wolff's model[110] of local-moment formation in dilute alloys using the self-regulating solution

of Suhl[117] and Levine and Suhl[118]. Their results show that within the framework of their theory[118], the resistivity due to the free paramagnetic ion exhibits a Kondo-like behavior approximating $\ell n\ T$ over an appreciable temperature range[61,71,19,119].

For amorphous alloys the phonon contribution to the resistivity behaves also as T^2 at low temperatures. No attempts will be made to separate the $\rho_{(phonon)}$ from $\rho_{(spin\ fluctuation)}$.

The experimental resistivity curves (Figs. 29 and 32) could be fitted to the phenomenological equation (38):

$$\rho = \rho_o - (\alpha + \beta(\frac{T}{\theta})^2 - \gamma\ \ell n\ T + \varepsilon T) \qquad (38)$$

There is a Kondo-like region in the temperature range $T_d < \rho \alpha \ell n\ T < T_d'$ as shown in Figs. 30 and 33. The existence of a $(-\gamma\ \ell n\ T)$ term indicates a Kondo-type effect due to the state of spin ordering of the free paramagnetic manganese ions. Although in the crystalline alloys so far studied the Kondo effect disappears in the magnetically ordered alloys, this does not seem to be the case in amorphous systems where the coexistence of the Kondo effect with magnetic order was observed frequently[120,121] and could be explained by the existence of a small amount of random paramagnetic ions in the alloys. These ions are relatively free from each other, since the resistivity data between T_d and T_d' could be explained without taking into account the terms arising from the mutual interaction between those free spins. This effect is probably linked with a small d-d interaction in the amorphous alloys. The leveling off of the resistivity below T_d in the $\ell n\ T$ plot is probably due to the internal

field arising from the magnetic ordering of the free ions and the presence of LSF in the nearly magnetic bound states formed on those paramagnetic Mn spins. As the temperature is lowered, the number of free spins diminishes and finally the LSF, T^2 term dominates the resistivity behavior. This lower portion of the resistivity curve was computer fitted to the LSF low temperature equation (43) and to the Nagaoka expression for compensated state, equation (44).

It is worth noticing that the concentration dependence of T_K is very close to that of T_d' (Tables XVI and XVIII), which indicates that they are similar. Experimentally $T_d' \simeq T_K$ increases linearly with Mn concentration "x" while theoretically T_d' should be proportional to $x^{1/2}$, due to the fact that the temperature dependence resistivity term for the amorphous alloys varies as T^2. Here the apparent linear increase of T_K with concentration may be attributed to the d-d spin interaction. On the other hand, $T_d' \simeq T_K$ remains almost constant up to 22 at.% P in $(Pd_{70}Mn_{30})_{100-y}P_y$, then increases as almost the square of the phosphorus content. The nonlinearity in the concentration dependence suggests that there are correlations between the paramagnetic ions in addition to those due to RKY interactions. The increase of T_d as the Mn concentration increases was previously noticed for Cu alloys containing Cr where the $\ell n\, R$ versus T temperature independent region increased with increase in magnetic field[68]. So the above result in Pd-Mn-P may arise from the same origin, as it occurs in a region of temperature where almost all other phenomena are weak and could be interpreted in terms of an increase in the internal field. This would also explain the decrease of the

absolute value of the slope γ of $\ell n\ T$ (Tables XVII and XIX) in Pd-Mn-P with increase in manganese content as due to the increase in the interacting localized spins in terms of an increased internal field[122,123]. This was seen experimentally and proved theoretically by Abrikosov[71], Liu[124] and Silverstein[108] in other alloys, also with increase in magnetic element concentration.

The difference between T_K and T_{LSF} is understandable as the constants in the two equations vary. The Kaiser-Doniach results applied to Pd-Mn-P amorphous alloy system imply that the transition from T^2 to T dependence of the resistivity occurs around $T_c \simeq 0.5\ T_{LSF}$, which is in agreement with the experimentally determined linear portion of the curve T_L (Tables XVII and XIX). The concentration independent T^2 behavior in Pd-Mn-P was also noticed in very accurate measurements in progress on AlMn and AlCr[126].

The LSF almost-linear dependence of resistivity on T at higher temperature may be understood in terms of the Bose character of localized paramagnons, since at temperatures larger than T_s the excitations take on classical equipartition occupation probabilities; the number of thermal excitations is proportional to T. Thus, the appearance of a linear law may be expected as a fairly general consequence of a low-lying Bose excitation spectrum. Kaiser and Doniach established an analogy between the spin fluctuation resistivity and the Bloch-Gruneisen expression for resistivity due to electron phonon scattering, which also shows a linear T dependence at higher temperatures. Fitting Kaiser and Doniach's linear dependent equation to the high temperature (200-300^{o}K) range yielded T_{LSF} values higher

than expected; for instance, for $(Pd_{62}Mn_{38})_{77}P_{23}$, $T_{LSF} = 600^{o}K$, while the T^2 portion of the curve yielded a $T_{LSF} = 443.4^{o}K$, which is in close agreement with the experimental curve. The deviation of the high temperature values of T_{LSF} may be attributed to the phonon contribution to the LSF resistivity. Such a contribution would vary linearly with temperature, and although it would not alter the linear temperature dependence of the impurity resistivity, it might alter the estimate of the T_{LSF} by some 10%. An evaluation and separation of this contribution was not attempted, because the resistivity of Pd-Mn-P is about one order of magnitude higher than the phonon resistivity in pure Pd or Mn and this can lead us to believe that this phonon contribution is small. Another reason for the deviation could be that the enhancement factor was not taken into consideration[127].

The breakdown of Matthiessen's rule in Pd-Mn-P is attributed to the relaxation of the conservation of momentum requirement in electron phonon scattering brought about by the loss of translational symmetry in the alloy[128]. Recently another way to explain the negative temperature dependence, following the same approach as that of Caplin and Rizzuto[116] was attempted[129]. It takes into account the dynamical splitting between the spin up and spin down vbs's induced by the spin fluctuations, by introducing an effective energy width $\Delta' = \Delta/n$ and then using the Sommerfeld expansion to calculate the scattering cross section. As a first approximation, it assumes that the effect of the thermal fluctuations can be approximated by considering, in place of one vbs of Lorenzian shape, two such states shifted

by kT around E_F (Anderson localized state model), and it results in a linear T dependence at high temperatures. This model, however, is too crude to be given further attention.

C. Magnetoresistivity

1. Pd-Co-P

The magnetoresistivity of Pd-Co-P is negative and varies from 2 to 16×10^{-3} as the concentration of cobalt increases from 15 to 50 at.%. The negative magnetoresistivity in Pd-Mn-P is much smaller and of the order of 1 to 3×10^{-4}. The magnetoresistivity results for Pd-Co-P, Fig. 39, for $H \geq 4$ kOe were best fitted to a relation

$$\Delta\rho_H/\rho_{H=0} = -(aH + bH^2) \qquad (45)$$

where H, the applied magnetic field is in kOe. For $(Pd_{85}Co_{15})_{80}P_{20}$, for instance, $a = 1.36$ and $b = 9.4 \times 10^{-6}$. Yosida[16] has shown that for a ferromagnet, the magnetoresistance is proportional to $-H$, and for a paramagnet, it is proportional to $-H^2$. This last term is attributed to an s-d exchange interaction. In Pd-Co-P the experimental results suggest, therefore, that ferromagnetism and paramagnetism coexist in the amorphous alloy even for $T \ll T_c$. This is consistent with the resistivity minimum found in these alloys below T_c. A better fit for the magnetoresistance versus H was obtained by fitting the curve to a formula of the form:

$$\Delta\rho_H/\rho_{H=)} = -qH^n \qquad (46)$$

Below 4 kOe the magnetoresistance was very close to H^2, indicating

the paramagnetic nature of the magnetic ions. Above 4 kOe, n decreased with increase in Co concentration, reaching 1.3 for 50 at.% Co, which is a clear indication of the loss of paramagnetic ions in favor of ferromagnetic spin ordering. The fitting parameter q also decreased with increase in Co concentration. Even though the paramagnetic contribution can be extracted from the observed magnetoresistance, quantitative agreement with the theoretical results of Béal-Monod and Weiner[75] is rather poor.

Qualitative agreement in terms of measured magnetization was satisfactory and was attempted by fitting the magnetoresistance to a general expression of the form:

$$\rho_H/\rho_{H=0} = -(c\sigma_\alpha + d\sigma_\alpha^n) \qquad (47)$$

where σ_α is the measured magnetization. As an example, for $(Pd_{85}Co_{15})_{80}P_{20}$, $d(\%/\mu_B^n) = 0.145$ and $n = 2.74$. The fact that the value of n is generally close to 2 seems to be due to the existence of ferromagnetism, since 4.2^oK is well below the Curie temperature of these alloys. This is in accordance with Yosida's theory[131], which shows that for ferromagnets the magnetoresistance is proportional to $-H^2$, and this behavior is attributed to an s-d exchange interaction. The deviation of n from 2 at low fields indicates, in terms of the theoretical equation (42), that the quasi-bound state model might not be fully valid. It is also evident that the absolute value of the negative magnetoresistivity increases somewhat linearly with Co concentration. This is consistent with the expected concentration dependence of the magnetization σ_α, which is proportional to n.

The existence of the c parameter in the above equation is attributed to the existence of paramagnetic spins.

Although the quantitative analysis of the negative magnetoresistance due to ferromagnetism is complicated by the existence of s-d exchange interaction in Pd-Co-P, the observed data obey equation (47) qualitatively if σ_α is the measured magnetization. The appreciable negative magnetoresistance at high concentration of Co is probably due to the large magnetization arising from a kind of d-d spin clustering among Co atoms in the alloys. The saturation of the negative magnetoresistance at high fields corresponds to the saturation magnetization.

2. $(Pd_{100-x}Mn_x)_{77}P_{23}$ Alloys

Two characteristics are noted in Fig. 40: (a) the negative magnetoresistance of the $(Pd_{100-x}Mn_x)_{77}P_{23}$ alloys increases as the manganese concentration increases from 15 to 30 at.%, and (b) although still negative, the absolute value of the magnetoresistance decreases to become almost field independent as Mn increases from 35 to 38 at.%. The absence of strong negative magnetoresistance for 35 to 38 at.% is due to the fact that (1) the magnetization σ_α at 4.2^oK is very small at these compositions as confirmed by the magnetic measurements, and (2) the mobility increases rapidly[135,136] with the increase of manganese concentration.

Similar behavior was observed by Gerritsen[132] in crystalline Au-Mn and in dilute alloys, but the transition metal concentration at which the minimum occurs is very small--of the order of less than 0.1 at.%. The fact that this minimum in amorphous alloys occurs at quite

a high concentration of manganese indicates that the d-d spin interaction between transition atoms is weaker in amorphous alloys than in crystalline systems. The interaction between localized moments and the conduction electrons was shown to result in negative magnetoresistance, which agrees with the experimental results. According to Toyozawa[133], the magnetoresistance dependence on concentration could be explained by the overlaps between the electron wave function belonging to different paramagnetic spins (which become appreciable as the concentration increases) and the localization of the electrons, thus causing the negative magnetoresistance to become obscured. Mott and Zinamon[134] have suggested that as long as moments persist in an alloy, the density of states should consist of two overlapping Hubbard bands, so that the Fermi energy (unless the compensation is high) will be in a pseudogap, which will give rise to a positive term to the magnetoresistance. Therefore the magnetoresistivity curves could be interpreted in terms of the number of electrons being influenced by each mechanism.

3. $(Pd_{70}Mn_{30})_{100-y}P_y$ Alloys

The behavior observed with the change in phosphorus concentration is similar to that obtained with change in manganese content. The magnetoresistance (a) is positive for low phosphorus concentration and the absolute value increases with P concentration from 17 to 19 at.% P, and (b) decreases in absolute value for 20 at.% P, then becomes negative and increases in absolute value as phosphorus increases from 21 to 26 at.%. The second characteristic is reasonably

consistent with the dependence of σ_α on phosphorus concentration. The theoretical results of Béal-Monod and Weiner[75] gave a rather poor fitting, even though the paramagnetic part of the magnetoresistivity was extracted. Recently Mell[137] has found a positive magnetoresistivity in amorphous films of InAs and InP. Therefore the experimental magnetoresistivity results for amorphous alloys suggest the existence of ferromagnetism or antiferromagnetism with paramagnetic random spins, even for $T < T_c$ or T_N. This is consistent with the localized spin fluctuation and Kondo-like behavior observed in these alloys.

D. Magnetic Properties

1. Pd-Co-P Alloys

The magnetization versus temperature curve for Pd-Co-P implies the existence of ferromagnetism in these alloys. The magnetic isothermals can be expressed by

$$\sigma(H,T) = \chi H + \sigma(0,T)$$

where $\sigma(H,T)$ is the magnetization at a temperature T and a field H, $\sigma(0,T)$ is the spontaneous magnetization, and χ is the total susceptibility. The classical method for obtaining the ferromagnetic Curie temperature T_c by plotting $\sigma^2(0,T)$ versus T and extrapolating the linear part to the temperature axis is not applicable in the present alloys, since the Curie temperature is above room temperature. High temperature magnetic transition determination (Sec. IV-D.2) revealed that the Curie temperature varies from 398^oK to 273^oK as the

cobalt concentration decreases from 50 to 15 at.% (Table XXII). A maximum in the magnetization curve appears at lower temperatures for 15 at.% Co. This maximum is related to the ordering of the free paramagnetic spins responsible for the Kondo-like behavior observed in the resistivity measurements. The magnetic nature of this ordering can be inferred from the quenching by an external field of the peak in the magnetization. It has also been suggested that the maximum in magnetization could be attributed to possible antiferromagnetic coupling of ferromagnetic domains[138,139], but this approach does not explain the observed quenching of the peak in magnetization at high applied magnetic field. Mössbauer study of Pd-Fe-P[140] revealed that the Pd atoms do not play a large role in these amorphous alloys, since the presence of phosphorus as an electron donor greatly reduces the polarization of the palladium[141] which appears to have a full "4d" band. A similar band filling effect of this type might be expected for Pd-Co-P alloys which might explain the reduced moment. Unfortunately this could not be checked since the amorphous range does not extend to lower cobalt concentration, but amorphous $Pd_{80}Si_{20}$ was shown to have a very low susceptibility $\chi(10^{-7},10^{-8}$emu/g) indicating a filled "d" band. Another factor that contributes to the reduced magnetization could be found in terms of Handrich's treatment[142] of the amorphous ferromagnet on the basis of the molecular field approximation. Starting from the Heisenberg-Dirac Hamiltonian,

$$H = - \sum J_{ij} \vec{S}_i \vec{S}_j$$

and taking into account the amorphous nature of the material by

allowing random fluctuations in the exchange integrals J_{ij}, he found that the effect of these fluctuations is to produce a reduced magnetization of the form

$$\sigma = \frac{1}{2}\{B_S[(1+\delta)x] + B_S[(1-\delta)x]\}$$

where B_S is the Brillouin function for spin S, $x = 3S/(S+1)(\sigma/\tau)$, $\tau = T/T_c$ and δ is a parameter reflecting the magnitude of the fluctuations. For $\delta < 1$ ferromagnetism exists. The failure of the theory to account for the low-temperature behavior at 15 at.% cobalt is a characteristic of all molecular field theories and is a result of the inability to take into consideration the low density tails of the spin random fluctuation probability. The effect of the hybridization of the s and d bands on the occurrence of ferromagnetism has recently been studied by Koishore and Joshi[143]. Their treatment uses the Hartree-Fock approximation and the so-called Hubbard approximation[144], but no characteristic behavior is deduced. Recently Rivier[145] treated the magnetism in amorphous alloys in terms of the Ruderman-Kittell-Kasuya-Yosida (RKKY) type iteration. The oscillatory character of the interaction together with the randomness in the distribution of magnetic moments is responsible for the magnetic behavior of this "well-defined state of magnetic matter". Each magnetic atom is tightly coupled to a probability distribution effective field due to all other neighboring atoms. The onset of "local magnetic order" depends on the strength of the "magnetic correlation" which is related to the effective field (external and internal) as well as the thermal noise. Therefore the magnetic characteristics of Pd-Co-P are described

very well by Rivier theoretical approach in terms of a collective and random distribution of magnetic spins. The isothermal magnetization increases linearly with the applied field, and a small tendency toward saturation may be observed at high fields or low temperatures, see Fig. 50. At 4.2°K, considerable remanance is observed in $(Pd_{50}Co_{50})_{80}P_{20}$, (13 emu/g) and the alloy seems to saturate at 3.5 kOe. Its saturation moment is 0.534 $\beta\mu$/atom. The general non-saturation behavior of magnetization was found to be common to most amorphous ferromagnetic alloys. The decrease in saturation tendency, as expected from the Rivier model for magnetism in amorphous alloys, is attributed to the lack of interaction among increasingly separated cobalt atoms.

2. Pd-Mn-P Alloys

The magnetic susceptibility versus temperature at 6 kOe was measured as a function of varied concentrations of manganese and phosphorus, see Figs. 47 and 49. The inverse susceptibility deviates from the Curie-Weiss law and the magnetization undergoes a maximum at $T = T_{max}$, Tables XXIII and XXIV, which are typical behavior of many Kondo systems. Above T_{max} the $1/\chi$ versus T for manganese above 30 at.% in $(Pd_{100-x}Mn_x)_{77}P_{23}$ and phosphorus above 22 at.% in $(Pd_{70}Mn_{30})_{100-y}P_y$ seems to consist of two straight lines with a change of slope at a characteristic temperature τ_d'. Consequently the values of μ_{eff} and θ_p are not the same below and above τ_d'. The straight line drawn through the higher temperature points ($\tau_d' < T < 300°K$) gives a negative intercept. The effective magnetic

moment was determined using the relation $\mu_{eff} = g[S(S+1)]^{1/2}$ where g is the ratio of the angular moment to the angular momentum and $\sqrt{S(S+1)}$ is the value of the angular momentum of the electrons. The value obtained for μ_{eff} leads to an absolute value of the spin quantum number S between 0.63 and 0.78 μ_B per atom as the manganese increases from 25 to 37 at.%. Similarly the spin quantum number S varies between 0.66 and 0.76 as the phosphorus concentration increases from 22 to 26. In crystalline alloys, the electric field of the other atoms or ions surrounding the metal ion in its compound restricts the orbital motion of the electrons so that the orbital angular moment and hence the orbital moment become partially or wholly quenched. Such a mechanism is not operative in the case of amorphous alloys, but due to the lack of any other approach, the magnetic moment was assumed to be due to electron spins alone.

The existing theories[146,147] predict that as T approaches zero the magnetic moment should decrease due to the formation of the quasi-bound state while the susceptibility becomes finite. The susceptibility could therefore be expressed as:

$$\chi = \mu_{eff}^2 f(T)/3kT$$

The effective magnetic moment $\mu_{eff}\sqrt{f(T)}$ obtained in this way is shown in Figs. 54 and 55. The difference between the S value of 5/2 assuming MN^{++} and the experimentally determined value of 1.78 which increases to 2.35 μ_B/Mn atom as the manganese increases between 17 to 37 at.% suggests that some conduction electrons provided by phosphorus fill the d shell of Mn. The value of μ_{eff} obtained for lower temperature is

smaller than the effective moment obtained above τ_d, implying the existence of magnetic interaction between paramagnetic spins. The characteristic temperature τ_d is probably the Kondo temperature for the following reasons: (a) τ_d is very close to the temperature at which the resistivity ρ deviates from $-\ell n\ T$ dependence; (b) the effective magnetic moment decreases below τ_d; (c) the susceptibility χ obeys a general function:

$$\chi = \mu_{eff}^2\ f(T)/3kT$$

where

$$f(T) = \text{constant}\ \ T/T_d^{1/2}$$

for $T_{max} < T < \tau_d$. This result gives $\chi \propto (T/T_d)^{-1/2}$ for $T << \tau_d$ as suggested by Anderson[52]. As shown in Figs. 56 and 57, this law seems to be obeyed approximately between T_{max} and τ_d' in the χ versus $\ell n\ T$ plot. Daybell and Steyert[68] suggested that θ_p is equal to τ_d', so an attempt to plot τ_d', θ_p and T_d' (the deviation from $\ell n\ T$ behavior in the resistivity measurement) in Figs. 58 and 59 revealed that the three parameters are closely related. Similar behavior was previously observed in Mn-Pd-Si[148]. But if the quasi-bound state model holds, the Curie-Weiss law should be obeyed--which is not the case--since the high temperature portion of the $1/\chi$ versus T curves for concentrations of phosphorus below 20 at.% and manganese below 25 at.% has a distinct curvature, concave towards the temperature axis. The fact that the presence of such curvature in a region where the magnitude of the localized moment is temperature independent suggests

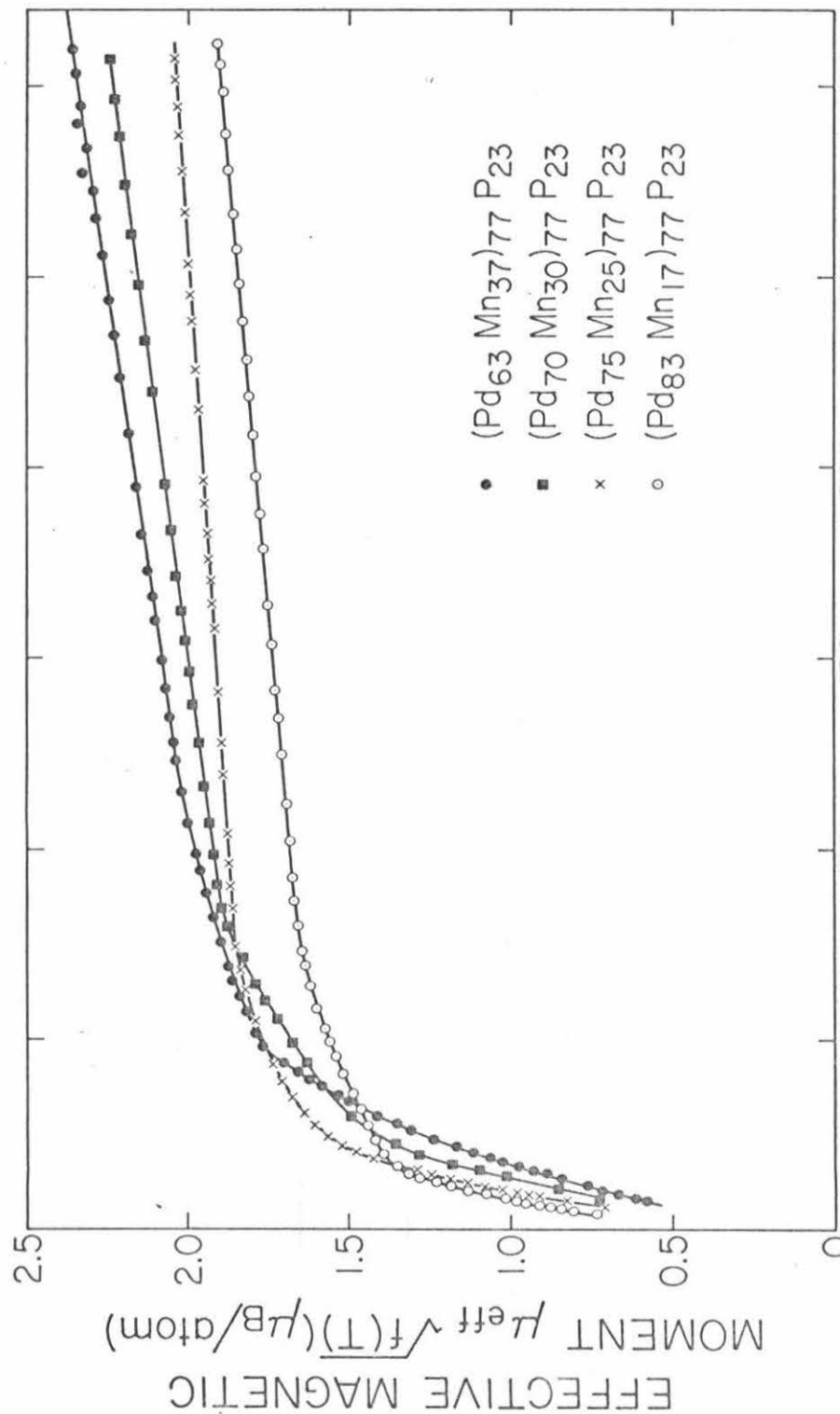

Fig. 54. Effective magnetic moment per Mn atom versus temperature for $(Pd_{100-x}Mn_x)_{77}P_{23}$

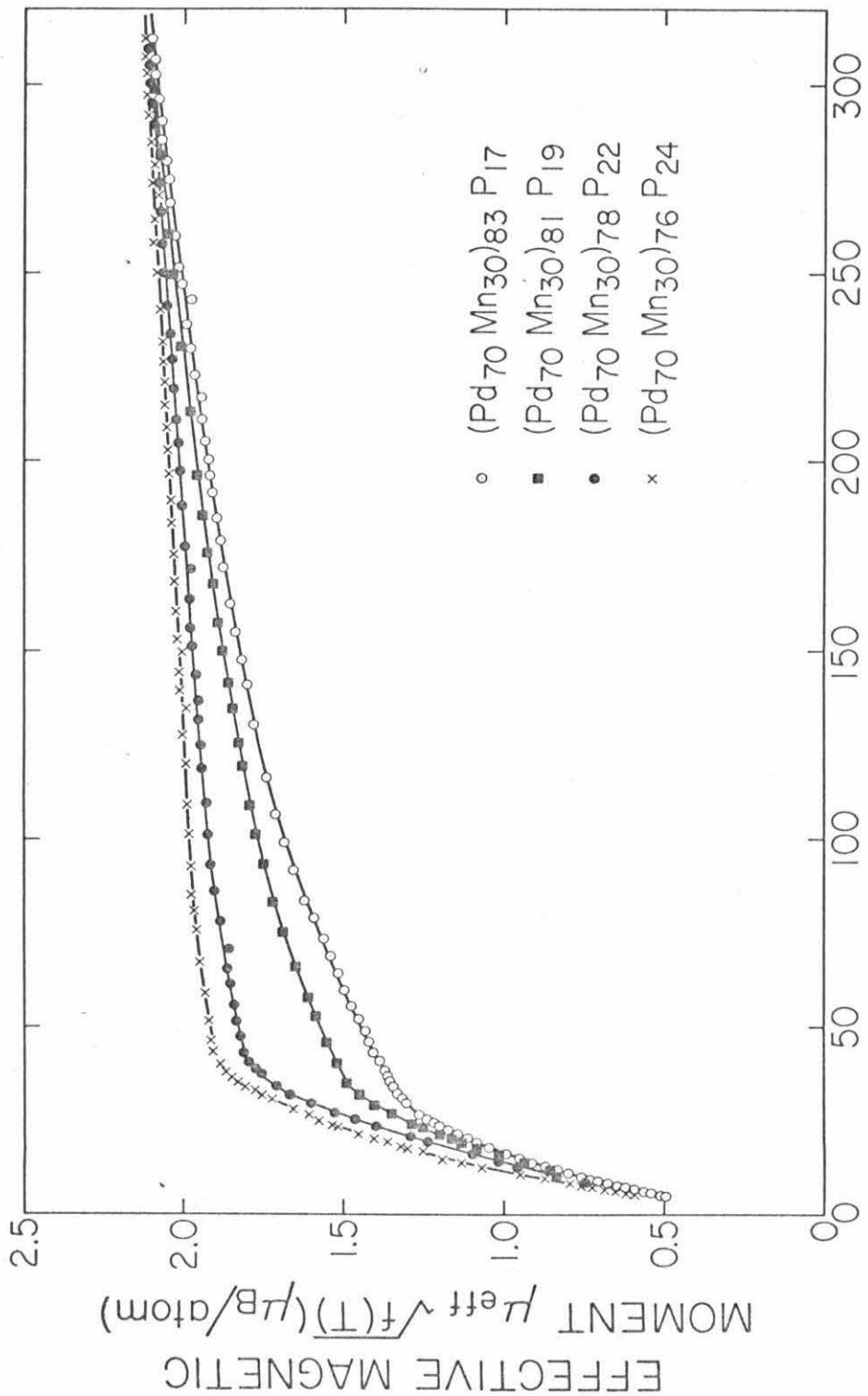

Fig. 55. Effective magnetic moment per Mn atom versus temperature for $(Pd_{70}Mn_{30})_{100-y}P_y$.

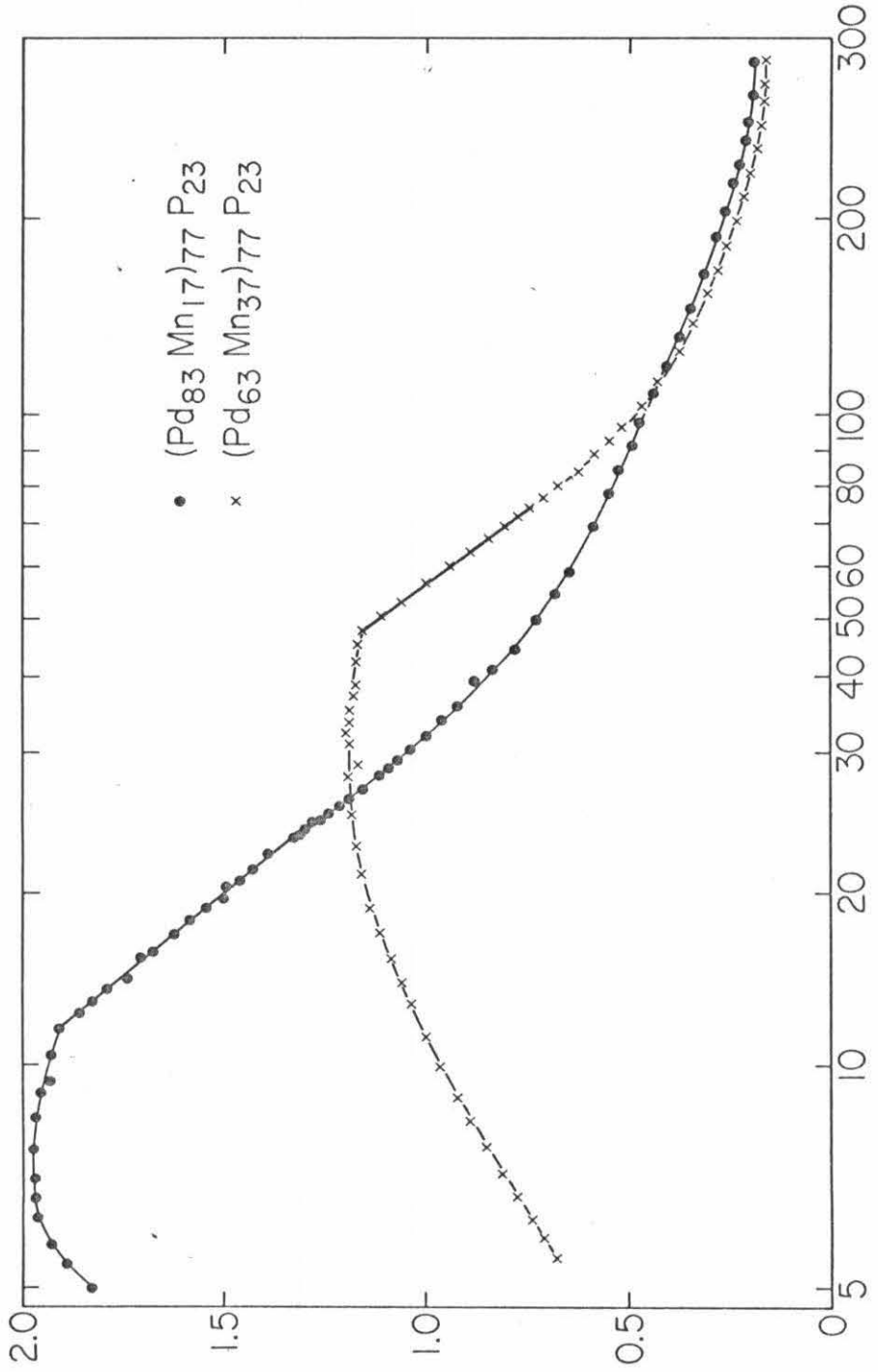

Fig. 56. Susceptibility per gram of $(Pd_{100-x}Mn_x)_{77}P_{23}$ Alloys versus Temperature

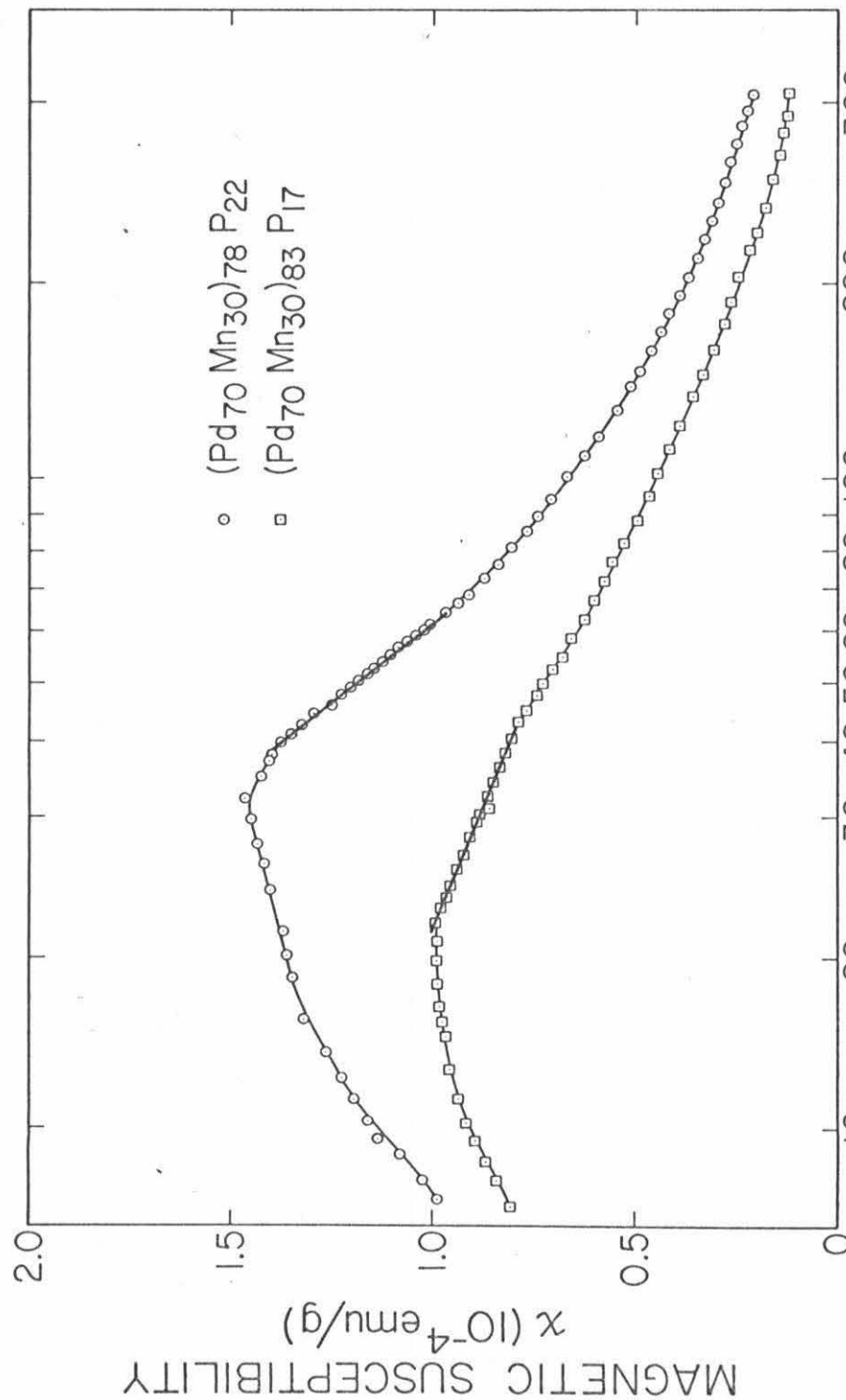

Fig. 57. Susceptibility per gram of $(Pd_{70}Mn_{30})_{100-y}P_y$ Alloys versus Temperature

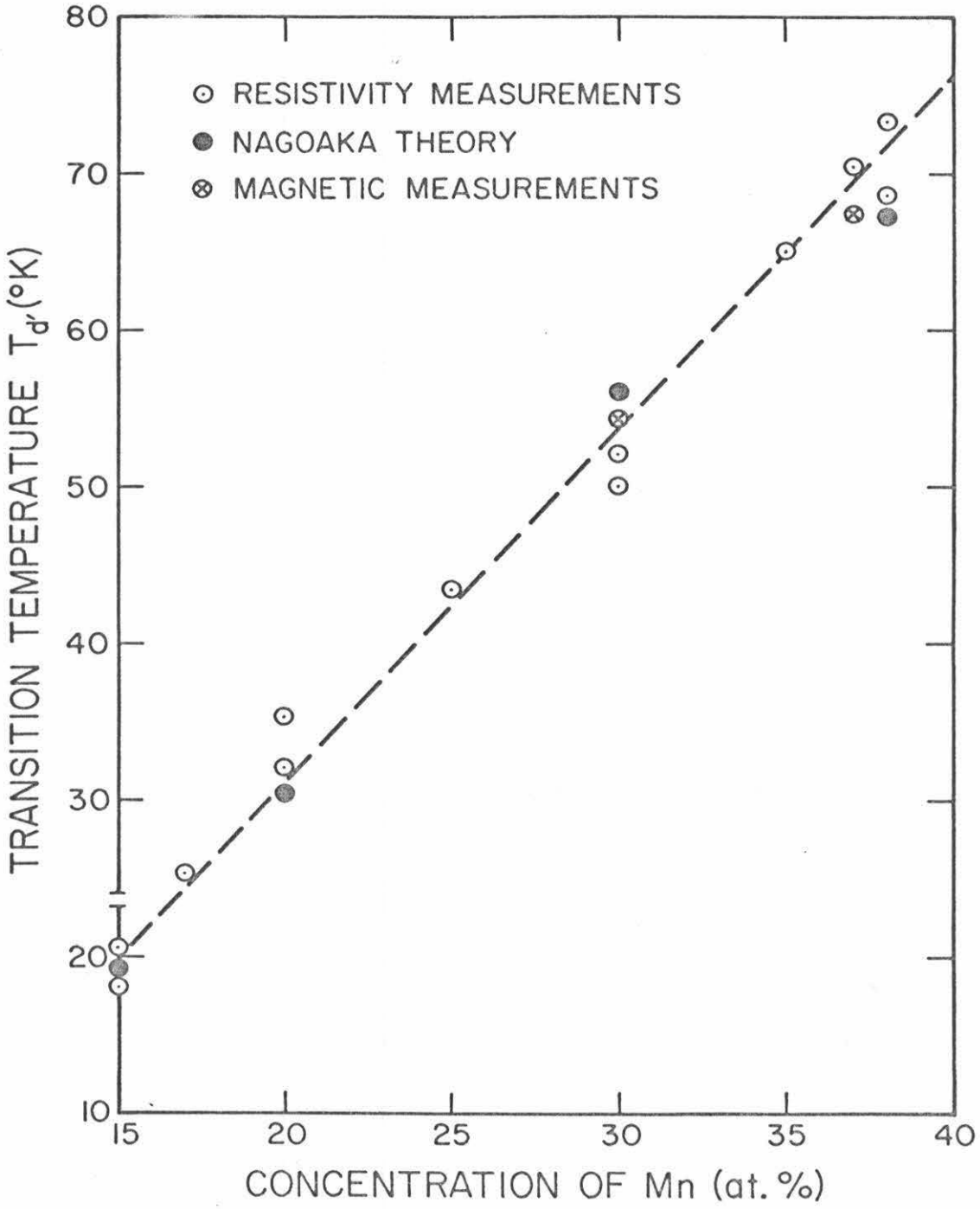

Fig. 58. Temperature at which the resistivity deviates from ℓn T law (o) versus Mn concentration, (o) from Table XVII, and (o) from Table XXIII.

Table XXIV. Results of Magnetic Measurements for $(Pd_{70}Mn_{30})_{100-y}P_y$

Composition	T_{max} (^oK)	σ_{max} β_μ	τ_d' (^oK)	$\mu_{eff}'(\mu_B/atom)$ $30^oK < T < \tau_d'$	θ_p' (^oK) $30^oK < T < \tau_d'$	S	$\mu_{eff}\sqrt{f(T)}$ $\tau_d' < T < 300^oK$	θ_p(^oK) $\tau_d' < T < 300^oK$
$(Pd_{70}Mn_{30})_{83}P_{17}$	19.15	0.00865	-	-	-	-	2.085	-
$(Pd_{70}Mn_{30})_{81}P_{19}$	25.20	0.00964	-	-	-	-	2.092	-
$(Pd_{70}Mn_{30})_{78}P_{22}$	30.30	0.01230	60.4	0.647	- 17.2	0.664	2.103	- 27.6
$(Pd_{70}Mn_{30})_{77}P_{23}$	32.80	0.01342	54.2	0.701	- 11.8	0.726	2.240	- 33.9
$(Pd_{70}Mn_{30})_{76}P_{24}$	36.40	0.01360	50.2	0.758	- 8.2	0.763	2.320	- 13.4

Table XXIII. Results of Magnetic Measurements for $(Pd_{100-x}Mn_x)_{77}P_{23}$

Composition	T_{max} (^oK)	σ_{max} β_μ	τ_d' (^oK)	$\mu_{eff}'(\mu_\beta/atom)$ $30^oK < T < \tau_d'$	$\theta_p'(^oK)$ $30^oK < T < \tau_d'$	S	$\mu_{eff}\sqrt{f(T)}$ (μ_B/Mn atom) $\tau_d' < T < 300^oK$	$\theta_p(^oK)$ $\tau_d' < T < 300^oK$)
$(Pd_{83}Mn_{17})_{77}P_{23}$	7.6	0.01725	-	-	-	-	1.78	-
$(Pd_{75}Mn_{25})_{77}P_{23}$	19.97	0.01515	-	0.583	+ 3.49	0.636	2.04	-28.5
$(Pd_{70}Mn_{30})_{77}P_{23}$	32.77	0.01342	54.2	0.701	-11.80	0.726	2.24	-33.9
$(Pd_{63}Mn_{37})_{77}P_{23}$	41.20	0.00932	67.5	0.763	-35.6	0.777	2.35	-40.7

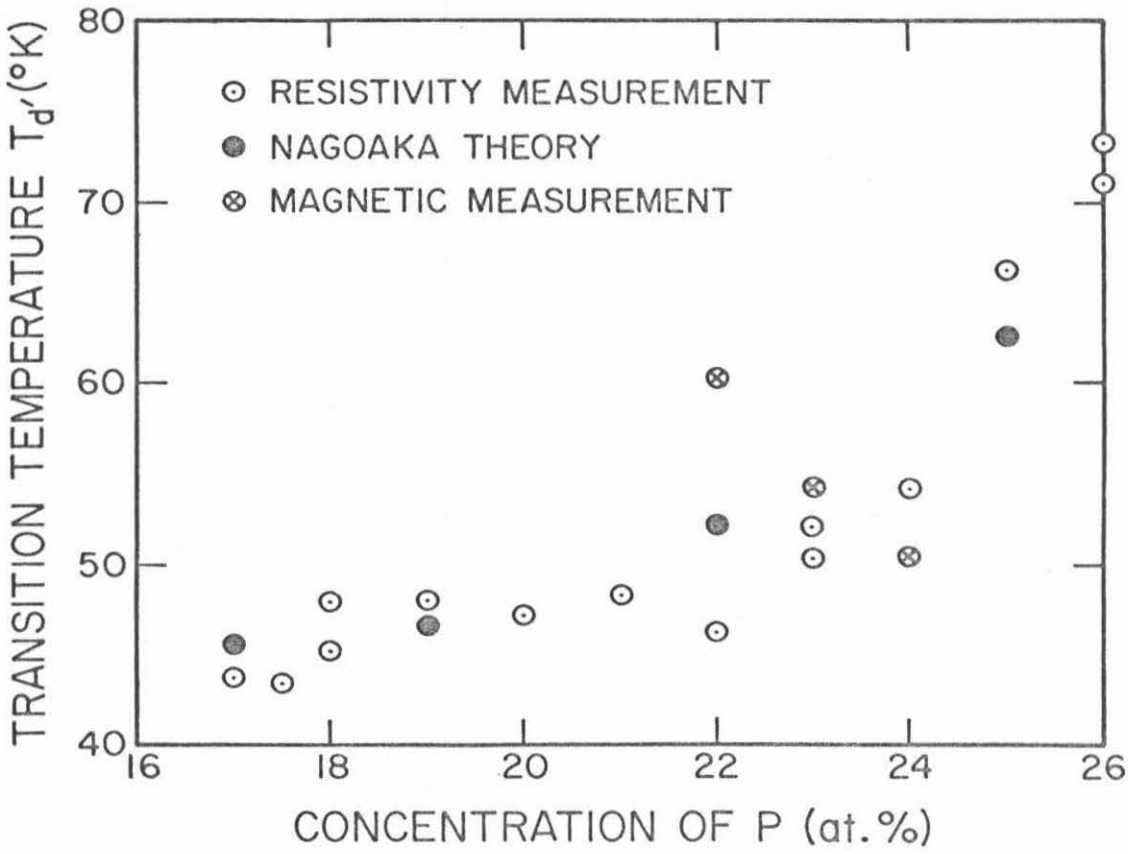

Fig. 59. Temperature at which the resistivity deviates from ℓn T law (o) versus P concentration, (o) from Table XIX and o from Table XXIV

that ferrimagnetic behavior does not exist. Also, the peak in the magnetization curve persists for all compositions of the alloy systems, and while the temperature at which the maximum occurs increases with increase in manganese content, the intensity of the magnetization maxima decreases drastically with increase in manganese concentration. Similar behavior is observed with increase in phosphorus content, but the intensity of the magnetization maxima is proportional to the phosphorus content. It can also be noticed that these maxima become broader and more diffuse with increase in either manganese or phosphorus content. Generally, such a peak in magnetization at low temperatures is associated with antiferromagnetic alignment of the spin. The belief that the susceptibility maximum is a Néel temperature is totally excluded, as preliminary heat capacity measurements failed to show a λ transition at the same temperature range. Qualitative considerations therefore suggest that the susceptibility maximum is a variant of the Van Vleck type of paramagnetism (VVP). VVP occurs when the ground state of the ion is a singlet and the crystal field interaction is strong compared to exchange. The ions, upon cooling, do not order but instead settle into the singlet ground state in which they possess only an induced moment. Thus, in this case, magnetization increases as temperature falls and finally levels off at some low temperature when the excited, permanent moment-carrying states are no longer populated to any appreciable extent. Under appropriate circumstances it appeared that the magnetization could pass through a maximum instead of leveling off to some limiting value as expected from the LSF resistivity mechanism. The circumstances under which this occurs could require a

highly magnetic excited state or states, only slightly higher in energy than the singlet ground state. Magnetization could continue to rise with decreasing temperature as long as a significant fraction (perhaps 5% or so) of the ions are in the excited magnetic state. Eventually depopulation of the excited state must occur and the system will exhibit the reduced magnetization characteristics of the singlet ground state. Thus qualitatively, it can be seen how the maximum in magnetization versus temperature arises, but unfortunately a quantitative demonstration of the energies ε_i and the magnetic moments μ_i is difficult due to the randomness and variation of the several crystal field states of the ions in an amorphous structure.

$$\chi = \frac{N_o}{H} \frac{\sum \mu_i \exp(-\varepsilon_i/kT)}{\sum \exp(-\varepsilon_i/kT)}$$

The nonlinearity of χ^{-1} versus T curve and the magnitude of χ for $T > 50^oK$ indicate that Mn, which appears to be non-magnetic below 50^oK, may be acquiring a moment at higher temperatures as explained in the LSF approach. Crystalline $NdNi_5$ exhibits similar behavior[149]. It is well known that manganese is a magnetic atom. Electron transfer from phosphorus to manganese is barely sufficient to fill the latter's d band, leaving infinitely small moment. The changing electronic configuration of manganese undoubtedly makes a contribution to both the magnetic and electrical properties.

Another difficulty in the study of magnetism in amorphous alloys is that the composition dependent exchange interactions are randomly distributed. The overall shape of the magnetization curves

is typical of those observed in garnets (RIG,YIG) resulting from the interplay of different exchange forces. Also, in amorphous alloys, the exchange integral J depends not only on metallic elements through direct exchanges but also on nonmetallic elements through superexchanges. In NiO [150], the nonmetallic O is localized between the two metallic elements Ni, and each J depends solely on a single nonmetallic elements. Gambino[151] measured the magnetic moment of $GdNi_{1-x}O_x$ and found that GdNi is ferromagnetic, but small amounts of oxygen ($x = 0.05$) cause paramagnetism and short-range antiferromagnetic order to set in as found by neutron diffraction analysis.

The increase in width of the magnetization peak with manganese and phosphorus could be attributed merely to the random fluctuations in local spin arrangement. It is also suggested that one of the dominant effects to be considered in the distribution of magnetic moments is the electron-transfer effect from phosphorus. As the P content remains constant, this effect alone cannot explain the increase in width observed with increase in manganese concentration. There are also the conduction electrons, which may become polarized through the Ruderman-Kittel-Kasuya-Yosida (RKKY) interaction and contribute to the observed width in the magnetization maxima[14,131,151]. This nonuniform spin polarization leads to the existence of the Kondo-like localized spin fluctuation effect observed in the resistivity measurement. The possibility of spin fluctuations as the source of both T and T^2 terms in the resistivity receives added proof from the magnetic measurements. In the case of the spin fluctuation, the coefficient β_{LSF} (equation (40) should be proportional to χ^2 [100] where χ is the

spin susceptibility. This relation is obeyed in the amorphous Pd-Mn-P. Also according to Kaiser and Doniach[69], the critical temperature T_c as defined in the last reference should decrease and β_{LSF} should increase with increase in the concentration of the 3d metal, which is confirmed by the results shown in Tables XVII and XIX. Thus, the relationship between susceptibility and resistivity confirms the localized spin fluctuation model for the Pd-Mn-P alloys.

VIII CONCLUSIONS

The structure and properties of amorphous Pd-Mn-P and Pd-Co-P alloys quenched from the liquid state have been investigated in terms of the effect of (1) the 3d band filling of the first transition metal group, (2) the phosphorus concentration effect which acts as an electron donor, and (3) the transition metal concentration.

The structure of the amorphous alloys was tentatively characterized in terms of relatively simple geometrical entities and their statistical distribution. This "geometrical entities" model has the advantage that it accounts not only for the size and concentration of the constituents but also for the affinity among the atomic components. From x-ray generated distribution functions, precise information about these structural entities was obtained as well as structural parameters such as: the number of nearest neighbors, the metal-to-metal distance, the degree of short-range order, and the affinity between metal-to-metal and metal-metalloid.

The effect of the change in transition metal content could be summarized as follows: (a) the transition metal solubility at constant phosphorus content decreases as we go across the transition metal series towards the left, from 70 at.% for Ni to 22 at.% for Mn; (b) the composition dependent rate of shift in $I(K)$ and $W(r)$ becomes decreasingly noticeable as the transition metal changes from Ni to Mn; (c) the ratio of r_2/r_1 which indicates the degree of short-range order changes in the above sequence from 1.65 to 1.82, which is closer to the liquid metal in which $1.8 \leq r_2/r_1 \leq 2.0$, indicating a greater

disorder in Mn alloys; (d) the first peak in the intensity versus 2θ has a shoulder on the left-hand side for Pd-Fe-P and Pd-Ni-P, while the shoulder is on the right-hand side for Pd-Mn-P (this is associated with the existence of higher number of unlike atom pairs in Fe and Ni than in Mn alloys); (e) contrary to what was observed in Pd-Fe-P and Pd-Ni-P amorphous metallic alloys, there is no shoulder on the high angle side of the second peak of I(K); (f) the number of maxima at higher interatomic distance (which gives an insight on the short-range order) decreases with increase in phosphorus concentration. The rate of damping of those maxima increases, while they become wider and flatter approaching a liquid-like structure. The transport properties of these amorphous alloys indicate that they are all electrical conductors. The magnetic properties of Pd-Co-P alloys show that they are good examples of amorphous ferromagnets. These alloys show a Curie temperature between 272.5 and 399^{o}K as the cobalt concentration increases from 15 to 50 at.%. The inverse susceptibility and magnetization retain the characteristic shape of crystalline ferromagnetic alloys, except that they are flattened slightly, which is attributed to a weak d-d spin interaction. The magnitude of the magnetic moment suggests a filling of the 3d band of cobalt by electron transfer from phosphorus. The Pd atoms appear to play a small role in the magnetization, since it is believed that its 4d shell is filled. Below a critical concentration, the short-range exchange interactions which produce the ferromagnetism are unable to establish a long-range magnetic order, and a peak in the magnetization shows up (15 at.% Co) at the lowest temperature range. This local magnetic ordering is due to

some indirect exchange interaction through the conduction electrons. The H/T superposition of the points does not hold and the existence of remanence suggests that superparamagnetism does not exist. The electrical resistivity of Pd-Co-P indicates the possible coexistence of a Kondo-like minimum in disordered ferromagnetic alloys even at high concentrations of transition metals. The minimum becomes less important as the transition metal concentration increases and the coefficients of $\ell n\ T$ and T^2 become smaller and strongly temperature dependent. The spin ordering in these kinds of alloys can be simulated as the ordering due to an applied "external field" or as an increase in "internal fields" due to an increase in transition metal concentration. The temperature coefficient of resistivity is positive for Pd-Fe-P, Pd-Ni-P and Pd-Co-P, while it is negative for Pd-Mn-P. It is possible to account for the negative temperature dependence by the spin fluctuation model[113,69] or by the simple phase shift analysis[153] and also by considering the modification of the exchange interaction constant through interference between potential and exchange scattering[73]. The LSF model seems most appropriate and has been found capable of yielding many features of the observed behavior. The high density of states at the Fermi energy for manganese accounts for the observed resistivity coefficient. This is confirmed by preliminary measurements made on Pd-Cr-P, which has also a negative temperature dependence. The magnetic measurements made on Pd-Mn-P suggest that a combination of localized moments on Mn sites and atomic disorder have produced a large spin disorder, which is fairly temperature independent at high temperatures. The peak in the magnetization in the lowest temperature range is attributed to a

variant of the Van Vleck type of paramagnetism. This lower range magnetic contribution is lumped with free paramagnetic spins whose effect was observed in the resistivity measurements. There is a strong possibility that in these alloys most of the Mn atoms have Mn first or second neighbors, especially at this high concentration of manganese. This suggests that there may be superexchange through Pd or P atoms, which implies that the 3d holes belonging to the Mn atoms are not strictly localized near the Mn nucleus, but are spread over the Mn and its neighbors. It would not be surprising if there were some spin transfer of this sort, since one would expect that Pd-Mn-P has covalent bonding to a certain extent. From the available evidence it does not seem possible to decide to what extent localized paired 4s electrons are present. A conclusive interpretation of the magnetic behavior is not possible due to the random distribution of magnetic spins as well as randomization in the spin directions. The magnetic results confirm the existence of the localized spin fluctuation mechanism suggested by the resistivity measurements.

The magnetoresistivity of Pd-Co-P and Pd-Mn-P suggests that some type of magnetic order coexists with paramagnetic spins. At the lowest fields, the change in resistance in a magnetic field is proportional to the square of the applied fields, which indicates high paramagnetic spin concentration. At high fields or high concentration of transition metals, the change of resistance becomes proportional to the magnetic field, which could be attributed to magnetic ordering. The theoretical work of Hart[154] and Yosida[131] interprets the structure in terms of a short-range magnetic ordering that could arise from the

Ruderman-Kittel[152] type of interaction. The experimental results and the phenomenological interpretation attempted indicate a relation between the cooperative magnetic effects and the anomalous observed resistivity behavior. Mell and Stuke[137] believe that the negative magnetoresistance is contributed by that part of the current that is carried by electrons with energies near the Fermi level rather than spin dependent scattering. Generally the negative magnetoresistivity is a strong indication of the existence of localized moment. On the other hand, Mott and Zinamon[134] suggest that alloys having a magnetic moment would have a density of states of two overlapping Hubbard bands, so that the Fermi energy will be in the pseudogap which would give a positive effect. The decrease in the absolute value of the magnetoresistivity with increase in manganese concentration may be arising from an increase in mobility with increase in transition metal content. Qualitatively, the effect of a magnetic field (either of external or internal origin) would be to stabilize the "moment" so that the magnetic cross section and hence the resistivity would be increased. The actual situation, however, appears to be more complex, and there is no quantitative theory of the nature of the observed negative magnetoresistivity. Clearly, further theoretical and experimental studies of amorphous alloys are needed. The x-ray diffraction experiments are not sufficient to establish the fine details of the structure analysis. Neutron diffraction experiments would certainly help. Unfortunately, the size and especially the thickness of the quenched specimens do create experimental difficulties. Heat capacity measurements might also be of interest, as more light could be shed on the magnetic properties.

Finally, a lot of the complications due to the presence of three kinds of atoms would be reduced by studying amorphous binary alloys whenever possible.

REFERENCES

1. Pol Duwez, "Liquid Quenched Metallic Metastable Alloys", Fizika 2, Suppl. 2 (1970), 1.1 to 1.15.
2. M. H. Cohen and D. Turnbull, Nature 189, 131 (1961).
3. J. Prins, in Physics of Non-Crystalline Solids, edited by J. Prins, North Holland Publishing Co., Amsterdam (1965), p. 1.
4. J. Stevels, in Physics of Non-Crystalline Solids, edited by J. Prins, North Holland Publishing Co., Amsterdam (1965), p. 497.
5. K. Evstropyer, in The Structure of Glass: Proceedings of a Conference on the Structure of Glass, Leningrad (1953), Consultants Bureau, New York (1958).
6. J. Dixmier, K. Dor, and A. Guinier, in Physics of Non-Crystalline Solids, edited by J. Prins, North Holland Publishing Co., Amsterdam (1965), p. 67.
7. P. L. Maitrepierre, J. Appl. Phys. 40, 4826 (1969).
8. J. F. Sadoc, J. Dixmier and A. Guinier (private communications, 1972).
9. J. D. Bernal, Nature 185, 68 (1960).
10. J. Friedel, Nuovo Cimento Suppl. 7, 287 (1958).
11. P. W. Anderson, Phys. Rev. 124, 41 (1961).
12. G. J. van den Berg, Proc. of the 7th International Conference on Low Temperature Physics (Univ. of Toronto Press, 1961).
13. A. N. Gerritsen, Physica 19, 6 (1953).
14. T. Kasuya, Progr. Theoret. Phys. (Japan) 16, 58 (1956); 16, 45 (1956).
15. R. W. Schmitt, Phys. Rev. 103, 83 (1956); R. Schmitt and I. Jacobs, J. Phys. Chem. Solids 3, 324 (1954).

16. K. Yosida, Phys. Rev. 107, 396 (1957).

17. J. Kondo, Progr. Theoret. Phys. (Japan) 32, 37 (1964)

18. Y. Nagaoka, Phys. Rev. 138, A1112 (1965); Progr. Theoret. Phys. (Japan) 37, 13 (1967).

19. H. Suhl and D. Wong, Physics 3, 17 (1967).

20. D. R. Hamann, Phys. Rev. 158, 570 (1967).

21. N. Rivier, M. Zuckermann, and M. Sunjić, unpublished results.

22. A. Blanden in Theory of Magnetism in Transition Metal, W. Marshall (ed), Academic Press (1967), p. 393.

23. Pol Duwez and R. Willens, Trans. AIME 227, 362 (1963).

24. F. Zernicke and J. A. Prins, Z. Phys. 41, 184 (1927).

25. J. Dixmier, Fizika 2, Suppl. 2, p. 9.1 (1970).

26. K. Furukawa, Rep. Prog. Phys. 25, 395 (1962).

27. W. Ruland, Britl J. Appl. Phys. 15, 1301 (1964).

28. B. E. Warren, H. Krutter, and O. Morningstar, J. Am. Ceram. Soc. 19, 202 (1936).

29. B. E. Warren, X-Ray Diffraction, Addison Wesley, Reading, Mass. (1969).

30. D. T. Cromer and J. T. Waber, Acta Crystallogrphi 18, 104 (1965).

31. D. T. Cromer, Acta Crystallographi 18, 17 (1965).

32. R. W. James, The Optical Principles of the Diffraction of X-Rays, Vol. II in Crystalline State, published by A. Bell and Sons, Ltd. London, 1948.

33. J. Waser and V. Schomaker, Rev. Mod. Phys. 25, 671 (1953).

34. R. Kaplow, S. L. Strong, and B. L. Averbach, Phys. Rev. 138, 1336 (1965).

35. C. Pings and J. Waser, J. Chem. Phys. 48, 3016 (1968).

36. S. Strong and R. Kaplow, Rev. Sci. Instr. 37, 1495 (1966).

37. W. Ruland, Brit. J. Appl. Phys. 15, 1301 (1964).

38. R. Kaplow, B. L. Averbach and S. L. Strong, J. Phys. Chem. Solids Pergamon Press, Vol. 25, 1195-1204 (1964).

39. A. Sinha and P. Duwez, J. Phys. Chem. Solids, 32, 267 (1971).

40. T. Ino, J. Phys. Soc. Japan 12, 495 (1957).

41. A. Guinier, Theorie et technique de la radiocrystallographie, Dunod, Paris, 1956, p. 431.

42. N. S. Gingrich and L. Heaton, J. Chem. Phys. 34, 873 (1961).

43. P. G. Mikolaj and C. J. Pings, J. Phys. & Chem. of Liquids 1, 93 (1968).

44. L. Goldstein, Phys. Rev. 84, 466 (1951).

45. M. E. Fisher, J. Math. Phys. 5, 944 (1964).

46. L. Goldstein, Phys. Rev. 100, 981 (1955).

47. M. D. Johnson, P. Hutchinson, and N. H. March, Proc. Roy. Soc. London A282, 283 (1964).

48. N. Kitamura et al., J. Phys. Soc. Japan 11, 527 (1956).

49. N. F. Mott and W. D. Twose, Adv. Phys. 10, 107 (1962).

50. R. E. Borland, Proc. Phys. Soc. 78, 929 (1961).

51. R. E. Borland and N. F. Bird, Proc. Phys. Soc. 83, 23 (1964).

52. P. W. Anderson, Phys. Rev. 109, 1492 (1958); 164, 352 (1967).

53. H. Fröhlich, Proc. Roy. Soc. A 188, 521 (1947).

54. A. I. Gubanov, Quantum Electron Theory of Amorphous Conductors, (Consultant Bureau, 1965).

55. L. Banyai, Physienes des Semi-Conducteurs (Paris: Dunod, 1964), p. 417.

56. T. E.Faber, Adv. Phys. 15, 547 (1967).

57. M. P. Sarachik, E. Corenzwit and L. D. Longinotti, Phys. Rev. 135A, 1041 (1964).

58. J. R. Schrieffer, J. Appl. Phys. 38, 1143 (1967).

59. B. S. Chandrasekhar and J. K. Huhn, J. Phys. Chem. Solids 7, 259 (1958).

60. H. Jones, Handbuch der Physik 19 (Springer Verlag, Berlin, 1956), p. 227.

61. J. Friedel, J. Phys. Chem. Solids 1, 175 (1956).

62. F. J. Blatt, J. Phys. Chem. Solids 17, 177 (1961).

63. J. M. Ziman , Phil. Mag. 6, 1013 (1961).

64. F. J. Blatt, Solid State Phys., Vol. 4 (Academic Press, 1957), p. 200.

65. A. H. Wilson, The Theory of Metals,(Cambridge University Press, 1953).

66. A. B. Bhatia and K. S. Krishnan, Proc. Roy. Soc. A, 194, 1859 (1948).

67. A. K. Sinha, Phys. Rev. B 1, 4541 (1970).

68. M. D. Daybell and W. A. Steyert, Phys. Rev. Letters 20, 195 (1968)

69. A. B. Kaiser and S. Doniach, Int. J. Magn. 1, 11 (1970).

70. N. Rivier and M. J. Zuckermann, Phys. Rev. Letters 21, 904 (1968).

71. A. A. Abrikosov, Physica 2, 61 (1965).

72. B. Y. Boucher, J. Non-Cryst. Solids 7, 113 (1972).

73. Y. Nagaoka, J. Phys. Chem. Solids 27, 1139 (1966); Prog. Theor. Phys. (Japan) 39, 533 (1968).

74. A. B. Pippard, The Dynamics of Conduction Electrons (Gordon and Breach, New York, 1965), p. 90.

75. M. T. Beal Monod and R. A. Weiner, Phys. Rev. 170, 552 (1968).

76. W. Sasaki, J. Phys, Soc. Japan 20, 825 (1965).

77. M. Balkanski and A. Geisman, Solid State Comm. 4, 111 (1966).

78. See, for example, W. Seicksmith, Phil. Mag. 8, 158 (1929); Proc. Roy Soc. 110, 551 (1939); N. Lundquist and H. P. Myers, J. Sci. Instr. 39, 154 (1962); R. Bozorth et al., Phys. Rev. 103, 572 (1956); P. Johngenburger and C. W. Berghart, Appl. Sci. Res. Sect. B, 7, 366 (1961).

79. J. Dixmier and P. Duwez, J. Appl. Phys. 44, 1189 (1973)

80. D. H. Everett, Discuss. Faraday Soc. 43, 82 (1967).

81. I. R. McDonald and K. Singer, Quart. Rev. Chem. Soc. 24, 238 (1970).

82. J. L. Finney, Proc. Roy. Soc. London A 319, 495 (1970); 319, 479 (1970).

83. D. Turnbull and M. Cohen, J. Chem. Phys. 52, 3038 (1970).

84. A. S. Gargill III, J. Appl. Phys. 41, 12 (1970).

85. C. H. Bennett, J. Appl. Phys. 43, 6 (1972).

86. R. Collins, Proc. Phys. Soc. 83, 553 (1964); 86, 199 (1965); 86, 443 (1965).

87. W. W. Wood, Monte Carlo Studies of Simple Liquid Models, ed. N. V. Temerley, et al (Amsterdam, N. Holland, 1968), Ch. 5 of The Physics of Simple Liquids.

88. J. L. Finney, Ph.D. thesis, Univ. of London, 1968.

89. J. L. Finney and J. D. Bernal, Nature, Lond. 213, 1079 (1967).

90. G. A. Chadwick and W. A. Miller, Metal Sci. J. 1, 132 (1967).

91. L. Brillouin, Science and Information Theory (Academic Press, New York, 1963).

92. C. E. Shannon and W. Weaver, The Mathematical Theory of Communication (Univ. of Illinois Press, Urbana, 1959).

93. H. Ruppersberg, Memoires Scientifiques Rev. Metallurg. LXI, 10, 709 (1964).

94. G. Mason, Nature, Lond. 217, 733 (1968).

95. J. D. Bernal, Proc. Roy. Soc. Lond. a 280, 299 (1964).

96. G. S. Gargill III, J. App. Phys. 41, 2248 (1970).

97. L. V. Woodcock, Proc. Roy Soc. Lond. A 328, 83 (1972).

98. L. V. Woodcock, Z. Naturf. 2, 287 (1971); Chem. Phys. Letters 10, 257 (1971); Nature Phys. Letters 264, 63 (1971).

99. N. F. Mott, Phil. Mag. 17, 1259 (1968); Phil. Mag. 17, 1269 (1968); Adv. Phys. 16, 49 (1967).

100. M. Rice, J. Appl. Phys. 39, 958 (1968).

101. T. van Peski-Tenbergen and A. J. Dekker, Physica 29, 917 (1963).

102. P. G. DeGennes and J. Friedel, J. Phys. Chem. Solids 4, 71 (1958).

103. A. J. Dekker, Physica 25, 1244 (1959); J. Phys. Radium 23, 702 (1962); see also Physica 24, 697 (1958).

104. A. D. Brailsford and A. W. Overhauser, J. Phys. Chem. Solids 15, 140 (1960); 21, 127 (1961).

105. M. T. Beal, J. Phys. Chem. Solids 25, 543 (1964).

106. W. Marshall, Phys. Rev. 118, 1519 (1960).

107. M. W. Klein and R. Bront, Phys. Rev. 132, 2412 (1963); M. W. Klein, Phys. Rev. Letters 11, 408 (1963); Phys. Rev. 136A, 1156 (1964).

108. S. D. Silverstein, Phys. Rev. Letters 16, 466 (1966).

109. M. J. Levine, T. Ramakrishnan and R. A. Weiner, Phys. Rev. Letters 24, 1370 (1968).

110. P. A. Wolff, Phys. Rev. 124, 1030 (1961).

111. V. Jaccarino, J. Appl. Phys. 39, 1166 (1968).

112. R. Hasczawa and C. Tsuei, Phys. Rev. B2, 1631 (1970).

113. P. Lederer and D. L. Mills, Phys. Rev. 165, 837 (1968).

114. A. I. Schindler and M. J. Rice, Phys. Rev. 164, 759 (1967).

115. E. Babic, R. Krsnik, B. Leontić, Z. Vučić, I Zorić and C. Rizzuto, Phys. Rev. Letters 27, 805 (1971).

116. A. D. Caplin and C. Rizzuto, Phys. Rev. Letters 21, 746 (1968).

117. H. Suhl, Phys. Rev. Letters 19, 442 (1967).

118. M. Levine and H. Suhl, Phys. Rev. 171, 567 (1968).

119. D. R. Hamann, Phys. Rev. 158, 570 (1967).

120. P. Maitrepierre, J. Appl. Phys. 41, 498 (1970).

121. S. C. H. Lin, J. Appl. Phys. 40, 2173 (1969).

122. R. J. Harrison and M. W. Klein, Phys. Rev. 154, 540 (1967); 167, 878 (1968).

123. M. T. Béal-Monod, Phys. Rev. 178, 874 (1969).

124. S. H. Liu, Phys. Rev. 137, 1209 (1965).

125. See, for example, C. P. Flynn, D. A. Rigney and J. A. Gardner, Phil. Mag. 15, 1255 (1967); G. Baota and J. Vio, Solid State Comm. 5, 649 (1967).

126. E. Babic, P. J. Ford, C. Rizzuto and E. Salamoni (private communication).

127. F. T. Hedgwick and P. Li, Phys. Rev. B2, 1342 (1970).

128. I. Campbell, A. Caplin and C. Rizzuto, Phys. Rev. Letters 26, 239 (1971).

129. G. Bobel (private communications).

130. M. Cyrot, "Occurrence of Local Magnetic Moments in Disordered Materials (private communication)

131. K. Yosida, Phys. Rev. 106, 893 (1957).

132. A. N. Gerritsen and J. O. Linde, Physica 17, 573, 584 (1951); 18, 877 (1952).

133. Y. Toyozawa, J. Phys. Soc. Japan 17, 986 (1962).

134. N. F. Mott and Z. Zinamon, Phil. Mag. 21, 881 (1970); 21, 347 (1970).

135. E. Wolf, D. Losee, D. Cullen and W. Compton, Phys. Rev. Letters 26, 438 (1971).

136. N. F. Mott, Phil. Mag., Paper VIII, 24 (1971).

137. H. Mell and J. Stuke, J. Non-Cryst. Solids 4, 304 (1970).

138. R. W. Schmitt and I. S. Jacobs, Canad. J. Phys. 34, 1285 (1956).

139. J. Owens, M. E. Browne, V. Arp and A. Kip, J. Phys. Chem. Solids 2, 85 (1951).

140. T. E. Sharon and C. Tsuei, Phys. Rev. B3, 1047 (1972).

141. J. P. Burger, Ann. Phys. (Paris) 9, 345 (1964).

142. K. Handrich, Phys. Status Solidi 32, K55 (1969).

143. R. Koishore and S. K. Joshi, Phys. Rev. B2, 1411 (1970).

144. J. Hubbard, Proc. Roy. Soc. London A276, 238 (1963).

145. N. Rivier and K. Adkins (private communication).

146. K. Yosida and A. Okiji, Prog. Theor. Phys. (Kyoto) 34, 505 (1965).

147. F. Takano and T. Ogawa, Prog. Theor. Phys. (Kyoto) 35, 343 (1966).

148. R. Hasagawa and C. Tsuei, Phys. Rev. B2, 1631 (1970).

149. W. E. Wallace and M. Aoyagi, Mh. Chem. 102, 1455 (1971).

150. M. T. Hutchings and E. J. Samuelsen (unpublished data).

151. R. J. Gambino, T. McGuire, H. Alperin and S. Pichart, J. Appl. Phys. 41, 933 (1970).

152. M. A. Ruderman and C. Kittel, Phys. Rev. 96, 99 (1954).

153. J. W. Lorain, R. J. White and A. D. Grassie, Phys. Rev. B5, 3659 (1972).

154. E. Hart, Phys. Rev. 106, 467 (1957).

155. The amorphous Pd-M-P alloy where M = Ni, Co and Fe was discovered by P. Maitrepierre. It was extended to include Mn by Chang-C. Tsuei.